Study, Design and Testing of Structural Configurations for the Bird-Strike Compliance of Aeronautical Components

Michele Guida

Department of Aerospace Engineering

University of Naples "Federico II"

A thesis submitted for the

Doctoral Degree in Aerospace Structure

tutor prof. Francesco Marulo

December 2008

to my loving parents, my wife Diomira and my son Antonio

Acknowledgements

It was a pleasure for me to work with all the wonderful people in Department of Aerospace Engineering in University of Naples.

I would like to thank professor Marulo for being a great advisor, for giving me the opportunity to conduct my philosophical doctor's degree under his guidance and supervisions, and, for giving me the chance to visit several interesting conferences. I learned a lot during this time and I am convinced that this knowledge will help me in the future. Professor Marulo has provided motivation, encouragement, and support throughout my studies.

I would like to thank professors De Rosa, Franco and Ricci for reviewing my thesis. I am happy to have such a supportive co-supervisors.

My thanks to my friends and colleagues for the great time I had in our group. I enjoyed the atmosphere, their friendship, and their support. My thanks to eng. Grimaldi and dr. Polito.
It was a pleasure to work with all these people and to benefit from their knowledge.

Furthermore, special thanks to dr Meo and Polimeno for their help and for the interesting and fruitful discussions during a professional training in University of Bath, UK, at Department of Mechanical Engineering.

My thanks to mrs Colino for accompanying and supporting our group over many years and for being open-minded to questions.

Last but not least, I wish to thank my family who have always supported me for enjoying life together with me.

Abstract

This work is the result of a collaborative research project between the university (Department of Aerospace Engineering at University of Naples "Federico II") and an industrial partner (Alenia Aeronautica at Pomigliano d'Arco). The aim of this project was to design, with the help of finite element analysis and the experimental tests, an aircraft wing leading edge structure with innovative materials, that satisfies the optimization of requirements such as weight and performance. This study was driven by the industrial demand to improve the design rules necessary to the evaluation of the structural response of a leading edge when subjected to bird-strike.

The first step was the material characterization: an extensive series of materials was tested to determine stiffness and strength properties on glass-based fiber metal laminate. Static tests were performed to determine the stress-strain curve, dynamic tests to evaluate material strain rate sensitivity at medium rate regime and, impact tests to determine the threshold for impact energy which correspond to visible impact damage.

Afterwards several configurations of an one-bay component of a typical wing leading edge were built and subjected to the bird-strike tests carried out at Alenia plant by an air pressure gas gun facility. Various materials, lay-up distribution and boundary conditions were investigated. The numerical finite element simulations were performed using the commercial explicit integration code MSc/Dytran. This work describes the basic assumptions of

the analyses, i.e. bird properties, composite failure modes, and the way in which the simulations have been carried out in an industrial environment. Numerical simulations were able to predict that the bird did not penetrate the leading edge skin. The final correlation between numerical and experimental showed that good correlation was achieved.

Finally the tests were useful to design and test a new configuration of leading edge structure able to satisfy the bird-strike requirement according to the Federal Aviation Regulation (FAR part 25, section 25.631 "Bird-strike Damage"). Compliance with this section we studied the configuration of the C27J aircraft, that presents a cruise velocity of 464km/h (=250kts), so the impact speed with an 8-pound bird is a potentially serious and damaging event that must be accounted for the design of flight critical aircraft components. The starting thickness of the fin C27J airplane's aluminium alloy leading edge was 0.8mm with a weight of 12.1kg. Before this work, to satisfy the airworthiness standards about the bird-strike damages, the thickness of the aluminium alloy leading edge was increased to 3.2mm with a skin weight of 36.8kg, this thickening involved a weight increasing of 305% related to skin thickness of 0.8mm.

After this research work, to certificate the empennage structure after impact with an 8-pound bird according to requirements, a innovative composite configuration has been studied, which offered an amount weight of 18.2kg producing a weight conservation of 51% related to leading edge in aluminium alloy with a thickness of 3.2mm. Furthermore this research project allows to validate a ribless configuration about the leading edge; this solution aided the manufacturing reducing the rib's installation onto the leading edge structure. The leading edge configuration in the fiber metal laminate and ribless has been tested at impact with an 8-pound bird at a speed of 250kts and the test has been considered highly satisfied and it has met the quality of requirements.

Contents

List of Figures

Chapter 1

Introduction

1.1 Overview

The bird-strikes concerned both civil and military aircrafts. The external surfaces of an aircraft which include windshields, nacelles, canopies, wind leading edges, engines, are susceptible to bird-strikes. The first known collision between wildlife and an aircraft occurred in Ohio in 1908 when Orville Wright struck and killed a bird near Dayton (1).

The bird-strikes to civil and military aircraft are reported into a National Wildlife Strike Database. Only in the States of America, each year, 36,000 aircraft accidents, produced by bird-strike, are estimated, and since 1988, wildlife strikes have killed more than 194 people and destroyed over 163 aircrafts. Moreover, population development of large flocking birds has increased dramatically in many parts of the world. Many researcher focused their research scientific on this problem, and the most of aeronautical companies build new airplane according to this requirements, even if yet neither design/construction standards nor operational practice has changed to reflect the new threat due to possible bird-strike. Nowadays the aircraft companies invest money in the crashworthiness and the bird-strike becomes

a design requirement. Certification standards, which include the verifing of the structural integrity of airframes and engines, are established by U.S. Federal Aviation Administration (FAA) and European Aviation Safety Agency (EASA).

The military and civil bird-strike statistics demonstrate the vulnerability of forward facing areas to bird-strike. It is important, therefore, that all the implications of bird impact are considered at the design stage of the aircraft. In particular the damage tolerance of the aircraft should be investigated taking account:

- Residual strength and stiffness of damage structure.
- Aerodynamic loading on damaged structure.
- Aerodynamic handling of damaged aircraft.
- Change in flutter characteristics.
- Effect of strike on emergency system.
- Residual vision of transparency components.

Essential mechanism and system should not be sited in vulnerable positions on the aircraft (e.g. directly behind leading edge or on front on the undercarriage). Where this is unavoidable consideration should be given to duplication of equipment or protection by armouring.

1.2 Ancient Solutions to Modern Problems

Generally, the number of reported strikes decreases with altitude. Studies, reported in (2), showed that it is near the airport where aircraft are most vulnerable to bird-strikes. Birds are attracted to airport due to the presence

of shelter, feeding, drinking and bathing areas. In United States, 92% of the strikes occur at below 3000 feet (920m) and a total of 97% of the reported strikes occur during the taking off and landing phase of the aircraft, (3).

ICAO, International Civil Aviation Organization, established different regulations about the bird-strikes in the annex 14, which states: *"The bird-strike hazard on, or in the vicinity of, an aerodrome shall be assessed through: (a) the establishment of a national procedure for recording and reporting bird-strikes to aircraft; and (b) the collection of information from aircraft operators, airport personnel, etc. on the presence of birds on or around the aerodrome constituting a potential hazard to aircraft operations."* This annex requires only that the airport's director records a database about the accidents due to the bird-strikes. Nowadays the normal procedure that operating company carry out to avoid the strike of a bird with an aircraft is to appoint a falconer to control the bird population with the use of trained falcons within the airport boundaries. This is an additional system to prevent bird-strikes. Another one is to use a horn, which is able to keep out at a distance birds from the run way so to avert the danger to collision.

1.3 Certification Specifications

Aircraft leading edges must be designed to absorb impact energy in order to protect the primary structures in the event of bird-strike. It is therefore critical to ensure that the aircraft leading edges are able to withstand to such high velocity impact to guarantee the safe landing of the aircraft after the strike. Currently, commercial aircrafts are capable of operate at a high speed greater than 250 knots and current design, construction and certification standards for these aircraft were developed over 40 years ago.

The EASA Certification Specifications, CS 25 in the section 631, (4), states that: *"The empennage structure must be designed to assure capability*

of continued safe flight and landing of the airplane after impact with an 8 lb bird when the velocity of the airplane (relative to the bird along the airplane's flight path) is equal to cruise velocity (Vc) at sea level, selected under, (5). Compliance with this section by provision of redundant structure and protected location of control system elements or protective devices such as splitter plates or energy absorbing material is acceptable. Where compliance is shown by analysis, tests, or both, use of data on airplanes having similar structural design is acceptable."

The regulations requires that the damaged structure must be able to withstand the static loads (considered as ultimate loads) which are reasonably expected to occur on the flight and if significant changes verified in structural stiffness or geometry, as consequence of a structural failure or partial failure, the damage tolerance must be further investigated. When a bird-strike occours an aircraft must demonstrate the ability to land safely after being struck by a bird with reasonable weight somewhere on the structure, at normal operating speeds. Impacted components must maintain structural integrity during the large transient loading resulting from bird-strike loads.

Certification for bird-strikes is mainly achieved by experimental full-scale test, but numerical simulations provide an invaluable tool to evaluate designs requirements and to reduce the costs of the experimental programme. In the last years there is the desire to improve modelling capabilities and enable verification by simulation, the explicit FE codes have been used to develop high efficiency bird-proof structures. Explicit FE analysis is a numerical technique used for the analysis of highly non linear behavoiur of materials with inelastic strains, high strain rates and large deformations such as it would occour during a crash and they offer different approaches to bird modelling: the Lagrangian approach, techniques based on Eulerian or Arbitrary Lagrangian Eulerian (ALE) approach, and recently solvers based on Smoothed Particle Hydrodynamics (SPH) Method.

1.4 Further Design Considerations

From the available statistics appears that the chances of sustaining a bird-strike on the wing and empennage's leading edge are high. The primary consideration must be to maintain the structural integrity of the wing box, but particular attention should be given to the other implications and consequences of a strike including:

- The effect on control system, hydraulics, electrics, de-icing system etc, placed between the leading edge and front spar.
- Possible damage to aircraft controls, flaps aileron, slat.
- Possible damage to engine pylons, damage to fuel pipes etc.
- Strikes causing the inability to jettison fuel.
- Strike causing inadvertent weapon release.

The accent is on deflection or absorption of impact kinetic energy. Where possible the leading edge should be continuous. Tests have shown that a leading edge packed with composite honeycomb or foam have the tendency to transfer energy into the structure resulting a damaged area greater and reducing the possibility to have a localized damage. Penetration of the leading edge usually occurs by tearing at the rivet attaching the skin to the backing stiffeners. Increasing the strength of the leading edge skin at the attachments will improve the bird-strike resistance. This can be achieved in several ways:

- Increase thickness of skin.
- Changing skin material.
- Using bonded or integral stiffeners.

In particular the empennage structure must exhibit satisfactory strength and stiffness characteristics after an impact, and it is necessary that the control system of the aircraft remain unaffected and the tailplane structure is attached to the fuselage. The curvature of the leading edge is favourable to reduce the effects of the strike, because the contact forces reduce the damage zone after the impact related to the impact on the flap panel, but a major proportion of this energy is transferred to the leading edge, but in general to the tailplane root as shear, torque and bending moments on the fuselage attachments. With T-tail designs having small tailplane to fin attachment geometry, the root bending moments become fin torsion loads hence the fn attachments geometry should be designed with this in mind.

1.5 Literature Review

The traditional bird-strike design methods use the empirical formula, (6), to determine the thickness of structural component so to be able to resist at bird impact. But the airworthiness requirements are gradually increasing, and the need to reduce design life cycle time and costs with ever more complex aircraft structures using advanced numerical tools is attractive. In the last years many researcher focused their scientific researches on the impact event, but the phenomenon is studied from more 50years.

In 1955 Parkes, (7), was the first to study the plastic deformation of structural elements under impact loading.

In 1975 Barbers, Taylor and Willbeck, (8), were the first to consider the bird-strike as a soft body impact problem studying the characterization of birds impacting a rigid plate and founding that peak pressures, which were generated in the bird impact on a rigid plate, were independent of the bird size and proportional to the square of the impact velocity.

In 1979 Cassenti, (9), developed the governing equations a soft body impact on a rigid plate with the constitutive equation of the impacting material to obtain analytically the Hugoniot pressure or the pressure generated in the beginning of the impact.

In 2001 Goldsmith, (10), analyzed the impact theory and behaviour studying a transverse impact of a mass on a beam assuming a equivalent system in which the beam is modelled by a massless spring. Goldsimth used energy method and the Lagrangian equations of motion to obtain a relation between the static and dynamic deflections of the beam.

A very extensive description of the ALE method was presented by Stoker (1999), (11), who studied applications of the ALE method in the forming processes. To explain the ALE method, Stoker included a section with fundamentals of continuum mechanics, followed by a derivation of the ALE motion description, and a mathematical formulation used for calculations.

In 1997 Birnbaum, Francis and Gerber, (12), used coupling techniques for numerical methods applied to solve structural and impact simulation problems. The authors provided examples of all approaches to bird modelling, Eulerian, Lagrangian, ALE and SPH techniques, applied to general fluid interaction and impact problems. To compare the methods described, the authors created three simulations of a Lagrange projectile impacting a concrete target (modeled in SPH, Lagrange and Euler). The Lagrange-SPH combination produced the best results, for the visualization of the impact. The three methods provided an adequate prediction of the deceleration of the projectile when compared to test results, although the average peak deceleration of the projectile was under-predicted by 20- 30%.

1.6 Bird-Strike Testing

Bird-strike testing are performed according to the Standard Test Method, (13). An air pressure gun is used to shoot the bird at the test article at the speeds desired. Figure 1.1 is the facility sited at Alenia plant and it used during the massive campaign of the experimental tests both on the bay leading edge component and full scale leading edge test article during the research project. This apparutus has a barrel length of 12m and it is capable to speed up to 140m/s.

Figure 1.1: Air Pressure Gun

The projectile is held inside a sabot packed with expanded polystyrene so that it does not change position or suffer any damage under the acceleration it must withstand when it is fired. The functions of the sabot are to hold and support the projectile, to seal the pressure chamber from the gas gun barrel and to guide the projectile during firing. It must be as light as possible since it constitutes an unwanted dead mass and it must break up and separate easily from the actual projectile just prior to impact without in any way affecting the projectile velocity or trajectory. Final tolerances are important

because they are such as to let the projectile go through the barrel without causing friction and then a slowdown in speed when it is fired.

Different structural aeronautical components must be subjected to the bird-strike tests as windshield, engine, wing leading edge, empennage leading edge and anemometer system. The table 1.1 shows the different bird weights required for the experimental tests.

A typical windshield must withstand, without penetration, the impact of a 4 lb bird when the velocity of the airplane is equal to the value of cruise speed, at sea level, (14). The aim is show that pilots will not be injured by the bird, windshield will continue to hold cabin pressure following to a bird-strike event, and it is possible to land in safety conditions.

A typical wing leading edge is characterized by being resistant to a perforation and to contain the deformation to avoid the spar can be damaged because of a strike with a bird of 4 lb, (15). The impact must neither compromise the integrity of the structural component nor to activate any switch as consequence of the strike so to produce a different catastrophic event. Differently the empennage leading edge is characterized by a strike with a bird of 8 lb, (15) and (4).

The aeronautical engine must continue to produce at least 75% thrust for 5m after ingesting a bird, (16). Fan integrity tests must demonstrate that the engine does not catch fire or disintegrate after being struck by a single 4 lb bird.

Component	**Bird Weight**	**Regulation FAR25**
Windshield	4 lb	775
Wing leading edge	4 lb	571
Empennage leading edge	8 lb	571 and 571
Engine	4 lb	section 33

Table 1.1: Bird Weight Requirements

1.7 Objective of the Work

One of the main structural requirements of a leading edge of a wing is to protect the wing torsion box and control devices from any significant damage caused by foreign object (i.e. bird-strike, etc) and to allow the aircraft to land safely. In particular, leading edge must be certified for a proven level of bird impact resistance. Since the experimental tests are expensive and difficult to perform, the use of advanced numerical tools can provide a quick and inexpensive way of designing crashworthy sandwich structures.

The aim of this research work was to evaluate the non linear behaviour of the structure subjected to an impact analysis and to design a new aircraft wing leading edge structure with composite structure with the help of finite element analysis so to satisfy the aviation requirements about to crashworthiness. The study was driven by the industrial demand to improve the design rules necessary for the evaluation of the structural response of a leading edge of an aircraft.

Several configurations of a one-bay component of a typical wing leading edge was prepared and these configurations were consequently built and subjected to bird-strike tests. Various materials, lay-up distribution and boundary conditions were investigated, extensive experience has been gained with metallic leading edges subjected to bird-strike. However, very limited data exist for composite or hybrid metal/composite structures.

The final configuration presents a sandwich structure made up of fiber metal laminate skins and flexcore as core. Before each test was carried out, pre-test numerical analyses of bird-strike were performed adopting Lagrangian, ALE and SPH approaches on a wing leading edge of a large scale aircraft using the MSC/Dytran and LS-Dyna solver codes. The numerical and experimental correlation have shown good results both in terms of global behaviour of the test article and local evolution of some measurable param-

eters confirming the validity of the approaches and possible guidelines for structural design including the bird impact requirements.

1.8 Finite Element Solver

The simulation methodology, used in this work for the analysis of highly non-linear phenomenon particularly suited to scenarious such as bird-strike, is based on the explicit finite elemenet analysis. The time step used in the solution algorithm is chosen to be smaller than the time taken for a shock wave to propagate through the smallest element in the model. This resulting time step, normally of the order of a microsecond or less, is necessary to ensure that all energies associated with the propagating shock wave are adequately captured by the analysis. A small time step means that thousands of structural analyses are required to complete the simulation of a complex scenario. For example, the bird-strike events presented herein spanned approximately 10ms, requiring up to 28h of CPU-intensive analysis. Nonetheless, the cost to explore many impact cases through simulation is a fraction of the cost of performing one full-scale physical impact test.

The time step for implicit solutions can be much larger than is possible for explicit solutions. This makes implicit methods more attractive for transient events that occur over a long time period and are dominated by low frequency structural dynamics. Explicit solutions are better for short, transient events where the effects of stress waves are important. There is, of course, an area where either method is equally advantageous and may be used. Explicit solutions have a greater advantage over implicit solutions if the time step of the implicit solution has to be small for some reason. This may be necessary for problems that include:

- Material nonlinearity. A high degree of material nonlinearity may require a small time step for accuracy.

- Large geometric nonlinearity. Contact and friction algorithms can introduce potential instabilities, and a small time step may be needed for accuracy and stability.
- Those analyses where the physics of the problem demands a small time step (e.g. stress wave effects).
- Material and geometric nonlinearity in combination with large displacements.

Convergence in implicit methods becomes more difficult to achieve as the amount of nonlinearity for all types increases. Explicit methods have increasing advantages over implicit methods as the model gets bigger and provide the cheapest solution even for problems dominated by low-frequency structural dynamics. The problem is analyzed using the Lagrangian solver, the Eulerian solver, the Euler-Lagrange coupling (ALE), or the Smooth Particle Hydrodynamics (SPH).

The benefit of the Lagrangian solver is that the displacements, deformations, and stresses in structures can be monitored with a high degree of precision. However, extreme deformations may lead to drastically reduced time steps and extended run times. The Lagrangian solver should be used for structural components that may undergo large deformation and for which the deformed geometry and residual stress state are of major importance.

The benefit of the Eulerian solver is that the complex material can be modeled with no limit to the amount of deformation. With increasing deformation, however, the boundaries between the materials may become less precise. The Eulerian solver should be used for bodies of material, such as fluids or solids, which may experience extremely large deformations, shock wave propagation, and even changes of state. With the coupling feature, the advantages of both solvers can be used in one analysis. This allows you to model the interaction of precisely defined structural components with fluids

and highly deformable materials. The Arbitrary Lagrangian-Eulerian (ALE) formulation is a combination of the Lagrangian and Eulerian formulations. It is necessary to set the mesh motion that best suite the problem in order to minimize the mesh distortions and obtain the best results.

The Smooth Particle Hydrodynamics formulation is a meshless Lagrangian technique to model the fluid equations of motion using a pseudo-particle interpolation method. Modeling a continuum requires a number of particles go to infinity. Capability of the method to address problems characterized by large mesh deformations The main advantages is that the nodes are continuously deformable and distort automatically to put computational effort where it is needed. The main disadvantage that it is computational demanding, both in memory and in CPU time. Another disadvantage is that particles may penetrate the boundaries and causing loss of smoothness and accuracy.

Chapter 2

Impact Analysis

2.1 Theoretical Consideration

2.1.1 Bird Impact Forces

The energy transfer, or pressure, that results from a bird-strike to an aircraft can be estimated through relatively simple calculations. Taking the simplest approximation, after the collision the change in a bird's kinetic energy is defined by the equation (2.1):

$$\Delta KE = W = Fd = \frac{1}{2}mv^2 \tag{2.1}$$

where W is the work, F is the force, d is the distance over which the force is delivered, m is the mass of the bird and v is the velocity of the aircraft.

The force that the airplane felt is given by equation (2.2):

$$F = \frac{\Delta KE}{d} = \frac{mv^2}{2d} \tag{2.2}$$

We can estimate the bird's mass, m, and the aircraft speed, v, with ease, The key parameter then is the distance d over which the impact is delivered.

As a first approximation, let's assume it is half the distance traveled by the aircraft in moving through the bird-strike event. If we further assume that the bird can be represented as a sphere, we end up with (2.3):

$$F = \frac{mv^2}{2r} \tag{2.3}$$

If we assume the bird is spherical, then the bird's size depends on its mass according to the relation (2.4):

$$m = \rho V = \frac{4}{3}\pi r^3 \rho \tag{2.4}$$

where ρ is the bird's density and V is the sphere's volume.

Combining the two previous expressions gives equation (2.5):

$$F = \frac{2\pi r^2 \rho v^2}{3} \tag{2.5}$$

Expressed in an equation, impact force is proportional to bird mass and the square of impact speed. Applying actual figures, a 4 lb bird that strikes an aircraft traveling at 250 kts will deliver an impact force of approximately 38,000 lbs. At an airspeed of 400 kts, the force increases to 100,000 lbs. In the possibility of a 8 lb bird, this forces are higher.

2.1.2 Momentum Transfer

Assuming that a bird is essentially a fluid body, the motion of the bird before and after impact is illustrated in figure (2.1).

The initial momentum of the bird along trajectory is simply mv, where m is the mass of the bird and v is the initial impact velocity of the bird. The momentum of the bird along trajectory after impact is zero as the bird has only radial velocity. Therefore, the momentum transferred to the target during the impact is simply equal to mv. This simple picture may be easily extended to oblique impacts by noting that only the component of

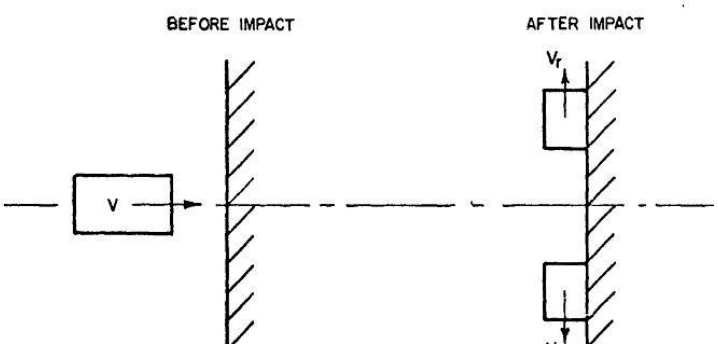

Figure 2.1: Motion of a bird before and after impact.

momentum normal to the impact surface is transferred to the target during the impact. Therefore, the momentum transfer, or impulse, I, is given by:

$$I = mv sin\theta \tag{2.6}$$

where θ is the angle between trajectory and the surface of the target. The equation (2.6) is the momentum transfer or impulse imposed onto a target during impact if the bird was a fluid body and the target was completely rigid.

2.1.3 Impact Duration

If the bird is assumed to be a fluid body, the impact begins when the leading edge of the bird first touches the target. The impact continues until the trailing edge reaches the target and there is no further bird material flowing onto the target. If the bird does not decelerate during impact, then this *squash-up time*, T_S, is given by:

$$T_S = \frac{l}{v_S} \tag{2.7}$$

where l is the length of the bird.

In an oblique impact, figure (2.2), the situation is different, the effective length of the bird, l_{eff} is now:

$$l_{eff} = l + dtg\vartheta \tag{2.8}$$

where d is the diameter of the bird. A real bird is more nearly an spheroid, in which case the effective length is less than that given by equation (2.8). However, when the straight length is replaced by the effective length in equation (2.7), a reasonable estimate of the pulse duration for an oblique impact is obtained.

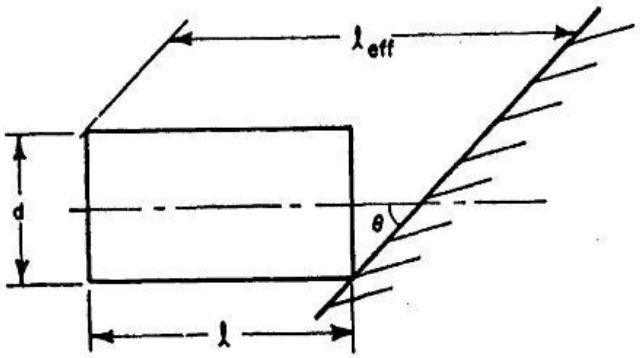

Figure 2.2: Oblique impact effective bird length

2.2 Bird Modeling

The non homogeneity of the bird is the main limitation to obtain the repeatability of tests. To idealize a bird impacting a rigid surface as a homogenous soft material is not real because its internal stresses greatly exceed its material ultimate strength, but are well below the target material ultimate strength. For these reasons, the bird impact process has been successfully modelled by the hydrodynamic theory, (17), where the bird do not bounce

and impact response is determined by the length of the bird and by the initial impact velocity but not by the material strength. The peak of pressure is divided in three different contributions, figure (2.3):

- The pressure developed in the initial instant of the impact defined as "shock pressure".
- The decay of pressure after the first instant of impact defined as "shock pressure decay".
- The stagnation pressure on the impacted surface defined as steady state pressure".

About the *shock pressure phase*, when the soft projectile impacts the target, a shock wave is formed as the particles on the front surface of the projectile are instantaneously brought to rest relative to the target, and a complicated stress field with high pressure gradients develops in the projectile.

$$p = \rho_i u_s u_0 \tag{2.9}$$

where ρ_i is the density of the projectile, u_s is the shock wave velocity, and u_0 is the projectile's initial velocity.

Generally, the bird material hydrodynamic response can be characterised by a polynomial interpolation, (18), of the curve relating the pressure to the density ratio ρ/ρ_i given by equation (2.10):

$$p = \rho_p u_{sp} u_0 \left(\frac{\rho_t u_{st}}{\rho_p u_{sp} + \rho_t u_{st}} \right) \tag{2.10}$$

where ρ_p is the density of the projectile, ρ_t is the density of the target, u_{sp} is the projectile shock wave velocity, u_{st} is the target shock wave velocity, and u_0 is the projectile's initial velocity. In equation (2.10) the initial peak pressure depends only on densities and velocities and not on the length

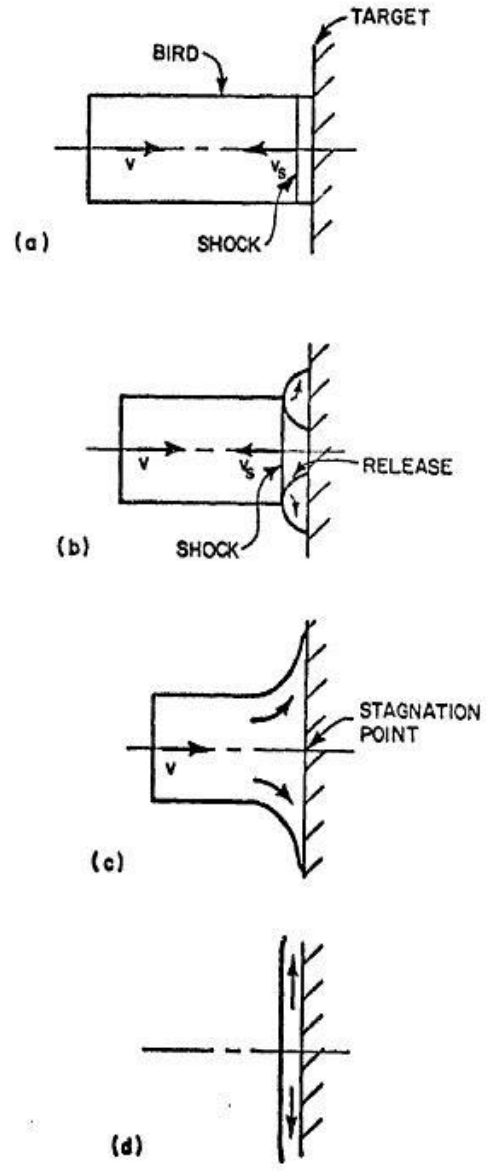

Figure 2.3: The phases of bird impact (a) initial impact (b) impact decay (c) steady flow (d) termination

or cross-sectional area of the projectile. However, as reported by Wilbeck, (17) bird substitute materials such as gelatine and water mixture are slightly more severe than a real bird, because the anatomic structure of birds includes bones, lungs and other cavities that reduce the bird density.

After the initial phase of the impact, there is the *decay pressure*; the shock pressure loading decreases with the time and also with distance from the centre of the impact region, the shock wave emerging at the lateral free surfaces of the body is followed by a set of release waves. The radial pressure distribution is given by equation (2.11):

$$p_r = p_c e^{-\frac{kr}{R(t)}} \tag{2.11}$$

where p_c is obtained from equation (2.10), K is a constant, r is the radial distance from the center of the impact region, and $R(t)$, function of time, is the maximum contact radius at time t. The length of this high pressure event is on the order of tens of milli-seconds. This is followed by a pressure release wave travelling towards the centre of the impact zone, eventually attaining an approximate steady state.

At least there is the *steady state pressure phase*, characterized by the stagnation pressure on the impacted surface during this steady state and described by the equation (2.12):

$$p_s = k\rho_0 v_0^2 \tag{2.12}$$

and is independent of bird shape. The steady state pressure is usually taken as 10-30% of the peak Hugoniot shock pressure at the centre of the impact region, based on experimental studies. For an incompressible fluid, k=1/2; but for most density increases with pressure, and as result, k may approach a value of 1.

Wilbeck and Rand conducted an extensive test program with substitute birds of various materials and shape. They conducted that a real bird can

be accurately modelled analytically by a a mixture of 85-90 volume percent water and 10-15% of air, with a slightly increased density for water of $1.06 g/cm^3$. For this purpose, they recommended that a gelatine bird with 15% porosity (to account for the avoids in real birds) represent a real bird accurately. They also found that a substitute analytical/synthetic bird will be more accurate if it is modelled as a cylinder with hemi-spherical ends and a length to diameter ratio approximately the same as the bird being modelled.

2.3 Numerical Analysis

In recent years, explicit FE codes have been used to develop high efficiency bird-proof structures. These codes adopted various finite element approaches to model the impact phenomena: the Lagrangian approach, Eulerian or Arbitrary Lagrangian Eulerian (ALE) approach, and recently solvers based on Smoothed Particle Hydrodynamics (SPH).

2.3.1 Lagrangian Approach

The various formulations existent for the finite element analysis differ in the reference coordinates used to describe the motion and the governing equations. The Lagrangian method uses material coordinates, also known as Lagrangian coordinates, as the reference; these coordinates are generally denoted as X. The nodes of the Lagrangian mesh are associated to particles in the material under examination; therefore, each node of the mesh follows an individual particle in motion, this can be observed in figure (2.4)

The motion description for the Lagrangian formulation is (2.13):

$$x = \varphi(X, t) \tag{2.13}$$

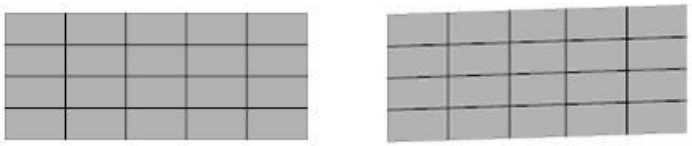

Figure 2.4: Lagrangian solver

where φ(X, t) is the mapping between the current position and the initial position.

The displacement u of a material point is defined as the difference between the current position and the initial position (2.14):

$$u(X,t) = \varphi(X,t) - X = x - X \tag{2.14}$$

The speed and acceleration are defined as the temporal derivates:

$$v = \frac{\partial}{\partial t}[x(X,t)] \tag{2.15}$$

$$a = \frac{\partial^2}{\partial t^2}[x(X,t)] \tag{2.16}$$

At the end of the time step if current configuration is the same related to initial position it's considered a formulation is known as the Updated Lagrangian formulation, in this case the new reference is the current state. If the current configuration consists of a modified configuration then it possible consider the formulation is known as the Total Lagrangian formulation, which as reference considers the initial state, when t = 0. This formulation describes the motion because fixed the initial position it is possible to restore a kinetic history about any point.

This formulation is used mostly to describe solid materials. The imposition of boundary conditions is simplified since the boundary nodes remain on the material boundary. Another advantage of the Lagrangian method is the

ability to easily track history dependant materials. However, a Lagrangian description of this problem may result in loss of bird mass due to the fluid behaviour of the bird which causes large distortions in the bird. In an explicit finite element analysis, the time step is determined by the smallest element dimension. The severe mesh distortion caused the time step to decrease to an unacceptably low value for the calculations to continue. These excessive distortions cause failure due to volumetric strain in some elements of the modeled bird.

2.3.2 ALE Approach

Before explaining the Arbitrary Lagrange Eulerian (ALE) method it is necessary to describe the Eulerian method for a better understanding of the ALE formulation. In the Eulerian formulation, the mesh remains fixed and the material under study flows through the mesh, as shown in figure (2.5). Since the mesh does not move, there is no possibility of mesh deformation,

Figure 2.5: ALE solver

which is a major disadvantage of the Lagrangian method in which the mesh moves and distorts with the material. This method is applied mostly to the simulation of fluid behaviour, although it has been applied to solid simulation. The major disadvantage of this method is difficult in tracking material interfaces and the history of the materials. This required more computations than in the Lagrangian methods, which leads to longer simulation time. The Arbitrary Lagrange-Eulerian (ALE) formulation is a combination of the Lagrange and Eulerian formulations in which the reference is set arbitrarily

by the user in order to capture the advantages of the methods while minimizing the disadvantages. The user must set the mesh motion that best suite the problem in order to minimize the mesh distortions and obtain the best results. This is the main disadvantage of the method, is that the user must be experienced in order to select the best method, and interpret the results obtained. In other words the material of a body under analysis moves through the Eulerian mesh; the mass, momentum, and energy of the material are transported from element to element. The Eulerian solver, therefore, calculates the motion of material through elements of constant volume. The Eulerian mesh is defined in exactly the same manner as a Lagrangian mesh.

General connectivity is used so the Eulerian mesh can be of an arbitrary shape and have an arbitrary numbering system. This offers considerably more flexibility than the logical rectangular meshes used in other Eulerian codes. Using the Eulerian bird technique, the bird flows through an Eulerian mesh to impact the structural finite element model. The Eulerian bird elements apply load to the structure elements through an ALE. In both cases the structure model is constructed with Lagrangian finite elements. This method does not need remeshing and is used for fluid dynamics simulations. The major disadvantages of the method are that the resolution of flow definition and interface definition is less than in other approaches. In the ALE method, the reference is chosen arbitrarily to use the optimal method for each step of the simulation. For the ALE method, the simulation is split into a Lagrangian phase, an Eulerian phase and a smoothing phase in between. Because of this, greater distortions of the material can be handled than those allowed by the Lagrangian method with higher resolution and the Eulerian approach. The solution of Eulerian approach is based on a so-called Riemann solution at the element faces that defines the fluxes of mass, momentum and energy, the conserved problem quantities. The non viscous

flow of a fluid or a gas is fully governed by the Euler equations of motion, (19).

2.3.3 SPH Approach

Smooth Particle Hydrodynamics (SPH) formulation is a meshless Lagrangian technique used to model the fluid equations of motion using a pseudo-particle interpolation method to compute smooth hydrodynamic variables. During the 70's this method was used to simulate astrophysical phenomenon, but at the beginning of the 90's it has been used to resolve other physics problems in continuum mechanics, crash simulations, brittle and ductile fracture in solids.

Due to the absence of a grid, this method allows solving many problems that are hardly reproducible in other classical methods discarding the problems that present mesh distortions and large displacements. Another advantage of the SPH method is that due to the absence of a mesh, problems with irregular geometry can be solved. In this formulation, the fluid is represented as a set of moving particles, each one representing an interpolation point, where all the fluid properties are known. Then, with a regular interpolation function called smoothing length the solution of the desired quantities can be calculated for all the particles, (20).

A real fluid can be modeled as many fluid particles provided that the particles are small compared to the scale over which macroscopic properties of the fluid varies, but large enough to contain many molecules so macroscopic properties can be defined sensibly. A large number of particles are needed for the SPH calculations, since the continuum limit is recovered when the number of particles goes to infinity. Particles in the SPH method carry information about their hydrodynamic and thermodynamic information, this in addition to the mass needed to specify the evolution of the fluid. Nodes in SPH are similar to nodes in a mesh, the difference is that these nodes

are continuously deformable and distort automatically to put more of the computational effort in regions of relatively high density. One disadvantage in SPH is that this method is computationally demanding, both in memory and in CPU time. This can be overcome using a parallel analysis with more than one CPU. There is also the difficulty of establishing the boundary condition when using the SPH method. Another disadvantage is that particles may penetrate the boundaries and causing loss of smoothness and accuracy.

The moving particles are described by:

$$(x_i(t), m_i(t))_{t \in P} \tag{2.17}$$

where P is the set of moving particles, $x_i(t)$ the location of particle i, and $m_i(t)$ the weight of the particle. The movement of each particle and the change of the weight is given by:

$$\frac{dm_i}{dt} = \nabla \cdot V(x_i, t) m_i \tag{2.18}$$

The quadrature formula can be written as:

$$\int_\Omega f(x)dx \approx \sum_{j \in P} m_j(t) f(x_j(t)) \tag{2.19}$$

A useful concept in SPH is the smoothing kernel. It is necessary first to introduce the auxiliary cubic B-spline function which has some good properties of regularity:

$$\vartheta(y) = \alpha_1 \times \begin{cases} 1 - \frac{3}{2}y^2 + \frac{3}{4}y^3 & \text{for } y \leq 1 \\ \frac{1}{4}\left(2 - y^3\right) & \text{for } 1 \leq y \leq 2 \\ 0 & \text{for } y \geq 2 \end{cases} \tag{2.20}$$

Where, α_1 is a constant that depends on the dimension and the shape of the kernel function. In two dimensions:

$$\alpha_1 = \frac{10}{7\pi} \tag{2.21}$$

The smoothing kernel is:

$$W\left(x_i - x_j, h\right) = \frac{1}{h}\theta\left(\frac{x_i - x_j}{h}\right) \tag{2.22}$$

where h is the smoothing length of the kernel. Generally, a property $A(x_i)$ is represented by its smooth particle approximation $A^h(x_i)$ of the function, and by approximating the integral in equation (2.19):

$$A^h(x_i) = \sum_{j=1}^{N} m_j \frac{A(x_j)}{\rho(x_j)} W(x_i - x_j, h) \tag{2.23}$$

The gradient of the function is obtained by applying the operator of derivation on the smoothing length.

$$\nabla A^h(x_i) = \sum_{j=1}^{N} m_j \frac{A(x_j)}{\rho(x_j)} \nabla W(x_i - x_j, h) \tag{2.24}$$

Initially in the SPH method, the smoothing length was chosen as constant during the entire simulation. However, it was shown that it is better for each particle to have its own smoothing length, depending on the local number of particles. The current method used for the smoothing length is the gather formulation. In this method

$$h = h(x_i) \tag{2.25}$$

is defined and the neighboring particles of a defined particle are the particles inside of a sphere centered in (x_i) with a radius of $h(x_i)$.

The equations for the SPH formulation presented in this section have been described by (21).

The mass density has been defined as:

$$\rho(x) = \sum_{j=1}^{N} m_j W(x_i - x_j, h) \tag{2.26}$$

The equation of conservation of the mass in a Lagrangian form is:

$$\frac{d\rho}{dt}(x_i) = -\rho \nabla V \tag{2.27}$$

The SPH approximation for the conservation of mass can be written in two different ways:

$$\frac{d\rho}{dt}(x_i) = \sum_{j=1}^{N} m_j (v(x_j) - v(x_i)) \nabla W_{ij} \tag{2.28}$$

or

$$\frac{d\rho}{dt}(x_i) = \sum_{j=1}^{N} m_j \frac{\rho}{\rho_j} (v(x_j)) \nabla W_{ij} \tag{2.29}$$

The SPH momentum equation may be written as:

$$\frac{dv}{dt}(x_i) = \sum_{j=1}^{N} m_j \left(\frac{P(x_i)}{\rho_i^2} \nabla W_{ij} - \frac{P(x_j)}{\rho_j^2} \nabla W_{ji} \right) \tag{2.30}$$

In the SPH analysis, it is important to know which particle will interact with its neighbors because the interpolation depends on these interactions. The influence of a particle is established inside of a sphere of radius of 2h, where h is the smoothing length. In the neighboring search, it is also important to list, for each time step, the particles that are inside that sphere. If we have N particles, then it is required (N-1) distance comparison. If this comparison is done for each particle, then the total amount of comparisons will be N (N-1). For the neighboring search, the bucket sort algorithm is used. The domain covered by the particles is split in several boxes of a given size. First the algorithm searches for neighbors, for each particle inside the main box and the neighbor boxes contained in the domain of influence of the particle. It is better to have a variable smoothing length to avoid problems related with expansion and compression of material. The main idea of this

concept is that it is necessary to keep enough particles in the neighborhood to validate the approximation of continuum variables. The smoothing is allowed to vary in time and space. For a constant smoothing length, a material expansion can lead to numerical fracture and a material compression can slow down the calculation significantly.

2.4 The Influence of Bird Shape

In many cases the bird model used in a simulation is based on a geometry and material type that represents the artificial birds used during physical experiments. The shape of the bird is often represented as a simple primitive geometry (cylinder, hemispherical ended cylinder, ellipsoid and sphere) to reflect the principal mass and shape; in particular, the bird is modeled as a projectile with the shape of a cylinder.

The weight of bird used in the impact testing was 8 lb, the density was $\rho = 950kg/m^3$, and it was shaped as a cylinder of 288mm long and a diameter of recreated 144mm diameter, figure (2.6), the finite element model of the cylinder is developed using eight-nodes underintegrated solid elements characterized by a progressive refinement towards the impacting end, (22). Moreover, to avoid penetrations, consequent to the distortions of the Lagrangian elements during the analysis, all the faces of the solid elements are involved during the impact with the targeting.

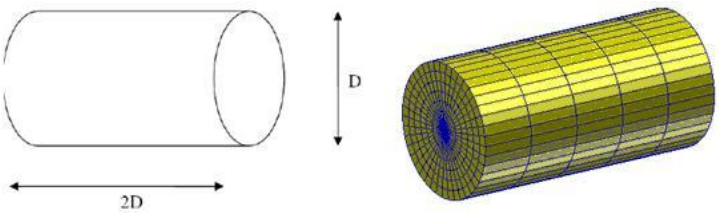

Figure 2.6: Bird shape as a cylinder

An alternative shape is to model the bird as a cylinder with hemispherical ends, which have been chosen to realise more realistic bird shapes than the idealised cylinder and will be referred to as bird models, figure (2.7).

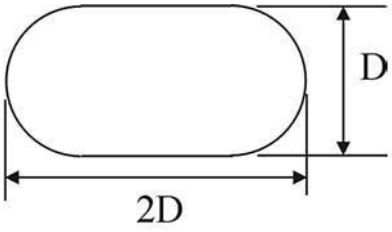

Figure 2.7: Bird shape with hemispherical ends

The results reported in (23) showed that the shapes having a curved impacting are characterized by initial peaks of pressure lower than those obtained with the cylindrical models. Moreover, high-pressure levels are developed only in a limited contact region. As a consequence, the overall contact forces of the bird models do not exhibit high initial spikes in correspondence of the initial pressure peaks as in the case of the cylindrical impacting body.

Chapter 3

Mechanical Behaviour of the Material

The aim of this project was to design, by the help of finite element analysis and the experimental tests, an aircraft wing leading edge structure with innovative materials, that satisfies the optimization of requirements such as weight and performance. This study was driven by the industrial demand to improve the design rules necessary to the evaluation of the structural response of a leading edge when subjected to bird-strikes, this study was related to Lockheed Martin C27J aircraft. This aircraft presents a cruise speed velocity of 250kts and according to requirements, (4), the leading edge configuration should be not perforated and in case of high deformations no critical damage must be induced to the front spar sited behind the leading edge, after the impact with 8 lb bird fired at 129m/s (250kts).

Different lay-up configurations were taken account in this work, so it is possible an optimization process about the configuration and the thickness. Five different configurations were considered for the experimental tests. The differences between the configurations concerned the lay-up, in general the aircraft wing leading edge structure was made of three different plies. The

outboard ply consists of Fiber Metal Laminate material made of aluminium alloy 2024-T3 and unidirectional glass/epoxy (FM 94-27% - S2 Glass 187-460) oriented in a cross-ply configuration. The inboard skin was aluminium alloy 2024-T3 with a thickness of 0.4mm and core skin was a honeycomb material of aluminium alloy 5052. The lay-up is reported in figure (3.1). The alternative configurations consist of a different outboard ply, which is

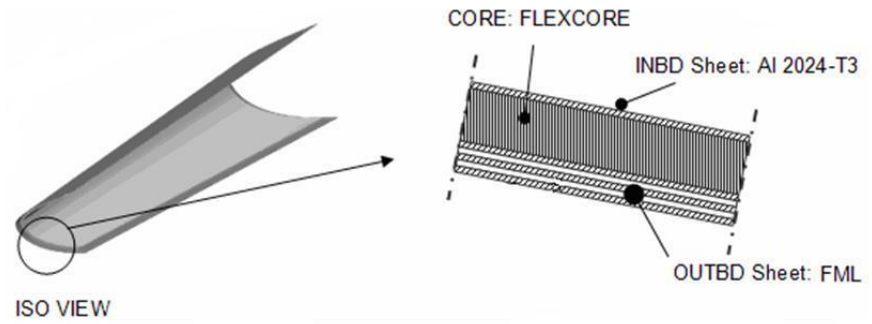

Figure 3.1: Lay-up of Test Specimen Configuration

substituted with an aluminium alloy sheet, lay-up was shown in figure 3.2. For both layup different configurations are studied, the differences were re-

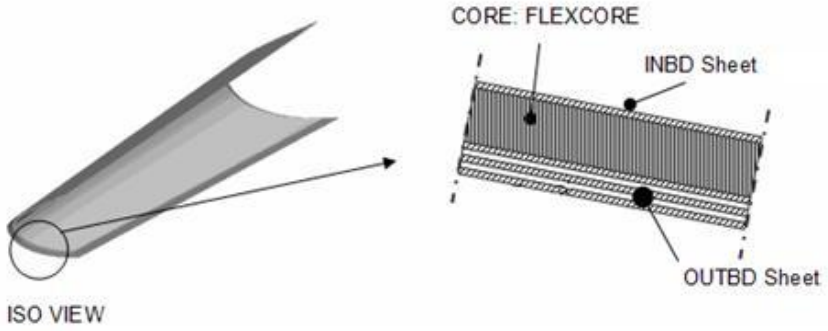

Figure 3.2: Test Specimen Configuration

lated to the thickness of the outboard ply. Summarizing, the materials used during the reserch project are:

- Sandwich honeycomb
- Fibre Metal Laminate (FML) and
- Aluminium.

The *sandwich structure* consists of honeycomb core between two metallic face plates. The significant mechanisms of energy absorption of these structures are the localized crushing of the core and the bending and stretching of the facings, while energy may be effectively absorbed through both local crushing and global deflection of the structural element as a whole. In order to construct suitable crashworthy sandwich elements, it is necessary to utilize components that have a high degree of energy absorption capability, examining the individual and coupled properties of the ingredients (facings and cores) comprising these elements. The core of a sandwich material must possess increased strength in shear to avoid relative sliding of the face plates when a bending deformation is applied on the sandwich panel, then must be stiff enough to ensure flatness and to prevent wrinkling of the intact portions of facings during the whole crushing process.

Fibre Metal Laminates, (FML), are a family of materials consisting of alternating "plies" of thin aluminium alloy and fibre/epoxy. The concept of FML's originated at Fokker in the Netherlands in the 1950s, and extensive development work has been performed since the 1970's. The laminates can be formed and machined like aluminium alloys and have a high specific strength similar to composite materials, giving. The major advantage is a impact strength, and this one has characterized our choice during the research project.

The aim of this work is create a detailed finite element model using an explicit code, so it is necessary to obtain the experimental data of different materials to correlate the experimental results with the numerical results. The experimental data of the honeycomb are known in bibliography, many researchers have focused their attention on the material characterization for different applications, so in the next sections the input required to model the material by finite element analysis have reported emphasizing the input required for the crash analysis. About the Fiber Metal Laminate it has been necessary to perfom an extensive series of materials characterization experiments to determine stiffness and strength properties on glass-based FML. In the next chapter the experimental tests are reported in detail.

3.1 Fiber Metal Material

Due to the increasing demand for lightweight construction, especially in the aerospace industry, a lot of research is being focused in the new composite materials. For airliners, maintenance costs are a high percentage (20%) of the direct operating costs (DOC), and for this reason there is a strong need for more durable and more damage tolerant structural materials to reduce the maintenance costs and the structural weight of the aircraft, (24). The high bending stiffness to weight ratio of the sandwich structure makes the FML material a preferable choice in applications where weight savings are important. Fiber Metal Laminates (FML) represent a family of hybrid materials, (25), it is presented as a hybrid composite consisting of thin aluminium layers alternating with thin layers of glass fiber reinforced epoxy. The composite has three main components, the metal alloy, the fiber system and the resin or cohesive which are variables, and that may result in a wide range of different materials. By varying i) the thickness of the layers, ii) the number of layers in a laminate, and iii) the fiber orientations, the variety in laminates

is further increased. These materials are so widely used in the aerospace industry because of their excellent damage tolerance properties and fatigue resistance. However, metals show visible damage caused by impact mainly on the surface of structures, while damage is hidden inside composite structure especially when subjected to low velocity impact, (26). This invisible form may cause serious decrease in material strength, which can be created during production, repair, maintenance, and small particle crashes to the composite body, caused by hailstones, dropped tools, and runway debris.

The FML were primarily developed to obtain a material with a high fatigue crack growth resistance without fiber failure, and continuous, it implies that the application to the aircraft structure can lead to: (i) large weight savings; (ii) improved safety; (iii) high strength; (iv) fatigue insensitivity; (v)outstanding workshop properties; (vi) good and easy repairability; (vii) excellent damage tolerance; and (viii) production simplifications, (27). The superior behaviour of these laminates can be translated towards weight savings in aircraft structures combined with cost savings in production-and maintenance.

During fatigue loading, at high stress level, cracks may originate in the FML material. The crack initiation starts at a free surface, i.e. an outer layer of the laminate, and the crack tends to grow, (28). While the monolithic material's crack growth rate increases rapidly with increasing crack length, the laminate materials exhibit their characteristic, almost constant slow crack growth behaviour, (24). This almost constant crack growth is caused by the crack bridging of the fibres, see figure (3.3).

In fatigue loading the crack initiates in the aluminium layer but the fiber layer stays intact and the stresses are bypassed over the crack. Thus the stress intensity factor at the cracks of the aluminium layers is reduced. Effective fibre bridging is only possible in combination with an adequate and local separation of the metal and composite layer, so-called delamination,

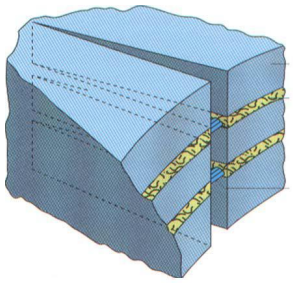

Figure 3.3: The bridging of the fibre layers of the cracked aluminium layers

(24). The delamination is required, so that the fibres have enough length to elongate. From the crack propagation and delamination growth observed in experiments, it is concluded that both mechanisms are in balance with each other. Without the delamination the crack growth would increase since fibre failure would have occurred. It is important to mention that, FML excels in all types of fatigue critical aircraft loading situations (29).

The residual strength of a material can be defined as the strength of the material in the presence of a crack-like flaw, (29). The causes of damage could be: an impact dent, fatigue cracks, imperfections in the manufacturing process and other causes of damage that may be originated during the maintenance of the structure. Comparing monolithic materials to fiber metal laminates, the FML show a significant increase in the residual strength. The improved residual strength further strengthens the potential of FML for applications where Damage Tolerance properties are the design drivers (28).

But an important property of the FML materials is their impact resistance. As mentioned earlier in this work, the sources of impact damage are many: runway debris, hail stone, dropped tools, bird-strikes and other maintenance damage . Comparing the aluminium alloys to FML, the same plastic deformation and damage is observed, only at higher impact energy levels, (28). For many types of impact the metal constituent the laminate

absorbs a lot of energy by plastic deformation, and, by introducing membrane stresses, the fibres enlarge the affected area, (28). Impact deformation is actually a significant advantage of FML, especially when compared to composites because this visible damage significantly increases inspectability and detectability, (24). In the same work, the authors specify that this impact performance of FML is attributed to a favourable high strain rate strengthening phenomenon which occurs in the glass fibres, combined with their relatively high failure strain damage in severe environments.

3.2 Sandwich Honeycomb Material

The use of a cellular microstrutture to reduce weight and conserve materials is very abundant in nature. The sandwich panel used during the research project is in form of non-metallic light honeycombs that are flexible in the thickness direction and they are prevalently used in structural applications due to the weight reduction and promising high energy absorption. Honeycomb is made primarily by the expansion method.

The honeycomb fabrication process by the expansion method begins with the stacking of sheets of the substrate material on which adhesive node lines have been printed. The adhesive lines are then cured to form a HOBE (HOneycomb Before Expansion) block. The HOBE block itself may be expanded after curing to give an expanded block. Slices of the expanded block may then be cut to the desired T dimension. Alternately, HOBE slices can be cut from the HOBE block to the appropriate T dimension and subsequently expanded. Slices can be expanded to regular hexagons, underexpanded to 6-sided diamonds, and overexpanded to nearly rectangular cells. The expanded sheets are trimmed to the desired L dimension (ribbon direction) and W dimension (transverse to the ribbon), figure (3.4). The corrugated process of honeycomb manufacture is normally used to produce products in

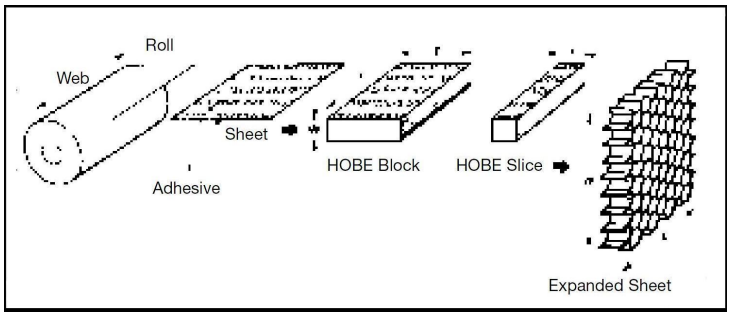

Figure 3.4: Expansion Process of Honeycomb Manufacture

the higher density range. In this process adhesive is applied to the corrugated nodes, the corrugated sheets are stacked into blocks, the node adhesive cured, and sheets are cut from these blocks to the required core thickness, figure (3.5). In particular Flex-Core cell configuration provides for excep-

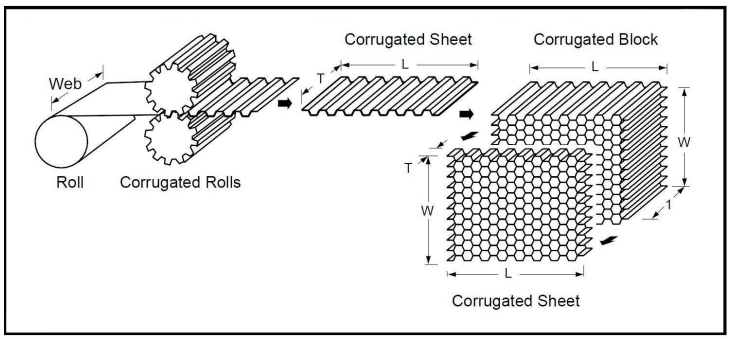

Figure 3.5: Corrugated Process of Honeycomb Manufacture

tional formability in compound curvatures with reduced anticlastic curvature and without buckling the cell walls. Curvatures of very tight radii are easily formed.When formed into tight radii, Flex-Core provides higher shear strengths than comparable hexagonal core of equivalent density. Flex-Core is manufactured from aluminum, Nomex, and fiberglass substrates, (3.6). The Flex-Core honeycomb in Aluminium deforms by plastic buckling and

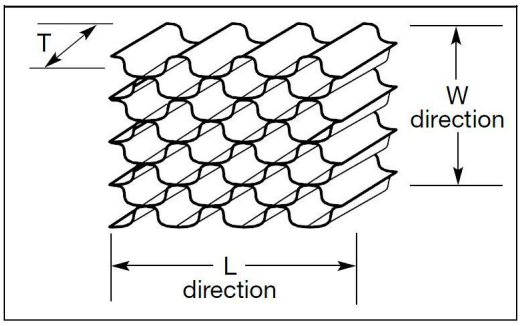

Figure 3.6: Flex-Core cell

are commonly well modelled as elastic, perfectly-plastic materials. In comparison, materials made from random, short fibres embedded in an epoxy matrix tend to fail predominantly by elastic buckling under compressive loading. After buckling, the core does not recover its original buckling strength due to local damage to the short fibres at the kinks and the altered geometry of the cells. The kinks become permanent hinges left in the core material. As a result, these cores are left in a state where the hinges deform from the start of load application. Previous studies of compressive failure in metal honeycomb, (30), has shown that the overall response is generally similar to that of an elastic-perfectly plastic material, especially where the material exhibits lower levels of strain hardening. When the material buckles locally, plastic hinges form and it is here that the bulk of the real inelastic strains are accumulated. On unloading, the small elastic strains are recovered from the plastic material in the neighbourhood of the hinges. In contrast, impacts with a material such as Nomex exhibit more complex behaviour both on loading and unloading. The initial buckling of the core is elastic in nature. As a result, the formation of hinges in the core material decreases its stiffness rapidly due to the geometrical changes that have occurred. The force sustained in the damaged material falls accordingly.

Figure (3.7) shows a typical plot of the nominal stress-strain behaviour

for a honeycomb sample under quasi-static through-thickness compression. From a mechanical perspective the most notable difference between non-metallic and metallic honeycomb structure is the post buckling load carrying capacity. Non-metallic honeycomb loses a large proportion of its stiffness post-buckling. In contrast, metallic honeycomb retains significant load carrying capacity because further deformation requires additional plastic work.

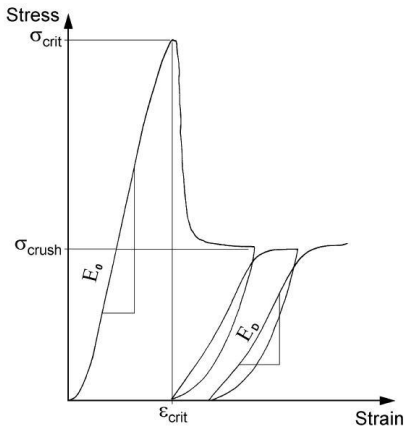

Figure 3.7: Nominal Stress-Strain behaviour of honeycomb core

The fall in this curve represents a decrease in the strain energy as the material buckles. Physically, the material forms a number of local wrinkle sites and begins to deform in a concertina fashion. The material between the wrinkles stores much less elastic energy than the small volume associated with the wrinkles stores a combination of elastic and inelastic energy. Subsequent to the initial buckling, the material exhibits steady crushing. The loading history shown in figure (3.7) can be divided into three regions as follows:

1. Elastic loading to the point where the critical stress, σ_{crit} is reached.

2. Rapid decrease in the apparent stiffness of the core material.

3. Steady crushing, during which inelastic strains accumulate.

During elastic loading, the honeycomb is modelled as an orthotropic solid to account for the large variation in its stiffness in its principal directions. This is valid until the peak stress σ_{crit} is reached is attained. An elastic continuum damage model is used to create the apparent change in stiffness (geometry) of the honeycomb. The main requirements of the damage evolution are that the decrease in stiffness occurs as rapidly as possible and that it causes the same reduction as the experimental samples. A schematic of this damage function is shown in Figure (3.8). Considering figure (3.7), it is clear that buckling happens very rapidly. The change in the stress-strain curve occurs approximately at a fixed strain, when ϵ_{crit} is reached. This is verified experimentally even at low strain rates. Under this assumption and the dominant through thickness elastic properties, the following relationship is developed in equation (3.1):

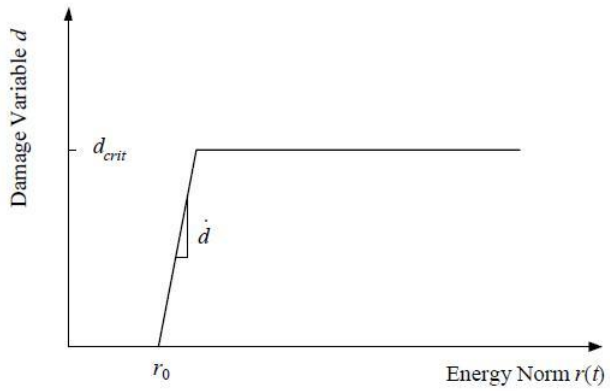

Figure 3.8: Damage Evolution

$$\epsilon_{crit} = \frac{\sigma_{crit}}{E_0} \approx \frac{\sigma_{crush}}{E_D} \tag{3.1}$$

Rearranging equation (3.1), approximate ratio equivalence between the critical stresses and moduli is found (3.2). The stress ratio is related to the damage multiplier, giving:

$$\frac{E_D}{E_0} = \frac{\sigma_{crush}}{\sigma_{crit}} = 1 - d_{max} \tag{3.2}$$

From experimental data, the reduction in stiffness was found to be 60% for typical Nomex honeycomb, giving a modulus ratio of 40%. Subsequent to the reduction in stiffness achieved by the damage accumulation, any further load application should result in steady crushing similar to an elastic, perfectly-plastic material. For a static loading case this would be hard to model using a yield surface criterion. The rapid rise in load during an impact event means that the behaviour shown in figure (3.7) is suppressed. Under these conditions, although the stress in the material is trying to fall, the externally applied load rises more rapidly. Consequently, instead of the behaviour in figure (3.7), under impact conditions the stress level increases until steady crushing occurs. As a result, the damage evolution and the start of the inelastic strains probably start at about the same time. If the damage gradient is sufficiently high, the damage event is completed rapidly and any subsequent increase in load will simply add to the inelastic strain component.

The application the plasticity model post buckling is appropriate for modelling impact with small levels of indentation only. Large levels of indentation may not be modelled well because the plasticity model permits flow that is not characteristic of a crushing honeycomb resulting in excess flow in the ribbon and transverse directions. The isotropic model allows damage to occur under both tensile and compressive loading. Since buckling occurs at much lower load levels compared to tensile failure and to avoid tensile damage progression, the model modified so that damage may only

develop under compression. Damage may only occur when the hydrostatic stress less than zero:

$$\sum_{i=1,3} \sigma_{ii} < 0 \tag{3.3}$$

Under these conditions there is a net compressive state and damage is permitted to progress accordingly.

Chapter 4

Material Characterization

This section describes an extensive series of materials characterization experiments to determine stiffness and strength properties on glass-based FML. At CIRA (Centro Italiano Ricerche Aerospaziali) facilities several tests were performed: static test to determine the stress-strain curve; low velocity impact (from 3.5 to 5m/s) to understand the impact-damage resistance of these novel composites so that they can be designed optimally for impact resistant aircraft applications; dynamic tests at different strain rates at medium rate regime (5m/s to 17.5m/s); and, at least, different impact tests to determine the threshold for impact energy which correspond to visible impact damage. The flat panels of FML were supplied by Alenia, during the tests, two different lay-up have been used, the first lay-up of the plates was A/0/90/A/90/0/A where "A" means a layer of aluminum alloy 2024T3 with a thickness of 0.3mm and "0" and "90" refer to layers of unidirectional glass/epoxy (FML 94-27% - S2 Glass 187-460) oriented in a cross-ply configuration, each glass layers had a thickness of 0.125mm, giving a total specimen thickness of 1.4mm, this test article is called FML 3/2 in this work. The second lay-up of the plates was A/0/90/A where the aluminium ply has a thickness of 0.4mm and the total specimen thickness is 1.05mm, because

of a less number of plies, this test article is called FML 2/1 in this work.

4.1 Static Testing

A static test was performed using a servo-hydraulic frames model MTS-810 equipped with valve to be used to generate a tensile load to 250KN. The equipment and techniques were performed according to ASTM requirements. Figure (4.1) shows the bow-tie specimen used for static test. On each test article a strain gauge (mod.CEA-13-125UN-120) was attached along load direction.

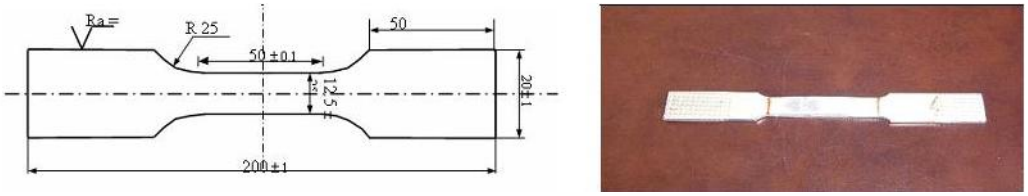

Figure 4.1: Details of FML specimens cut from plates

The tensile static tests showed the results about FML strength property and deformation until to rupture, the stress-strain curve is shown in figure (4.2) and the results are summarized in table (4.1), for both samples.

	Tensile Strength	**Yield Stress**	**Young** E **Modulus**	**Deformation at failure**
	$\sigma_r[MPa]$	$\sigma_y[MPa]$	E [GPa]	$\epsilon_r[mm/mm]$
FML 3/2	631.4	310.3	30.7	0.064
FML 2/1	595.9	338.8	36.3	0.058

Table 4.1: Results about tensile static test on FML 3/2 and FML 2/1

The results showed as glass fibre have a lower elastic modulus compared to Aluminium alloy, depending on the fibre orientations. FML was about

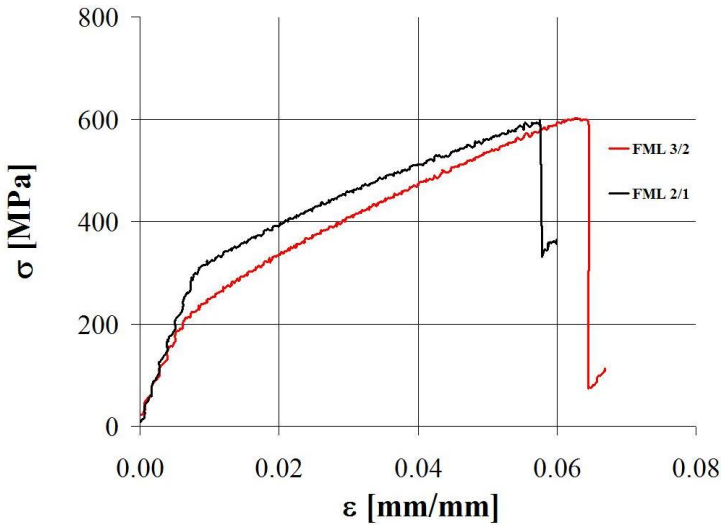

Figure 4.2: Curve $\sigma - \epsilon$ for tensile static test on FML 3/2 and FML 2/1

15% softer, and failure stress was 20% higher than standard alloy Al 2024 for the same thickness.

The figure (4.2) shows the tensile $\sigma - \epsilon$ relation for FML 3/2 and FML 2/1, it can be seen that, in general the FML exhibited a bilinear $\sigma - \epsilon$ behaviour. The initial longitudinal modulus fot the FML 3/2 was found to be 30.7GPa; however, it decreased considerably at a stress level of 310MPa. During the first linear part, both aluminium and glass/epoxy layers are loaded according to their Youngs modulus. After the aluminium starts yielding, the load-carrying capability of aluminium decreased substantially. As a result, the stress-strain curve began to deviate from the initial linear path, but the stress still increased due to the continued reinforcement of laminate by the glass/epoxy plies. Beyond the transition region, the stress-strain relation became linear again since the glass/epoxy composite layer typically exhibited a linear elastic response up to ultimate fracture.

4.2 Dynamic Testing

The main objective of these tests were to investigate stiffness and strength properties at different strain rates on the FML articles. Strain rate $\dot{\epsilon}$ is the rate of change of strain ϵ with time t, defined as in equation (4.1):

$$\dot{\epsilon} = \frac{d\epsilon}{dt} \tag{4.1}$$

The units of strain rate are s^{-1} and they will be used throughout this article. Being ϵ the engineering strain, equation (4.1) becomes:

$$\frac{d\epsilon}{dt} = \frac{1}{L_0}\frac{dL}{dt} = \frac{V}{L_0} \tag{4.2}$$

Where L is length of the specimens of original length L_0, V is the velocity at which the specimens is being deformed. A constant crosshead speed in a mechanical testing machine yields a constant engineering strain rate defined by equation (4.2). The experimental test was performed at a different strain rate, as required by technical handbook (31), with servo-hydraulic machine (model MTS 819HR), equipped with high capacity valves can be used to generate strain rates as high as $500s^{-1}$.

Five strain rates were applied whether FML 3/2 or FML 2/1 coupons. Quasi-static testing was performed a strain rate of around $30s^{-1}$ which yields a strain of 1m/s, the equipment and techniques have been extended to strain rates of 5m/s (150 s^{-1}), 10m/s ($300s^{-1}$), 15m/s ($450s^{-1}$) e 17.5m/s ($500s^{-1}$). The results from the tensile tests for elastic properties are summarized in table (4.2) and plotted in figure (4.3).

The results show that yielding stress increases with strain rate ($d\epsilon/dt$). This is related to a lower rupture deformation and toughness. The FML 2/1 presents the maximum yielding stress at 10m/s, whereas the FML 3/2 presents maximum yielding stress up to 17.5m/s, generally FML 3/2 showed higher resistance.

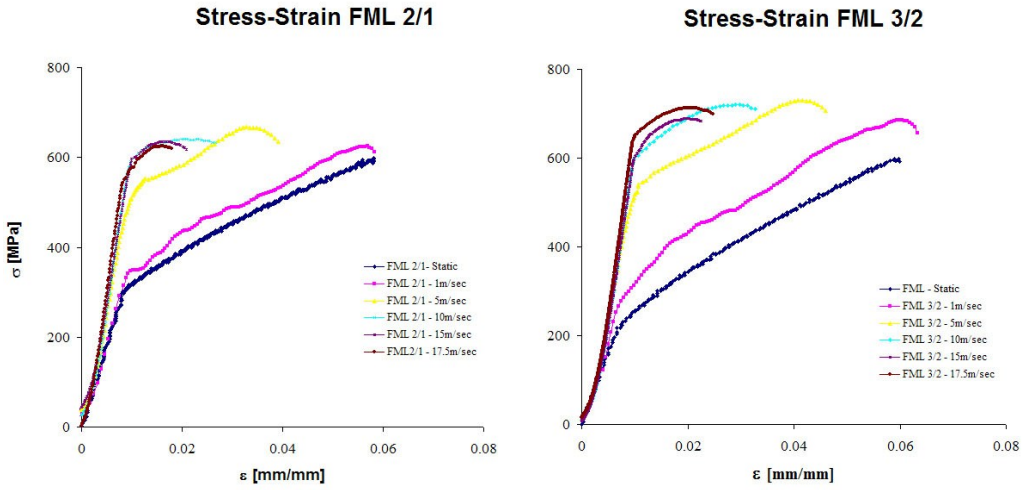

Figure 4.3: Curve $\sigma - \epsilon$ at a different $\dot{\epsilon}$ on FML 2/1 (left) and FML 3/2(right)

	Max Stress $\sigma_{max}[MPa]$	**Max Strain** $\epsilon_{max}[mm/mm]$	**Yielding Stress** $\sigma_y[MPa]$
FML 3/2 - 1m/s	711.8	0.062	316.3
FML 3/2 - 5m/s	719.3	0.042	551.0
FML 3/2 - 10m/s	729.3	0.029	614.3
FML 3/2 - 15m/s	691.1	0.023	627.3
FML 3/2 - 17.5m/s	715.9	0.020	651.1
FML 2/1 - 1m/s	630.9	0.055	358.8
FML 2/1 - 5m/s	647.3	0.033	539.2
FML 2/1 - 10m/s	635.3	0.023	589.9
FML 2/1 - 15m/s	631.2	0.020	571.0
FML 2/1 - 17.5m/s	605.3	0.018	571.1

Table 4.2: Experimental results on FML for different strain rate

For the dynamic tests a rate increase from quasi-static to $500s^{-1}$, resulted in an increase in ultimate load capacity (tensile strength) from 631MPa to 715MPa (10%). However, no increase strain rate on ultimate strength is consistent with the findings of Vlot, (32), who tested a similar cross-ply glass-based fibre metal laminate at a quasistatic rate and a rate of 20 m/s. Vlot found an increase in strength of 11% in going from the quasi-static rate to the higher rate. Examining the strain rate time history it is noted that the yielding stress increases from 310MPa (at a quasistatic test) at 651MPa (at a rate of 17.5m/s), this increasing of 110% suggests the strain rate strongly influences the yielding strength and the glass layers are the main contributors to the strain rate effects. Supporting evidence for this can be found in the literature, (33).

4.3 Low velocity impact

The low velocity impact tests were performed at department of Mechanical Engineering at University of Bath, and main goal of those tests is to present and discuss some experimental results obtained during a low velocity impact testing campaign conducted on glass fiber epoxy matrix laminate plates. The impact behaviour of this particular class of composite material is then analyzed from an energy viewpoint, by means of two parameters: the indentation and the damage degree of a plate specimen subjected to a drop-dart test according to the ASTM standard, (34). Those localised low-velocity impact events that might occur during the in-service life or maintenance have been identified as very hazardous, as they can result in internal damage such as delamination and back face splitting which can reduce the residual strength by as much as 60%, (35), compared with the strength of an undamaged specimen. Although those impacts are barely visible, the strength and

reliability of the structure is affected. Hence great attention has been given to the behaviour of composite structures under those impacts.

During the test, the velocity of the impactor, along the stages was in the range of (3.6 m/s - 6.1 m/s). The impactor mass was constant at 0.746 kg. Those impacts can represent real life situations such as dropped tools during repairs or manufacturing, runway debris and hail stones.

The impact is a dynamic event which can be characterised by three stages:

- Just before impact.
- Contact/Impact.
- Just after impact.

For the purposes of the tests the velocities for stage first, V1 and stage last, V3 were captured, while zero velocity was assumed when there is the contact. During impact the kinetic energy of the impactor mass is dissipated by the composite specimen, through deformation, heat and sound.

The composite specimens consist of three materials with different properties:

- Aluminum.
- Glass fibers.
- Resin or cohesive.

So in the dynamic process of impact the aluminium may deform plastically but fracture within the specimen may occur to the fibers or in the cohesive zone. According to (36). Internal damage in laminated composites can be divided into three categories: interlaminar damage (delaminations), interlaminar damage between fibres (splitting, transverse ply cracking) and interlaminar damage involving fibre fracture. Matrix damage is the first

type of failure induced by transverse low-velocity impact (26), as it involves less energy dissipation than fiber fracture. Moreover manufacturing imperfections produce stress concentrations which may act as crack initiators by concentrating stress in those weak areas of the laminated structure (37).

The Fiber Glass Aluminium Laminate tested, was fabricated at (Alenia), using 7475 T761 aluminium sheets 0.3 mm in thickness and glass fiber 0.125 mm in thickness for aerospace applications. The stacking sequence of the layers was [7475 T761/glass 0 degrees /glass 90 degrees /7475 T761/glass 90 degrees/glass 0 degrees/7475 T761], where 7475 T761 indicates an aluminium layer and 0 and 90 is the fiber glass layer orientation. Unfortunately some of the the material properties were not provided. For modeling purposes, the missing material properties were replaced by very similar properties found on papers (38). The properties used are provided in table (4.3) and table (4.4).

Material	**E11**	**E22, E33**	**G12, G13**	**G23, G23**	$\nu 12$, $\nu 13$	$\nu 23$	**Vf**	ρ
	$[GPa]$	$[GPa]$	$[GPa]$	$[GPa]$				$[kg/m^3]$
Glass	48	15.3	5.1	5.8	0.315	0.332	0.65	2000

Table 4.3: Elastic properties of glass/epoxy

Material	**Young's Modulus** [GPa]	**Poisson ratio**	**Density** $[kg/m^3]$	**Yield Strength** [MPa]	**Thickness** [mm]
Aluminium	71	0.3	2780	280	0.3

Table 4.4: Elastic properties of Aluminium

The square samples with a size of 80 mm x 80 mm are clamped between two plates with a circular opening with a diameter of 70 mm, figure (4.4).

The four clamps ensure clamped boundary conditions of the tested area. The low velocity experiments were performed with a drop weight impact tester, with an impactor mass of 0.746 Kg. In the impact tests, each specimen was subjected to a single impact test. The instrumentation required for the tests consisted of: a strain gauge meter within the impactor to measure the strain in the specimen, an oscilloscope, an amplifier and a high speed camera to measure the velocity of the impactor.

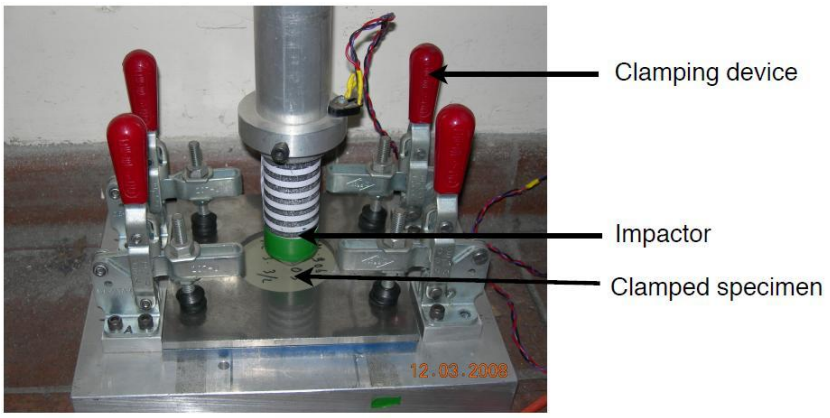

Figure 4.4: Specimen Clamping device

The impactor tip was a hemispherical indentor of 11 mm diameter, which is dropped from eight different heights to characterize eight different impact energies.

In the table (4.5), the velocity values from the experiments have been also given in energy values assuming that all the energy before and after the impact is kinetic. The difference of the two energies in each stage is roughly the energy absorbed by the specimen figure, (4.5). The energy absorbed tends to grow as the stages of the test increase. It has to be mentioned that during the experiments inaccuracies may have occurred as the quality of the test rig was not the highest.

Stage Number	**Before Contact velocity v1 (m/s) energy)**	**Rebound velocity v3 (m/s) energy)**
1	3.6 - (4.83J)	2.3 - (1.97J)
2	4 - (5.96J)	2.652 - (2.62J)
3	4.23 - (6.67J)	2.9 - (3.13J)
4	4.42 - (7.28J)	3.24 - (3.91J)
5	4.8 - (8.59J)	3.62 - (4.88J)
6	5.1 - (9.7J)	3.83 - (5.46J)
7	5.28 - (10.39J)	4.1 - (6.27J)
8	3.5 - (11.28J)	4.2 - (6.58J)

Table 4.5: The impact velocities meausered before and after the impact

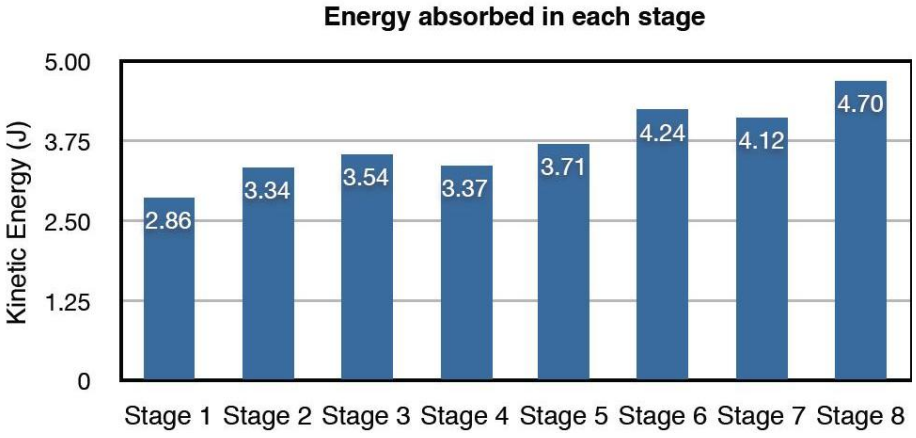

Figure 4.5: Energy absorbed by the specimen during the impact

After the testing the specimens were examined using both non-destructive and destructive techniques, to investigate the damaged zone.

Two *non-destructive methods* were used:

1. To measure the dents on the surface of the specimens a Pro Scan laser scanner was used. The laser beam scanned the damaged zone and 3-D plots were produced, showing the deformed area.

2. A C-scanner was employed to inspect the specimens. The principle is to measure the first arriving acoustic wave that is sent at a straight angle through the test object. This technique is especially suited for detecting air pockets and distributed air inclusions, such as delaminations and porosity in laminates. The C scanner couples the ultrasound into the material using water jet probes. The detected peak values in the transmission signals are stored on computer disk and may be visualised. With this method very accurate defect sizing is possible but not defect depth. Unfortunately the ultrasonic method was not adequate to determine the extent of the damage within the specimen due to the fact that surface dents caused by the impact, scatter portion of the ultrasonic beam, reducing the accuracy of the measurements. Furthermore the acoustic impedance of the materials (fiberglass and aluminium) is very different and that made the process more difficult. It was possible to solve this problem by removing the aluminium layer from the specimen and then examine it, but not all the specimens could be destructed.

The *destructive methods* employed, was the cross sectioning of the specimens across the damaged area and then the configuration of damage was observed with a metallographic microscope. This method permits to inspect the damages in cross-section with the microscope:

- Fiber crack.
- Resin crack.
- Fiber resin separation.
- Delamination.
- Fracture of metal layer.

Moreover the overall damage length was measured and compared with the previous techniques. The specimens before the inspection had to be divided into resin, which had dried and polished and then the specimens were ready to be inspected with the metallographic microscope. With the laser scanner the depth of the indentation was measured, table (4.6).

Stage/ Energy	**Indentation Depth**
1/(4.83)	1.093
2/(5.96)	1.28
3/(6.67)	1.31
4/(7.28)	1.396
5/(8.59)	1.59
6/(9.7)	1.613
7/(10.39)	1.98
8/(11.28)	2.064

Table 4.6: The depth of the dent for each stage of impact

The indentation depth increased as the Energy/velocity increased, but the rate of increase clearly decreased with increasing Energy. A graph, figure (4.6), plots the dependence of dent size on the impact velocity. The continuous curve, drawn by hand, evidences the trend of the experimental data.

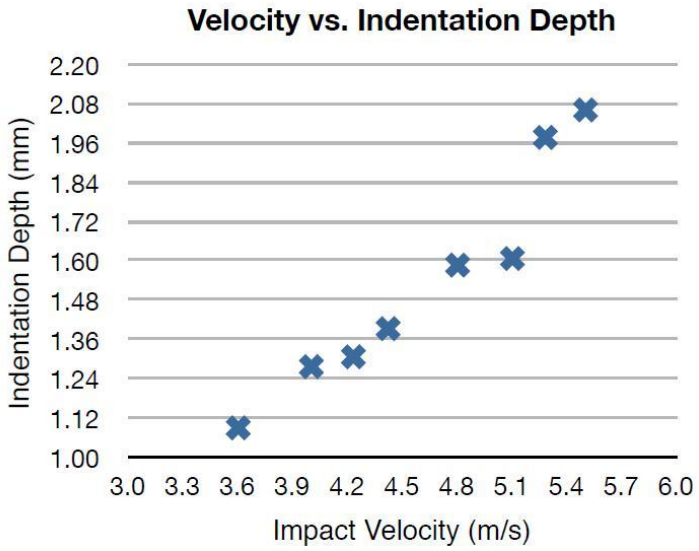

Figure 4.6: Dent size dependance on impact velocity

The sample impacted at the lower value of energies presented a characteristic *hat-shaped* distributuion of damage along the thickness direction, which was found with the aid of the laser scanner, (4.7) and (4.8)

The permanent deformation of the specimen was not limited just to the impact location zone, due to the plasticity of the aluminium layer. In addition by comparing the damage extent in the impact side and in the layers far from that, it was clear that the damaged area was much smaller in the first side than the second figure (4.9).

For this sample also destructive techniques were applied, figure (4.10). The photos were taken from the metallographic microscope. Cohesive failure and the delaminations at the top and bottom layers are observed between the fiber layers. There is possibly fiber fracture in the marked area. Considering that this was the lowest velocity impact, the damage occurred was quite significant. The cause was probably the manufacturing imperfections which act as crack initiators, (39). However such an observation is not certain as

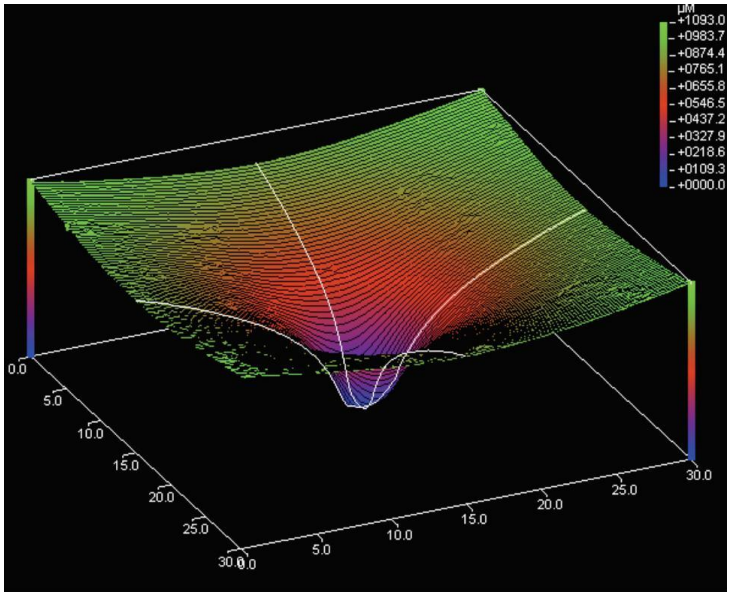

Figure 4.7: 3-D Laser-Scanner plot for specimen

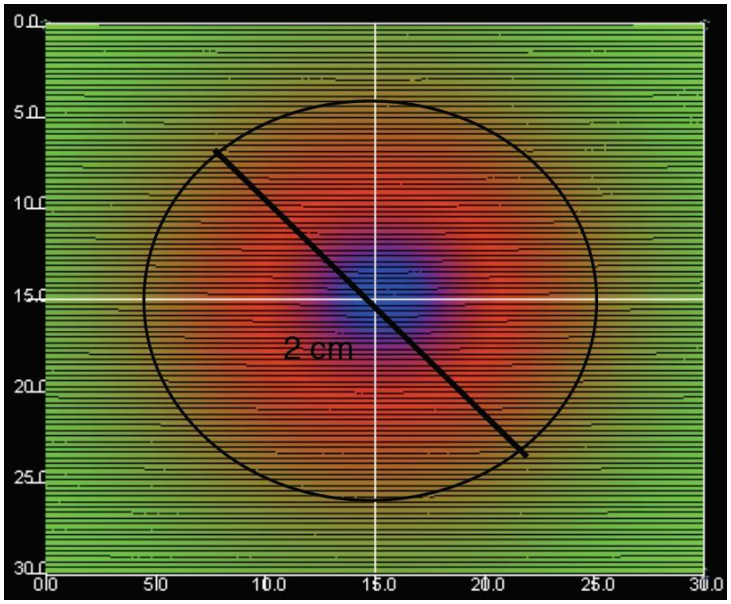

Figure 4.8: 2-D Laser-Scanner plot for specimen 1

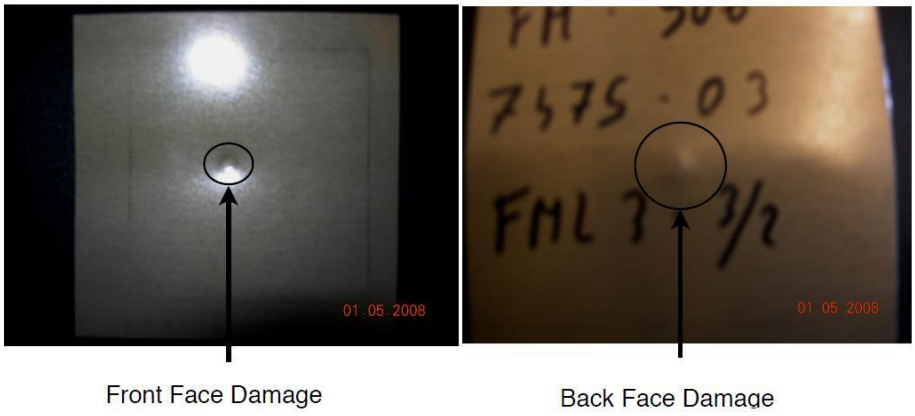

Figure 4.9: Front and back face damaged area comparison

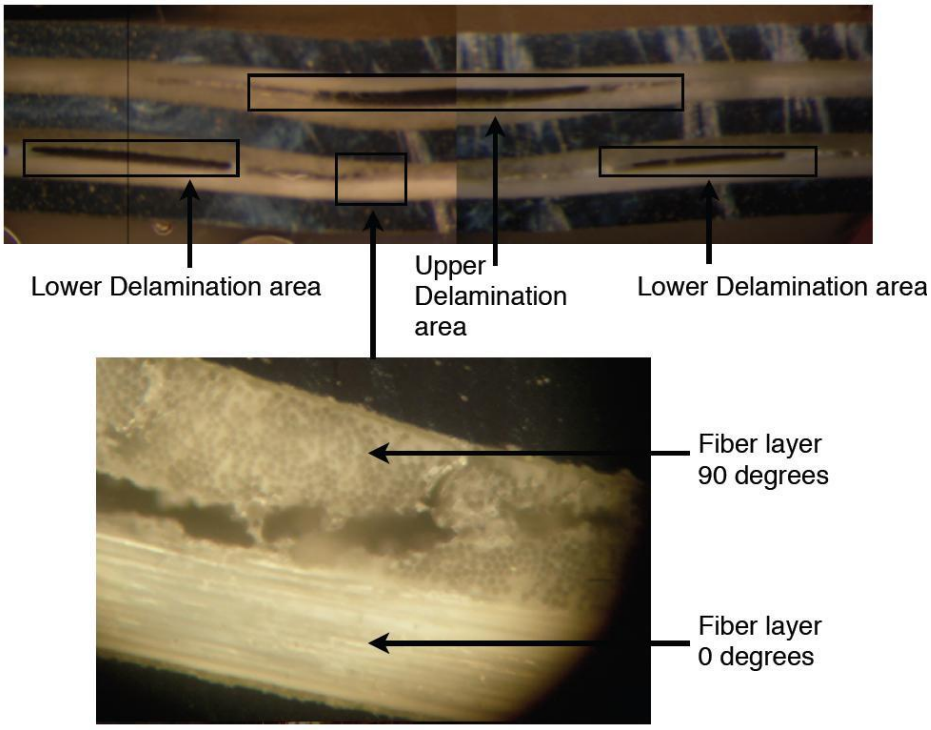

Figure 4.10: Metallographic photographs shows the internal damage of the specimen, obtained from the cross sectioning technique

possibly resin covers the 90 degree fiber layer. More increasing the impact energy and more damage extends. Analyzing the sample impacted at the maximum value of energy with the C-Scan method, it can be noted the shape of deformation has an elliptic shape, figure (4.11), and the damaged area was calculated at 6.6 cm^2. Then the same sample was subjected to destructive technique, figure (4.12), the interlaminar damage was found as cohesive failure and delaminatons were observed between both fiber layers. This damage mode generally occurs much later in the fracture process than matrix cracking and delamination, and there is less information on this area. This type of damage arises at higher impact energies from those applied on the current tests. Moreover fractured cohesive, blocks the clear image of the fiber layers. The three areas of delamination observed, were only between the fiber layers. The separation size was significant for this low velocity impact. By examination of the strain vs. time plots of all the experimental stages, it was identified that the same response was recorded for all the stages but with a different magnitude. Since all the specimens had identical properties and the only variable during the testing was the impact velocity, the same response was expected. The sequence of events for all the stages was:

- Cohesive cracking of the top layers.
- Aluminium layer plastic deformation.
- Delamination and cohesive cracking at lower layers as well as layer separation growth.

The $hat - shaped$ distribution of damage was profound in all the stages. The indentation depth and the diameter of the damaged area was increasing as the impact velocity increased. Moreover the damaged area of the impacted side was clearly smaller than the damaged area of the back wall of all the sample. The cross-sectioning method was very important as it was the only

technique where the internal damage could be observed. The two samples examined showed the same damage characteristics. Cohesive failure and delaminations were observed in both cases. The cohesive failure and the layer separation in the upper layers, was due to the compressive stresses acting in the impacted layer. The separation between both upper and lower fiber layers was larger for sample characterized by higher impact energy and the separation increases as the velocity of the impact increases. Fiber failure may also be present but such phenomena is not certain as the damaged area was covered by the fractured resin and no clear view was available. At conclusion of this activity it is possible identify declare that even though the damage can be easily visually identified, in the case that such damage has not been detected, the damaged area can be considered as a major crack initiator and the strength and reliability of the structure is greatly affected. Impact on composites is a complex problem largely due to the following points.

- Large deflections and shear deflections and membrane effects are usually significant
- Local forces under the impactor give non-linear contact behaviour
- Impact is a dynamic event
- Damage modes are numerous and interacting, including internal delamination, surface micro buckling, fibre fracture and matrix degradation
- The response and damage modes are sensitive not only to the exact nature of the composite, but also to the many impact parameters.

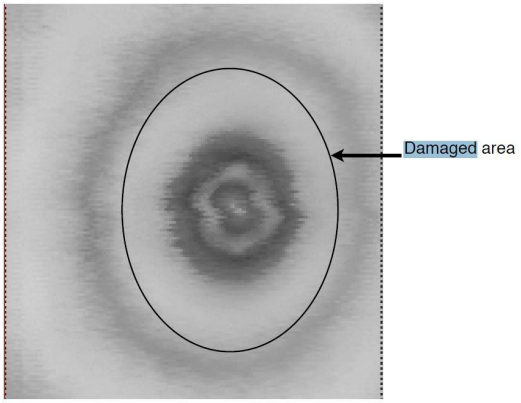

Figure 4.11: Damaged area measured with the C-scan technique

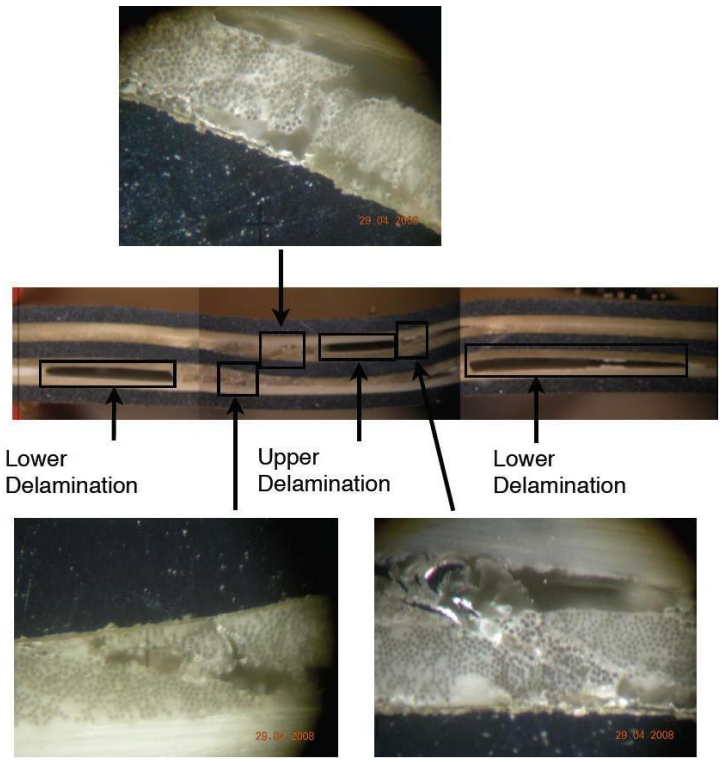

Figure 4.12: Metallographic photographsque

4.4 Impact Testing

The main objective of the impact tests was to investigate the behaviour and the damage resulting from low-velocity. The impact test were carried out using Fractovis (CEAST) Drop Weight Impact Machine. The impactor chosen for this work was a cylindrical steel bar with a hemispherical tip to prevent unwanted penetration. The impactor has a diameter of 20 mm with a mass of 7 kg. During the test, a clamped sample is hit by a striker of mass M at the certain initial velocity v_0, as shown in figure (4.13), during this event three variables are recorded: the force F, the time t and the initial velocity v_0.

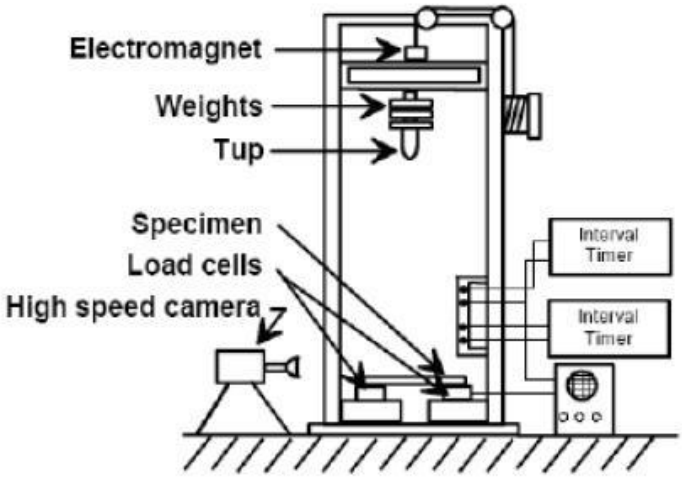

Figure 4.13: Schematic drawing of the falling-weight system

The impact tests were carried out on FML 3/2 and FML 2/1 panels, the FML test panels dimensions were 75 mm x 75 mm. Nine impact tests were carried out repeatedly at increasing input energies defining a height onto the required impact location of the test panels, in order to achieve the required

impact energy, the energy were 15, 25 and 60 Joule for FML 3/2 and 15, 25 and 40 Joule for FML 2/1.

In the first stage, when the impact is relatively low (15 Joule), the delamination increases less for a certain amount of increasing energy. When the plates were impacted with 15 Joule, whether FML 3/2 plate or FML 2/1 plates no obvious damage was observed, however the FML 3/2 presented a deformation higher than FML 2/1 deformation, this is due to higher bending stiffness for FML 3/2 plate than FML 2/1.

During the second test, where the impact energy is relatively high (25 Joule), the complexity of the damage can be appreciated with diffused bending, fracture in the bottom aluminium alloy figure (4.14) and delamination in the upper interface.

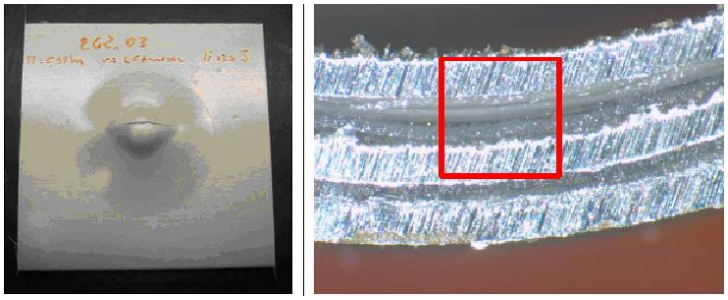

Figure 4.14: Ply cracking (left) and delamination (right) of a plate FML 3/2 after an impact energy of 25Joule

During the third impact test, the impact energy reached 60 Joule for FML 3/2 and 40 Joule for FML 2/1. These tests had essentially the purpose of measuring the maximum energy absorbable by the coupon. The figure (4.15) compares the minimum impact energies which evidence first failure. FML 3/2 shows higher resistance to cracking than non-clad 2024-T3, (24) and than FML 2/1. This impact performance of FML is attributed to a favourable high strain rate strengthening phenomenon (40), which occurs in

the glass fibres, combined with their relatively high failure strain figure (4.2).

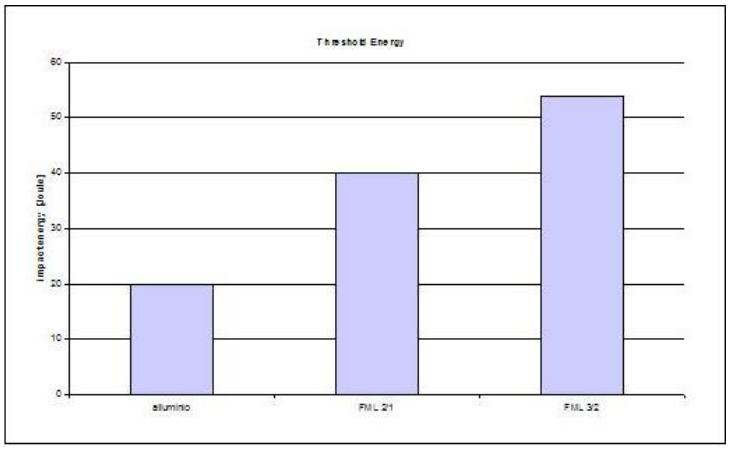

Figure 4.15: Impact property of Fiber Metal Laminate

4.5 Lock-In Thermography Testing

Lock-In thermography allows to detect fastly and reliability defects in components. Thermal waves are used as probes to reveal local material inhomogenities thereby indicating subsurface faults in the examined material. However, there are basic limitations concerning the detection of hidden defects in thick materials with thermal waves: the penetration depth and thus the depth range of thermal waves is limited and depends on thermal diffusion length. This limitation can be turned into an advantage if several thermal waves with different wavelengths are used: one can achieve depth resolved imaging of a component. After dealing with artificial samples the long pulse technique will now be applied to a realistic example. Fibre reinforced materials are sensitive to impact damage which is often only barely visible at the sample surface. However, inside the sample or at its rear surface a serious

damage may occur. The detection is performed on the samples FML 3/2 with dimensions 75 mm x75 mm, which were used during the impact tests at low energy and where the impact energies are 15 and 25 Joule, i.e. before that the sample is perforated. A lock-in image of a specimen with low impact damage is illustrated in figure (4.16), it shows the sample before to the impact so to correlate the pattern when the sample is impacted. The phase analysis is characterized by a long pulse measurement with an evaluation frequency of 0.1 Hz. This frequency value allows to identify the fibre orientation of 90 and it is possible to identify a resin concentration in the middle sample.

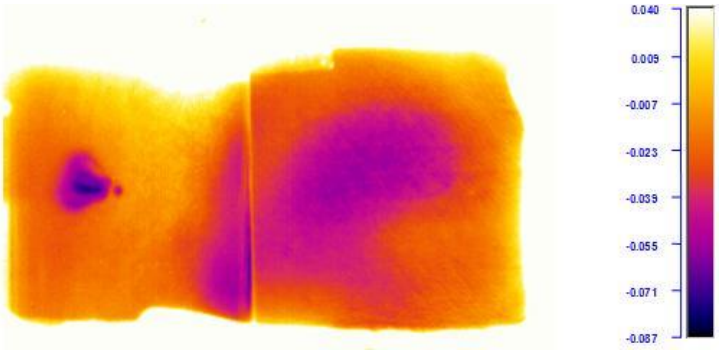

Figure 4.16: Fiber Glass with presence of resin concentration, f = 0.1 Hz

When the sample is impacted with a low energy (1 J), it is necessary to use a frequency of 0.025Hz to identify the impact track on the sample, figure (4.17). In figure it can seen the track of the impactor on the sample and how the damage extends on the large areaeven if the impact energy is lower and any damage is apparent. When the impact energy increases (25 Joule), the panel is not perforated but in figure (4.18) appears a typical butterfly pattern with a lower evaluation frequency. The damage pattern appears more diffuse, but the apparent damage remains the same; figure (4.18) shows also deeper-located damage areas at an analysis frequency of 0.1 Hz, where the damage

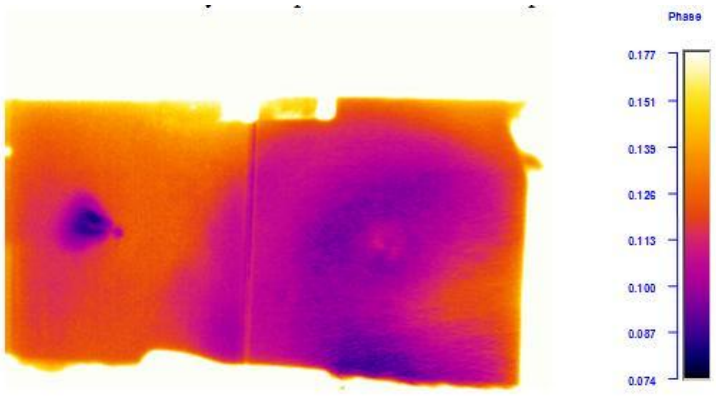

Figure 4.17: Fiber Metal Laminate impacted at 1 J, f = 0.025 Hz

is concentrated on the outer aluminium ply and the damage area appears more large than the impact at 1 J. When the phase analysis is characterized

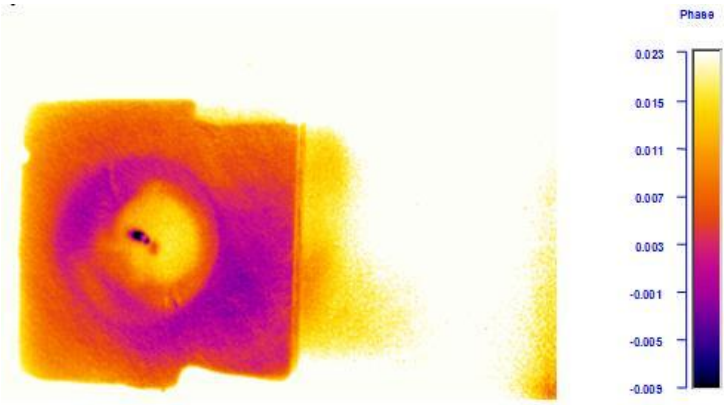

Figure 4.18: Fiber Metal Laminate impacted a t 25 J, f = 0.1 Hz

by a long pulse measurement with an evaluation frequency of 0.025 Hz, the damage appears only as delamination of the fibres near the surface, figure (4.19). This is due to the fiber contribution, which extends the damage involving a large part of the sample, but this results explained that when

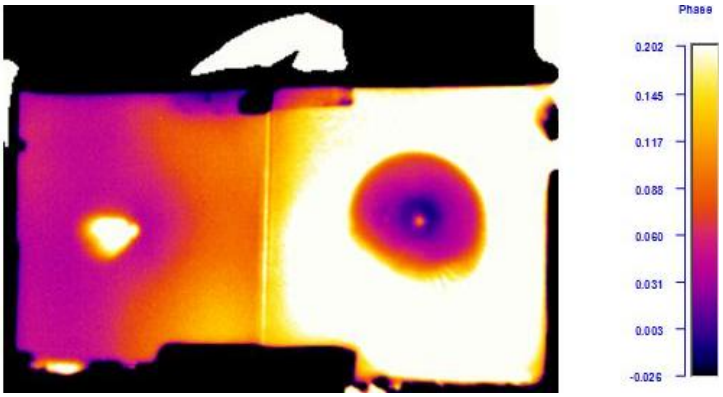

Figure 4.19: Fiber Metal Laminate impacted a t 25 J, f = 0.025 Hz

the damage is barely visible or totally absent the damage can be extended and different plies of a composite react absorbing a different level energy.

4.6 Characterization For Fastener Design

Usually, the failure behaviour of a structural joint is obtained using static loading conditions or an analysis based on a static collapse process. Often, for the purpose of design, the rupture of a joint is assumed to be independent of rate effects: in reality this is often not the case. Under rapid collapse in a crash situation, the behaviour of a joint can be very different to that of the statically loaded case. The immediate implications of this are that, without detailed knowledge of the dynamic failure and collapse of a joint system and material, the prediction of the failure load and energy absorption capability of a structure are subject to error. For this reason it has been necessary to estimate the static and dynamic behaviour of two different types of joints to consider the fittings at connecting the leading edge skin to the ribs.

The aim of this tests was to evaluate the behaviour related to two different joints, see figure (4.20), the first type of joint is a countersunk head rivet in

aluminium alloy, named CSK, see figure (4.21), the second one, figure (4.22) shows a titanium Hi-lock joint.

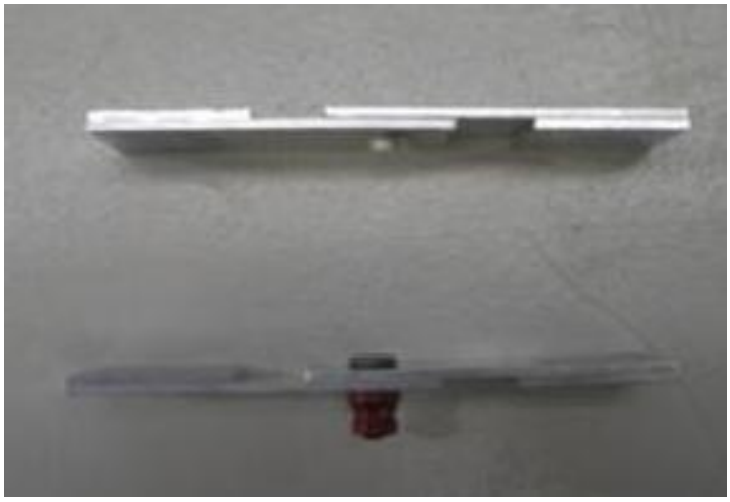

Figure 4.20: Two joints: aluminium CSK (up) and titanium Hi-Lock (down)

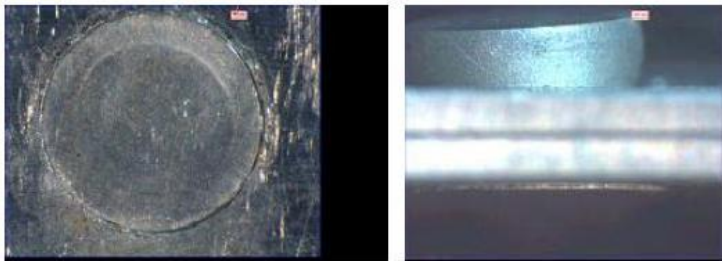

Figure 4.21: CSK Aluminum joint

These joints connect two aluminium sheets with a thickness of 2 mm, as shown in figure (4.23).

The joints in question likely result in a non-perfect contact between the two metal contact strips, and the evidence is collected by images using a stereo-microscope, which measured the distance between them equal to $130\mu m$ related to Hi-lock, and $180\mu m$ about CSK.

Figure 4.22: Titanium Hi-Lock joint

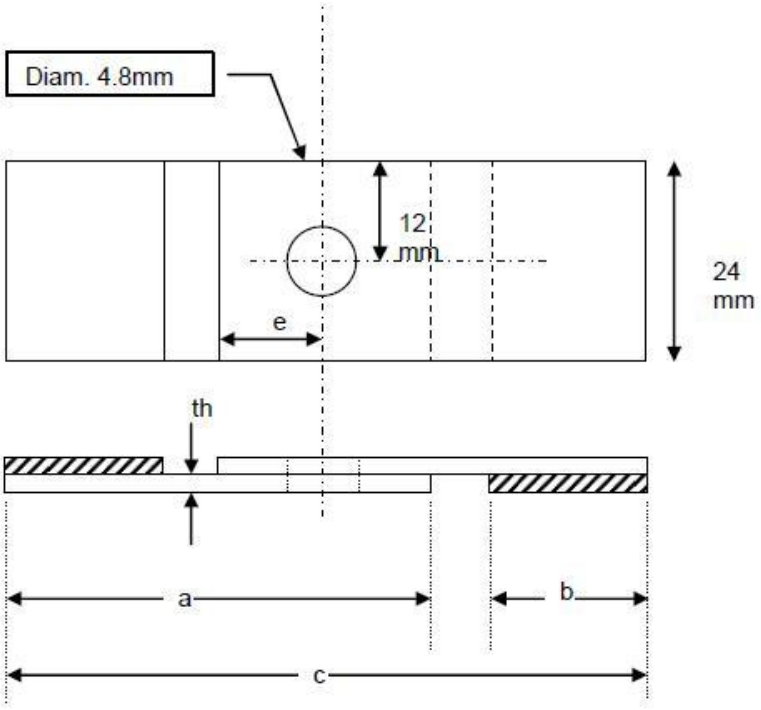

a =	55	mm
b =	24	mm
c =	90	mm
e =	9.6	mm
th =	2	mm

Figure 4.23: Geometry of the samples

For this samples different tests were performed:

- Static test.
- Dynamic test at 1m/s.
- Dynamic test at 5m/s.
- Dynamic test at 17.5m/s.

For each of the speeds and for each of the materials examined, different tests were performed in order to obtain sufficient statistical variation of data.

During the static tests the curves $\sigma - \epsilon$ were plotted in figure (4.24) and (4.25), that presented an ultimate load of 4.73KN for CSK joints, and 7KN for Hi-Lock joints. It is possibile to distinguish for both curves a non linear slope, this trend is associated with the fact that a flexural load is in combination with the traction load.

About the aluminium foils jointed by CSK joints, in figure (4.26) it can be seen that two aluminium foils separated creating a yielding and a misalignment of the fitting but the joint presented any visible rupture.

The Hi-lock behaviour is different related to the CSK joint, the alluminum foil starts to deform plastically at free after the joint; then the rivet begins to bend causing cracks along the hole and this generates the bearing, figure (4.27). An analysis of the section of the cross section of the Hi-lock joint shows how the fracture was caused by the separation of metal grains. This causes the production of pores and voids in large quantities uniting to form a surface fracture apparently due to “dimple”, reflecting the voides and close elevations “ torn ridge”, due to the high plastic deformation.

When the dynamic tests were performed at 5m/s, the curve stress-strain showed that at the maximum load the joints istantaneous breakes, the mode failure was a shear out of the joint with little bending of the aluminium foils. The CSK joint is subjected to a load off the plane which facilitates

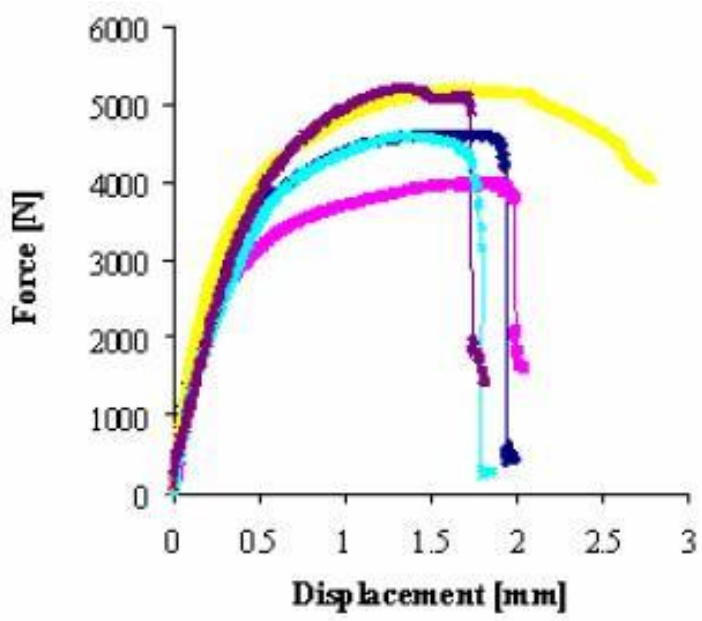

Figure 4.24: Curve $\sigma - \epsilon$ recorded during the static test on the CSK joints

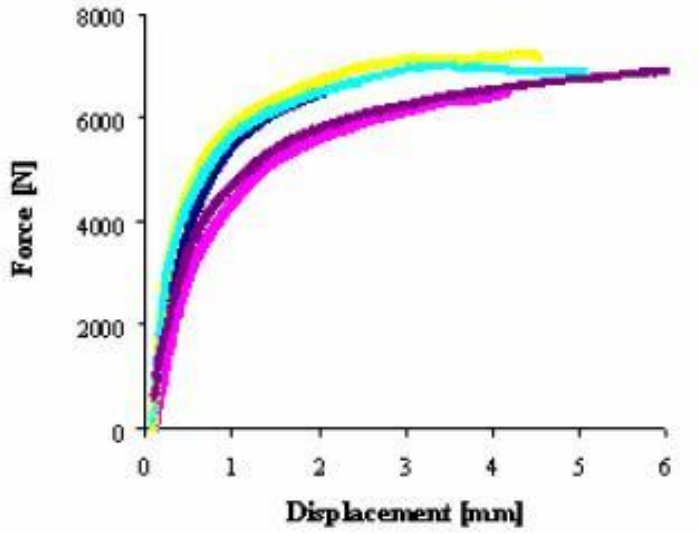

Figure 4.25: Curve $\sigma - \epsilon$ recorded during the static test on the Hi-Lock joints

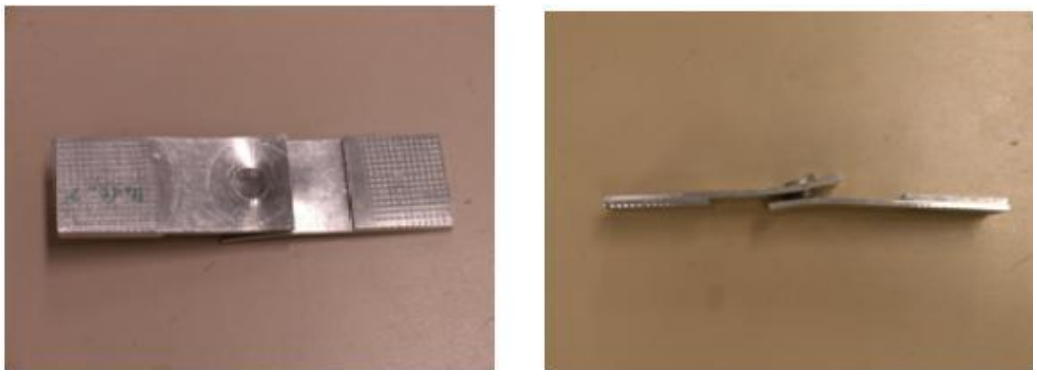

Figure 4.26: CSK joint after static test

Figure 4.27: Hi-Lock joint after static test

the escape from the hole, figure (4.28); then the breaking is due to shear while any bearing is present like so the static tensile tests. About the Hi-Lock joint, a tearing is clear and the aluminum ply completely break, as demonstrated by the figure (4.29), while the titanium joint is intact and continues to maintain its role of connecting metallic plates

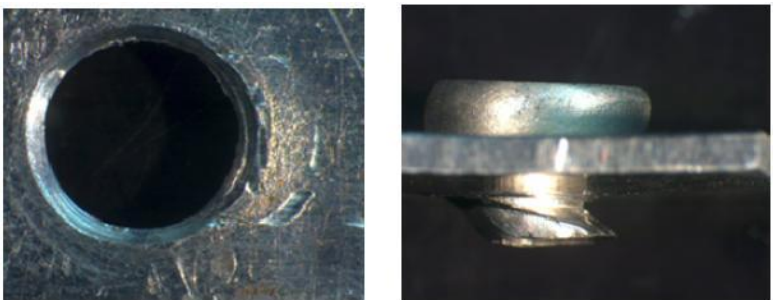

Figure 4.28: CSK joint subjected to the dynamic test at 5m/s

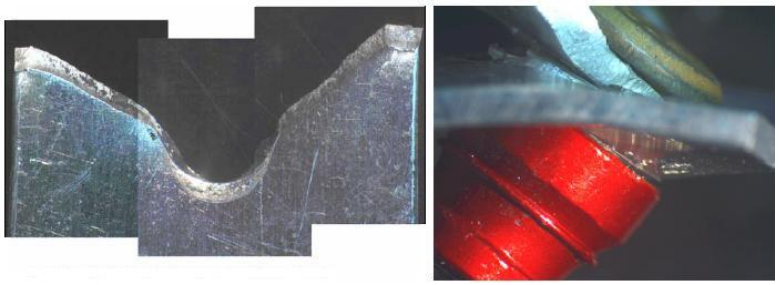

Figure 4.29: Hi-Lock joint subjected to the dynamic test at 5m/s

When the dynamic test were performed at 17.5m/s, the CSK joint breakes because of it escapes from the hole causing the separation of two elements with small cracks around the hole. The aluminum joints is deformed and its axis is tilted by the load traction, see figure (4.30). For the titanium Hi-Lock joint, figure (4.31) again the break caused by the failure of aluminum

ply around the rivet. The hole is partially bearing, and it is known as the flexural load has determined the deformation of aluminum ply.

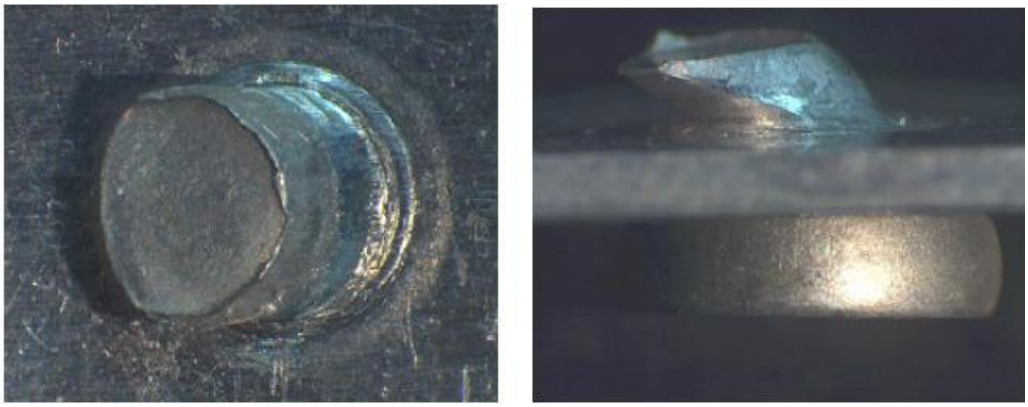

Figure 4.30: CSK joint subjected at dynamic test at 17.5m/s

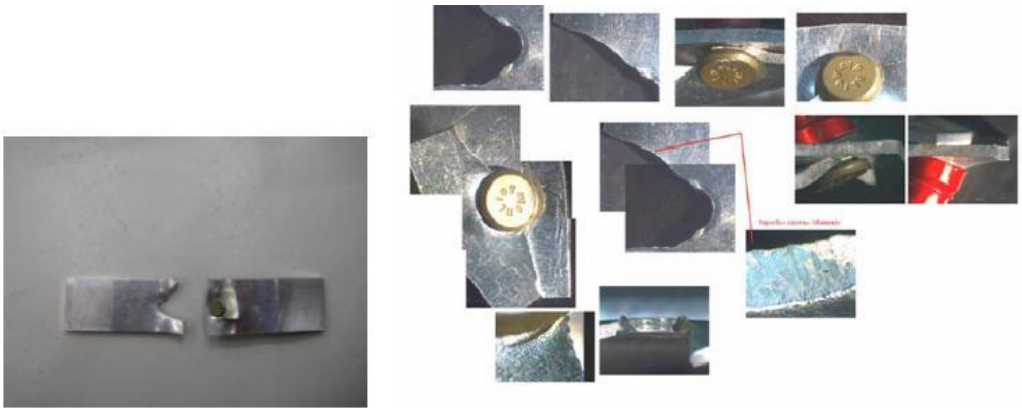

Figure 4.31: Hi-Lock joint subjected at dynamic test at 17.5m/s

Table 4.7 shows the results of tests conducted at different speeds of deformation. It notes that, in general, with increasing of the load speed, the ultimate load tends to increase. It is interesting to note that the load-displacement curves for these two modes of failure, although similar in shape,

	Max Load $F_{max}\,[KN]$
CSK - static test	4.73
CSK - 1m/s	4.54
CSK - 5m/s	4.61
CSK - 17.5m/s	5.11
Hi-Lock - static test	7
Hi-Lock - 1m/s	6.80
Hi-Lock - 5m/s	7.47
Hi-Lock - 17.5m/s	7.82

Table 4.7: Test Results

have different values of peak load and displacement to failure. These curves serve to indicate further differences between the static and dynamic failure of the same joint system. Obviously, these elemetal joint characteristics can influence global collapse behaviour of the structure, especially when considering that a real structure is usually formed by various rivets under different arrangements. The results showed several meanings, however, the fractographic test has allowed the identification of these types of break. In particular for aluminum joints CSK, these generally come out beyond the housing hole, and thanks to high-speed camera, it possibile to confirm that any plasticities and bearings are present along the hole. In the case of Hi-lock joints, those does not show any structural failure and the breaking is due to failure of metal ply.

Chapter 5

Failure Criteria of Materials

5.1 Aluminium Alloy

The material law used for the aluminium alloy was an isotropic elastic plastic model, where it has defined a bilinear yield model with isotropic hardening, using the von Mises yield criterion with a plasticity algorithm that includes the strain rate effects. The strain rate dependency was included in the material law for the aluminium alloy layers. Cowper-Symonds law was used as the elastic-plastic formulation to consider strain rate sensitivity at medium rate regime:

$$\frac{\sigma_n}{\sigma_y} = 1 + \left(\frac{\dot{\epsilon}}{D}\right)^{\frac{1}{P}} \tag{5.1}$$

where σn is the dynamic stress, σy is the static yield stress, and ϵ is the equivalent strain rate. D and p are constant in Cowper-Symonds rate enhancement formula equal to D=1.28E+5 s^{-1} and p=4.0, (41). The material properties are reported in table (5.1).

The failure strain has been defined at 18%, thanks to a study reported in (42), which gave gave the maximum strain for 2024-T3 under uniaxial

Young Modulus [GPa]	**Yield Stress** $\sigma_y[MPa]$	**Ultimate Strength** $\sigma_R[MPa]$	**Failure Strain** [%]
72	2.08	385	18

Table 5.1: Aluminium Alloy Material Parameters

tensile loading as 18%, so this was implemented via the isotropic damage law within the code. For this reason the used failure model is the one that is based on a maximum equivalent plastic strain. The material fails completely when the plastic strain reaches beyond the defined limit. The element no longer carries any load and is removed from the calculation.

5.2 Fiber Metal Laminate Material

The fiber metal laminate presents as a composite material, in this way for the FML composite face plates, the "orthotropic material model" was used in shell elements to build a multilayered composite element. The material describes the elastic behaviour of brittle material with failure based on the interactive stress criteria of failure per mode. It includes the effects of directionality in the material stress-strain response allowing a different fiber orientation to be specified at each through thickness integration point for shell elements. Unidirectional laminated fiber composite shell thickness, each unidirectional layer (lamina) fiber orientation, and unidirectional layer constitutive constants are required as input by the user.

The elastic stress-strain relation between the fiber and matrix stresses and strains is formulated as where the properties and the corresponding:

$$\begin{bmatrix} \sigma_{11} \\ \sigma_{22} \end{bmatrix} = \frac{1}{(1-\nu_{12}\nu_{21})} \begin{bmatrix} E_{11} & \nu_{21}E_{11} \\ \nu_{21}E_{11} & E_{22} \end{bmatrix} \begin{bmatrix} \epsilon_1 \\ \epsilon_2 \end{bmatrix}$$

evaluated at $t + 1/2$

The shear stress-strain relation is defined as:

$$\gamma_{12} = \frac{1}{G_{12}}\sigma_{12} + 3\alpha\bar{\sigma}_{12}\sigma_{12} \tag{5.2}$$

Where α is an experimentally derived value. Setting α to zero reduces the elastic behaviour in relation to orthotropic Hooke's Law. For the prediction of failure, MSC/Dytran has a variety of models available, the card Mat8A is built on a set of stress-based failure criteria for the fiber and matrix failure under tensile, compressive and/or in-plane shear loading, while these failure modes can be accounted for in shell theory where plane stress condition is assumed and the failure mechanisms of delamination response associated with a splaying mode of failure and debonding were not considered. For this reason, additional input data regarding to lamina strength in its principal material directions is required, while the failure criteria mentioned below are formulated as ratios of applied stress to lamina strength, with multiple terms accounting for lamina in-plane stress interactions. To develop a numerical method to simulate the tensile behaviour, the FML laminates were modelled by a nonlinear layered structural shell element. This element has six degrees of freedom at each node: transitions in the nodal X, Y , Z directions and rotations about the nodal X, Y,Z axes. The glass fibre/epoxy layers were modelled with homogenized linear elastic orthotropic materials, and the elasto-plastic characteristic of aluminium layers were modelled with bilinear isotropic hardening materials behaviour using the von Mises yield criterion. In general, phenomenological strength criteria such as maximum stress and Chang-Chang criteria are used to detect the failure status of composite laminates. Due to the complexity of failure mechanisms in the FML material, it is difficult to define an applicable failure criterion. However, it is expected that the uniaxial static tensile failure of FML material is dominated by properties of glass fibre/epoxy composite layers, and the laminate fails just after the fibre breakage. So, the maximum strain failure criterion

was used to predict the failure load in this study, and fracture is expected to occur when the strain in glass/epoxy layers reach the ultimate failure strain because aluminium has a much higher ductility than the fibre/epoxy composite layer. The basis of the model is the modification made in (43), to the well known Chang and Chang composite damage model. More specifically, the fiber breakage the failure is assumed when the following condition is true:

$$\left(\frac{\sigma_{11}}{X_T}\right)^2 + T \geq 1 \qquad (\sigma_{11} > 0) \tag{5.3}$$

It must be noted that T is a weighting factor for the ratio of the shear stress to shear strength taking values in the range between 0.0 and 1.0. When failure occurs, the material constants E1, E2 , ν_{12}, G12 are set to zero in the corresponding unidirectional layer of the composite shell element.

$$T = \left(\frac{\sigma_{12}}{S}\right)^2 \frac{1 + \frac{3}{2}\alpha G_{12}\sigma^2}{1 + \frac{3}{2}\alpha G_{12}S^2} \tag{5.4}$$

In the case of compressive fiber mode, failure is assumed to be:

$$\left(\frac{\sigma_{11}}{X_C}\right)^2 + T \geq 1 \qquad (\sigma_{11} > 0) \tag{5.5}$$

Similar to the previous case, when failure occurs, material constants E1, E2, ν_{12}, G12 are set to zero in the corresponding unidirectional layer of the composite shell. Finally, regarding the matrix failure, the matrix cracking is assumed:

$$\left(\frac{\sigma_{22}}{X_C}\right)^2 + T \geq 1 \qquad (\sigma_{11} > 0) \tag{5.6}$$

while the matrix compressione is defined by:

$$\left(\frac{\sigma_{22}}{2S}\right)^2 + \left[\left(\frac{Y_C}{2S}\right)^2 - 1\right]\frac{\sigma_{22}}{Y_C} + T \geq 1 \qquad (\sigma_{22} > 0) \tag{5.7}$$

The property degradation rules describe how stress increments are related to strain increments in the various directions after failure in a particular mode has occurred, for example, in matrix compression failure, the material constants E2 (lateral Young's modulus), and ν_{12} (Poisson's ratio) are set to zero. Finally, the model describes how the stresses are relaxed to zero after failure has occurred. The relaxation can start either when a particular mode has failed or when all material properties (E1, E2, ν_{12}, G12) are degraded to zero according to the property degradation rule. The relaxation always occurs in time, either in problem time units by a propagation velocity, or simply by time steps. This model is referred to as the post-failure degradation rule. The basic material properties required for this model are given in table (5.2).

Young modulus $E\,[GPa]$	**Yield Stress** $\sigma_y\,[MPa]$	**Strength** $\sigma_r\,[MPa]$	**Deformation at failure** $\epsilon_r\,[mm]$
30.7	310.3	631.4	0.064

Table 5.2: Material Properties of the FML

5.3 Sandwich Honeycomb Material

This section refers to the material constitutive models used to simulate the material behaviours of the distinct parts of the leading edge. The core of the configuration is a hexweb aluminium flexcore developed by Hexcel; the cells have been manufactured from aluminium alloy 5052 with core height of 6.35mm, core cell size of 9.53mm and core cell wall thickness of 0.145mm. For the honeycomb core material behaviour, an "Orthotropic Crushable Material Model" was used, where the properties and the corresponding experimental stress strain curve under edgewise compression are given respectively in table

(5.3) and figure (5.1). The input required for the material consists of two parts: data for the fully compacted state and data for the crushing behaviour. For the fully compacted material, density, elastic modulus, Poisson's ratio and yield stress for the fully compacted material, and the relative volume at which the material is fully compacted were. During crushing, the elastic modulus varies from their initial values to the fully compacted values. The stress-strain curve of such a material is shown schematically in figure (5.1). The stress strain curve has three distinct regions: the first part of curve is

Young modulus for material fully compacted [GPa]	**Max Shear Direction L** $\tau_L[MPa]$	**Max Shear Direction W** $\tau_w[MPa]$	**G13** [MPa]	**G23** [MPa]
0.9	0.8	1	90	220

Table 5.3: Core Material Properties

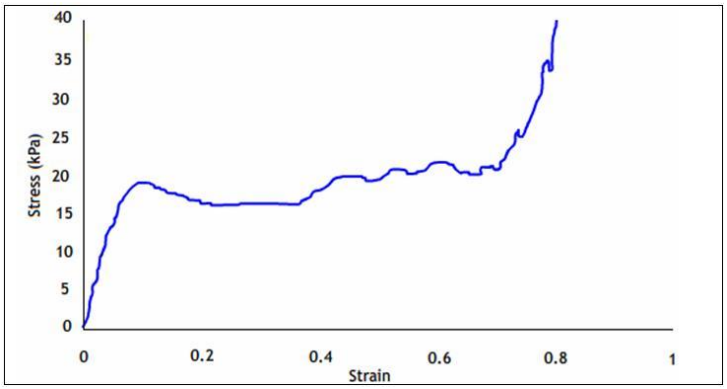

Figure 5.1: Experimental compression stress strain curve

characterized from predominant contribution to the elastic strain comes from the vertical compression. In the model FE has been considered a table to define the stress-strain with the variability of cell volume under compressure.

About the elastic region it is characterized by the effective Young modulus of the material, considering E* = 2.3 ES (t/c)3 (44), with Es=70GPa, t is the core cell wall thickness equal to 0.145mm and c is the core cell size equal to 9.53mm, the average modulus E* is 567MPa. The second part of graph shows the aluminium honeycomb will start to plastically deform if the stress in the faces anywhere exceeds the flow stress, σ_Y, of the aluminium cell wall. The yielding behaviour started when the maximum stress in each face reaches the flow stress, σ_Y, of the material making up the cell walls, which is given by:

$$\sigma = \frac{2}{3}\left(\frac{t}{l}\right)^2 \cdot \sigma_Y \tag{5.8}$$

Considering that t is thickness of an individual sheet and it is equal to 0.145 mm, l is the length of each of the cell faces and it is equal to 6.35 mm σ_Y=100 MPa, the yielding behaviour started when the stress is 34.7 kPa. At last the densification strain at which the cells deform uniformly, ϵ_D, is given by:

$$\epsilon_D = ln\left(\frac{l}{l + 2lsin\theta}\right) = ln\left(\frac{1}{1 + 2sin\theta}\right) \tag{5.9}$$

Then the stresses rapidly increase with further deformation due to the fact that the cell walls are forced into contact with each other. When the material is fully compacted, the behaviour is assumed to be elastoplastic with isotropic plasticity. The load tables define the magnitude of the average stress in a given direction as the material's relative volume changes. The densification strain about the hexweb aluminium flexcore developed by Hexcel is considered equal to 0.7.

5.4 Fasteners Element

The fasteners used during the experimental test were in titanium material and were modelled with one dimensional element and with an isotropic elastic plastic model. The non-linear behaviour and the failure criterion, may be expressed by:

$$\left[\frac{N(\alpha)}{N_u}\right] + \left[\frac{T(\alpha)}{T_u}\right] \leq 1 \tag{5.10}$$

where $N(\alpha)$, N_u are respectively the current and the ultimate tensile components and $T(\alpha)$, T_u are respectively the current and the ultimate shear components. The global load, F, may be divided into two components as a function of the angular position:

$$N(\alpha) = Fcos(\alpha) \text{ and } \; T(\alpha) = sin(\alpha) \tag{5.11}$$

Variations of this angular position leads to different load configuratios, moreover for $\alpha = 0$ and $\alpha = 90$, pure tensile and pure shear loads are obtained. The fitting chosen the study is characterized by parameters, $\{N_u, T_u, a, b\} = \{4.45N, 2.54N, 2.8, 1.8\}$, (45).

The experimental tests were performed at $\alpha = 0$, and the aim of the the dynamic tests related was to characterization of the joints, with different values of speed ($1ms^{-1}$, $5m/s^{-1}$ and $18m/s^{-1}$) to define the failure criterion and the non-linear behaviour,

The yield (0.2%) and Ultimate Tensile Stress of aerospace alloys such as 2024-T351 are not considered to be overly sensitive to strain rate. However, more significant is the influence of strain rate on the fracture strain. Although, not entirely conclusive, static and dynamic test performed on the rivets, in the last section, indicated an increase in fracture strain with respect to strain rate, experiemntal tests confirms this trend, giving a true failure strain value of over 20% for a strain rate of $500s^{-1}$. Strain rates of order

$100s^{-1}$ are typical of the averaged global strain rates that a fuselage structure might experience during a crash. But, observation of the failure modes in the test joints showed highly localised regions of deformation where the strain rate is likely to be much higher, and consequently the failure strain too. Moreover, for impact analysis (bird-strike, tyre or hard debris impact) the strain rate can reach an order of magnitude of $1000s^{-1}$ or more. The fracture is modelled with the Cowper-Symonds:

$$\frac{\sigma_n}{\sigma_y} = 1 + (\frac{\dot{\epsilon}}{D})^{\frac{1}{P}} \tag{5.12}$$

where σn is the dynamic stress, σy is the static yield stress, and ϵ is the equivalent strain rate. D and p are constant in Cowper-Symonds rate enhancement formula.

Chapter 6

Bird-Strike Simulation

6.1 Test Procedure

In this section are reported the experimental tests about the impact on the leading edge bay. Preliminary validation of the bird-strike test methodology was achieved through a series of tests and simulations on a simplified but representative structure, developed and manufactured specifically for this purpose by Alenia. Those tests have been useful to identify the best configuration capable to optimize the weight and performance and have given the opportunity to correlate the results with numerical results, which have been extended to the experimental fullscale test on the tailcone. The bay of the leading edge of the representative structure is shown in figure (6.1). Typical dimensions of the bay is 640 mm x 330 mm and thickness of the rib is 2 mm.

A number of different impact scenarios have been considerd in order to identify the worst case scenario and to get insight into the behaviour of the component The main points subjected to variation have been: thickness and materials, table (6.1) reports the different configurations studied during this first massive campaign of test, it can be noted the configurations are different

Figure 6.1: The leading edge's bay

for the application of a different outer skin and of a different thickness of the ply, the core and inner ply are the same for each configuration.

Test	**Outboard**	**Core**	**Inboard**
1	AL 2024 (1.4mm)	honeycomb (6.32mm)	AL 2024 (0.4mm)
2	AL 2024 (1mm)	honeycomb (6.32mm)	AL 2024 (0.4mm)
3	FML 3/2 (1.4mm)	honeycomb (6.32mm)	AL 2024 (0.4mm)
4	FML 2/1 (1.05mm)	honeycomb (6.32mm)	AL 2024 (0.4mm)
5	FML 2/1 (0.85mm)	honeycomb (6.32mm)	AL 2024 (0.4mm)

Table 6.1: The configurations considered during the experimental test

The figure (6.2) presents the lay-up of the leading edge configuration with an outboard ply in FML, the honeycomb is the core of the composite configuration and it is a flexcore aluminium with a cell height of 6.35 mm, the inner ply is made of aluminium alloy of 2024 with a thickness of 0.4 mm.

The figure (6.3) presents the composite lay-up of the leading edge configuration with an outboard ply in aluminium, the configuration is completed with the core and inner ply, which are the same of the last lay-up.

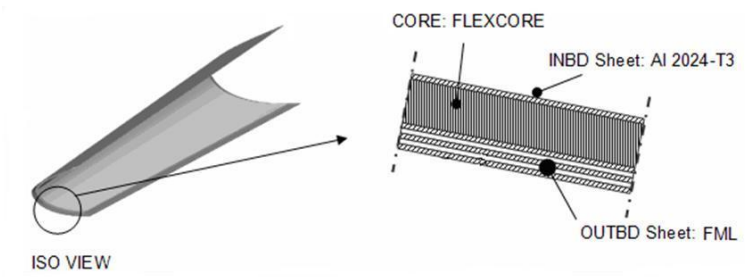

Figure 6.2: Test configuration FML specimen

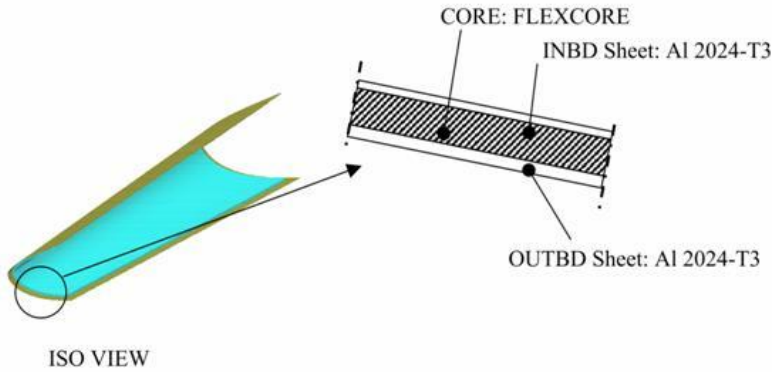

Figure 6.3: Test lay-up aluminium

6.2 Experimental Setup

Tests were conducted using an air pressure gun, with a barrel length of 12m, able to shoot dummy birds at speed up to 140m/s. The arrangement of the apparatus is shown in figure (6.4), where is poossible to distinguish the leading edge bay position.

The projectile was held inside a sabot packed with expanded polystyrene in such a way that no position changes or damage was experienced under the acceleration when fired. The functions of the sabot are also to hold and support the projectile, to seal the pressure chamber from the gas gun barrel

Figure 6.4: Air pressure gun with one single bay leading edge as target

and to guide the projectile during firing. It has to be as light as possible since it constitutes an unwanted dead mass and it must separate easily from the actual projectile just prior to impact without any planned projectile velocity or trajectory. Final tolerances were important because the projectile should go through the barrel without any friction which would cause a slowdown in the impact speed.

The whole assembly was located at a distance of three meters from the mouth of a gun. The operating procedure consisted in inserting the sabot with the projectile in the breech block, applying a pressure above the predetermined test pressure to the prongs and inserting the whole assembly between the flanged ends of gun barrel and pressure chamber. The sliding flange in the pressure chamber was then pressed against the breech block with a hand operated hydraulic pump. The pressure in the chamber was finally raised to the desired value. To fire, the prongs were vented to atmospheric pressure. The pressure in the chamber caused the clamps to retract thus releasing the sabot. The triggering system together with the tight tolerances of the sabot ensured an extremely consistent performance of the gun. The velocity of the projectile was measured by two photocell mounted between the muzzle and the sabot separator. Two high-speed cameras up

to 10,000 fps were used to visualize the impact sequence, one recorded the impact in the front view and the second one recorded the lateral view.

The support frame was suspended by means of six load cells of 10KN, figure (6.5), which measured loads transmitted to the foundations in three

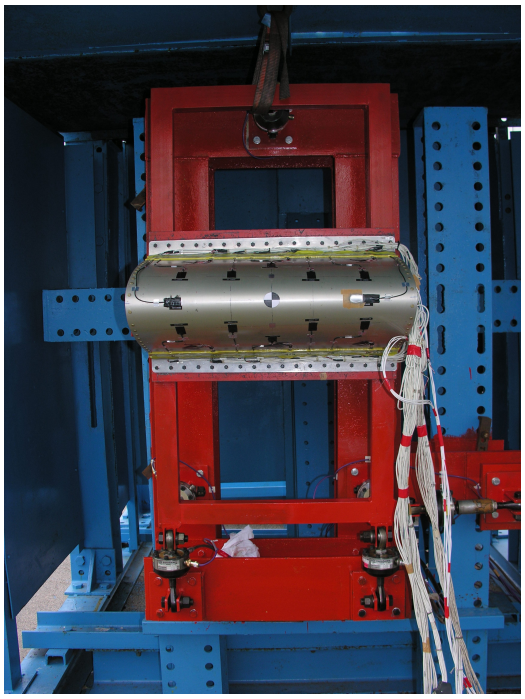

Figure 6.5: Experimental Setup

coordinate directions. The data acquisition system was a typical high speed, with a sampling frequency of 100kHz, this system were linked to the load cells attached to the loading frame and to other sensors (accelerometers, strain gauges) located around test article. During the test phase, unfortunately the strain gauges and accelerometers data could not be retrieved due to the detachment or saturation during the event. However, data gathered from the load cell were available. The projectile impacted just inside the leading edge at mid height just onto the target.

6.3 Finite Element Analysis

The Finite Element code MSC/Dytran (19) was used to predict the effects of bird-strike on the leading edge. MSC/Dytran is a general-purpose explicit finite-element code able to analyse transient dynamic problems with geometric and material nonlinearity.

By analysing the test structures and support, it was decided to model the load frame in some detail since it could introduce its own dynamics into the measurements. In this section the study is dedicated to correlate the FE model with the experimental results, the figure (6.6) shows the finite

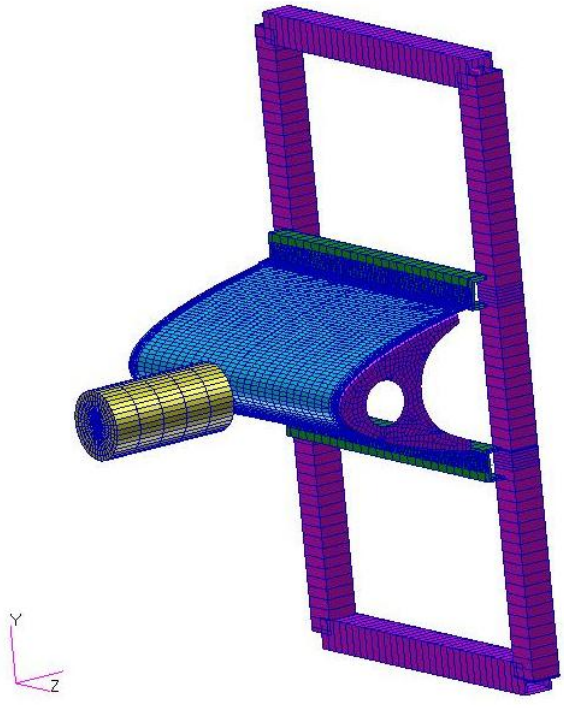

Figure 6.6: Leading Edge FE model

element model of the leading edge structure and the lagrangian bird model.

The model contains the bird, one leading edge skin, two ribs, a rigid back plate and the load frame, and the leading edge was also modelled in details i.e. skin and core.

The load frame was divided in the interface beam and a support beam. The interface beam was used to connect the leading edge structure to the load frame, and they were linked to the support frame using a tied node to surface contact interface. Both the interface beams and the support frame were given the properties of steel and they are assumed to remain elastic throughout the analysis. The support frame was attached to ground with six spring elements, the free ends of the spring elements were fixed in all six degrees of freedom to simulate the rigid supports in the experiment. The skin was riveted to the two rib flanges. The rigid back plate was a beam located back the model to protect in case of perforation or excessive deformation of leading edge structure during the tests.

For this test the planned impact angle was 90 degree with an impact speed equal to 129 m/s and the bird mass was 3.68kg. The outboard skin contained 4.544 shell elements with a relatively fine uniform mesh, the sandwich honeycomb core was modelled with eight-node brick, this ply contained 12.240 elements. The fasteners jointed were modelled by one dimensional element and they jointed the stinger at interface beam and then we were used the same fittings to joint the ribs to skin.

The truss are modelled with one-dimensional element, and it was divided in the interface beam and a support beam figure (6.7-d). The interface beam was used to connect the leading edge structure to the load frame, and they were linked to the support frame using a tied node to surface contact interface. The FE model consists of two brackets or horizontal beams, which were linked to the truss and supported the corner of the leading edge, both the interface beams and the support frame were given the properties of steel and they are assumed to remain elastic throughout the analysis. The total

number related to fitting and whole truss were 387 one dimensional elements. The two ribs were contained 1422 shell elements, (6.7-b), and the horizontal beams were linked to the outboard skin and interface beam with the fittings, discretised using four nodes shell elements (figure (6.7-a). The bird element were modelled with eight-node brick, this one contained 2938 elements. it was shaped as a cylinder of 268mm long and a diameter of recreated 134mm diameter (6.7-c). The total number of specimen's finite elements were 37.407.

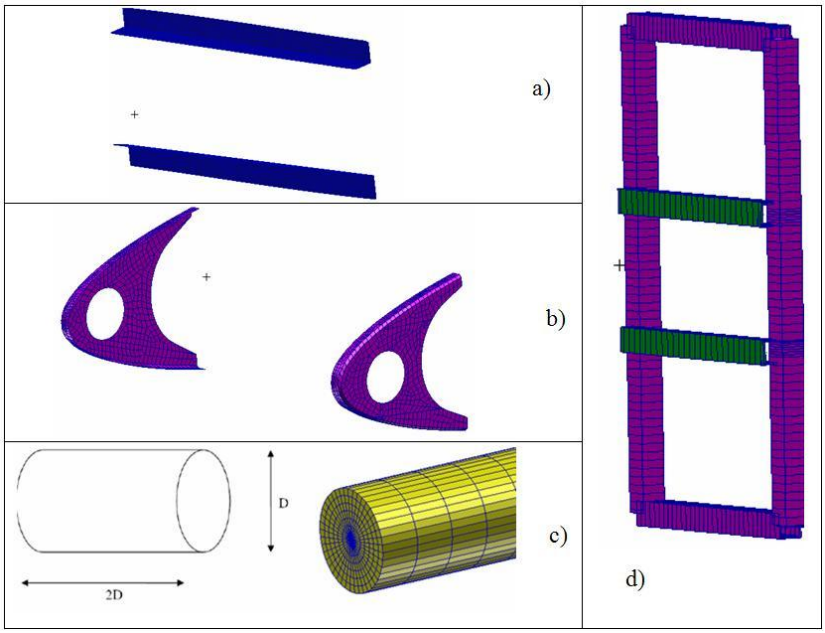

Figure 6.7: FE model: brackets (a), ribs (b), bird (c) and load frame (d)

6.4 Numerical and Experimental Correlation

6.4.1 Aluminium configuration

The leading edge with an outer ply in aluminium alloy material consists of two different configurations, the first one has a ply with thickness of 1 mm, the second one has a sheet of 1.4 mm. Only the main results of the leading edge with 1mm skin thickness (configuration 1) are reported, while a detailed analysis of the configuration with a thickness of 1.4mm (configuration 2) is reported. The deformed shape of configuration 1 is shown in figure (6.8).

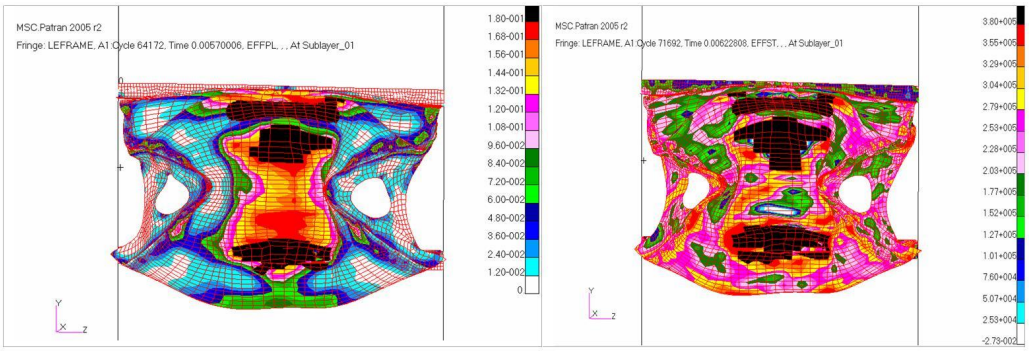

Figure 6.8: Configuration 1 - Strain (left) - Von Mises Stress (right) (KPa)

The figure shows the strain and stress plot on the configuration. The failure occurs when the equivalent plastic strain exceeds the 18%. Then it shows the Von Mises stress on the bidimensional element (outboard and inboard skin) about configuration number 1 and by examining it, it is possible to distinguish the initiation of damage in the buckled region highlighted by the fact that the maximum stress on the inboard ply were larger than the allowable stress, 385KPa. This showed us that the configuration 1 was not able to withstand the bird-strike. The experimental results, shown in figure (6.9) clearly confirmed our numerical prediction, the figure showed the

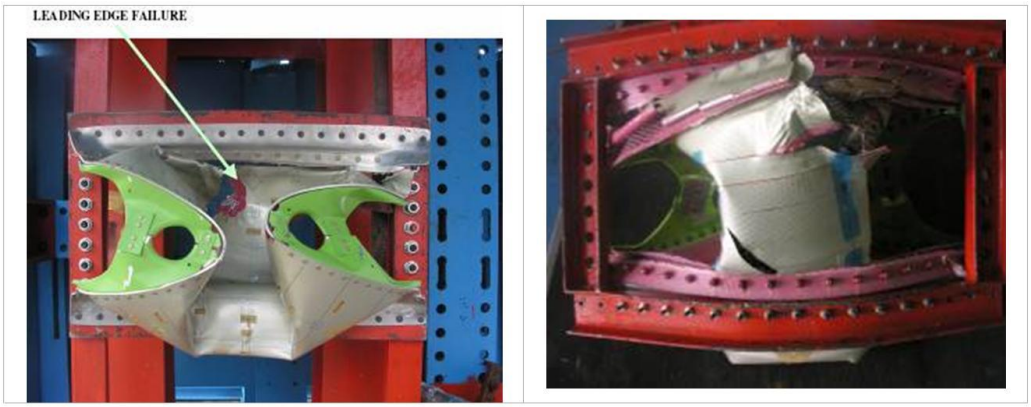

Figure 6.9: Deformed shape of the front and rear view configuration 1

first configuration after the impact; therefore a new design of the tailplane leading edge was needed with minimum changes in terms of manufacturing process and easy-of-implementation. It was decided to change the outboard skin thickness from 1 to 1.4mm. A new finite element model was built and impact transient analysis was performed about the second configuration. Figure (6.10) gives a comparison of the measured and predicted deflection of configuration 2. It can be seen that the global phenomenon is well reproduced. The finite element simulation did not predict any penetration of the bird as required by the certification authority. The figure (6.11) shows a comparison of the evolution of the deformation in time between the FE simulation and the test. Examining the progressive collapse and the terminal views of the crushed sandwich specimen, the deformation modes and failure characteristics observed from macroscopic point of view were satisfactory simulated by the developed finite element model. The cracks of the compressed sandwich and the subsequent laminate splitting are formed as a result of the brittle fracture failure mode of the laminates and are formed at the areas of high stress concentration. The results of the finite element analysis agree well with the findings of the experimental works. Unfortu-

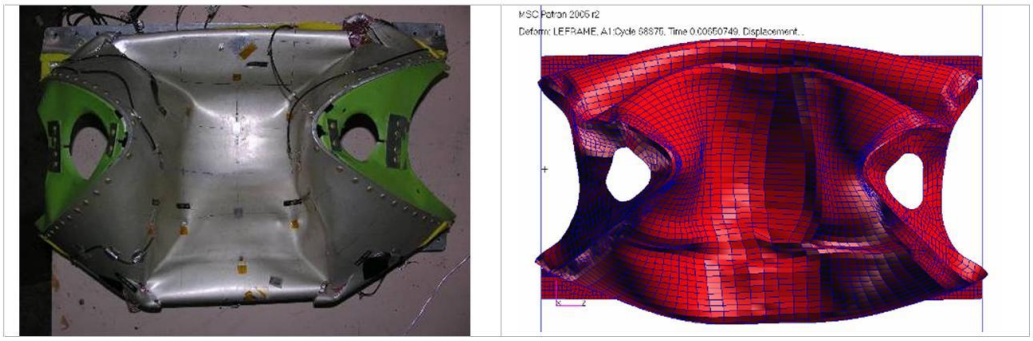

Figure 6.10: Deformed Shape of configuration 2 a) Experimental b) FE

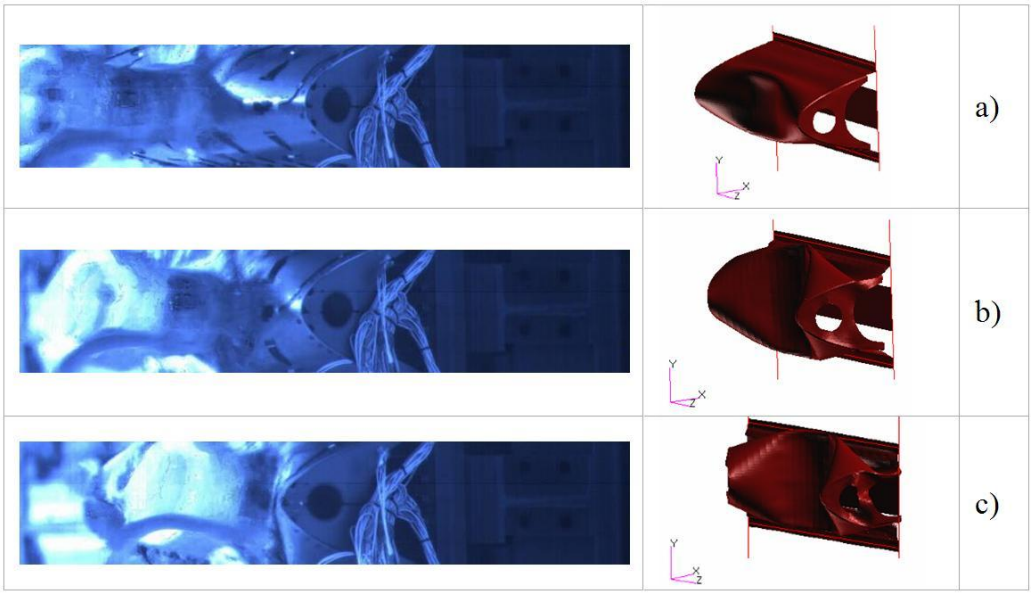

Figure 6.11: Comparison of impact sequence between experimental and numerical simulation at (a) t = 1ms; (b) t = 2ms; (c) t = 3ms

nately the strain gauges and accelerometers data could not be retrieved due to the detachment or saturation during the event. However, it was possible to correlate some parameters. Figure (6.12) shows the displacement shape

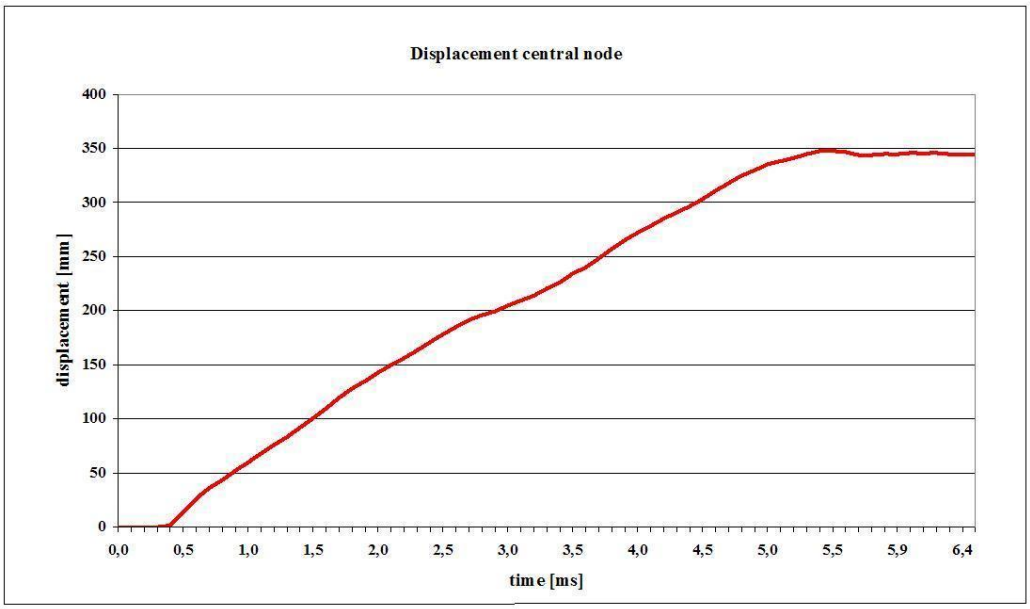

Figure 6.12: Time history of central node on the leading edge

of the central node (impact location). It can be seen that the time history presents a significant increase in model deformation with a maximum displacement of the target point equal to 350mm, and the residual displacement of 340mm. This value of displacement is not accepted because of the spar position. This test was performed fixing behind the configuration a large beam, which has a double function, the first solution is to define the position of the spar, the second one is to avoid that the bird could perforate the leading edge and create a catastrophic event, the high speed camera underlined that the defomration of the leading edge is constrained by the beam presence and this lets to think that in absence of the beam, probably the

deformation can be larger. The figure (6.13) shows the von Mises stress on

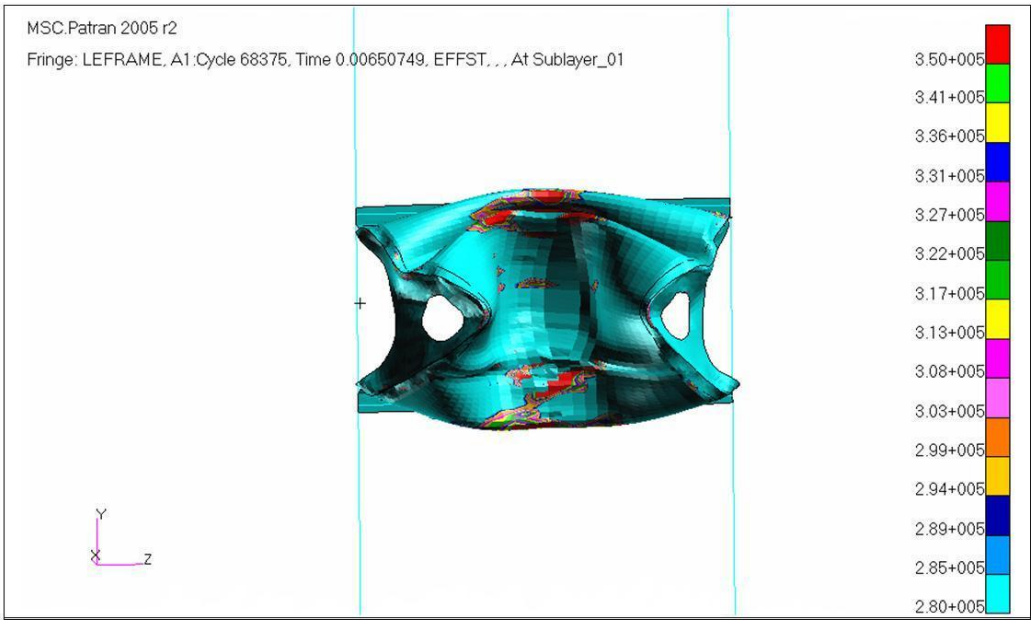

Figure 6.13: Von Mises Stress (KPa) plot on the CQUAD element of the configuration 2

the bidimensional element (outboard and inboard skin) where is possible to distinguish the zone related to the progressive collapse, characterised by the high curvature after the impact and in proximity to beams. In absence of the sensors it is possible to consider that preliminary numerical simulations were able to predict that the bird did not penetrate the leading edge and the final correlation showed a global behaviour of the bird-strike scenario, confirming the validity of the approach, but now it is possible to correlate the local parameters and for this reason the study remarked several parameters, as for example the comparition of the distance, after the impact, between the edges of ribs. Figure (6.14) shows the final state of the impacted configuration in particular, the distance between the ribs (220mm). The time history

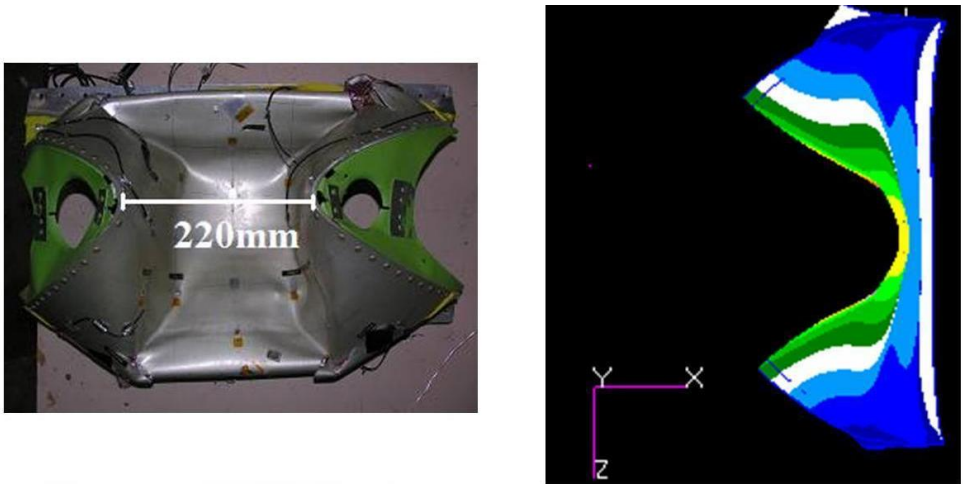

Figure 6.14: Edge rib distance after the impact

of figure (6.15) shows the displacements of each edge rib, this confirms the validity of the approach. In particular, the model was accurate to predict the final rib distance with an error of 2%, showing that good correlation was achieved. Figure (6.16) presents the difference between the honeycomb behaviour during the impact when the outboard skin has a thickness of 1.4mm and the case of skin outboard with a thickness of 1mm; this figure shows the honeycomb of the configuration with an outboard of 1.4mm absorbs a higher energy level during the impact than the case of configuration with an outboard 1mm. Figure (6.17) shows the time history recorded from load cells along impact direction, and FT03 represents the top load cell, whereas FT01 and FT02 represent the bottom load cells. Very poor correlation was achieved in terms of the curve behaviour between the numerical and experimental data. However, analysing the peaks recorded from three cells it was noted that they were different in time (even if the loads cells were located symmetrically with respect to the impact location) due to the rotation of the impactor. The bird hit the target, and after this first contact the bird rotates

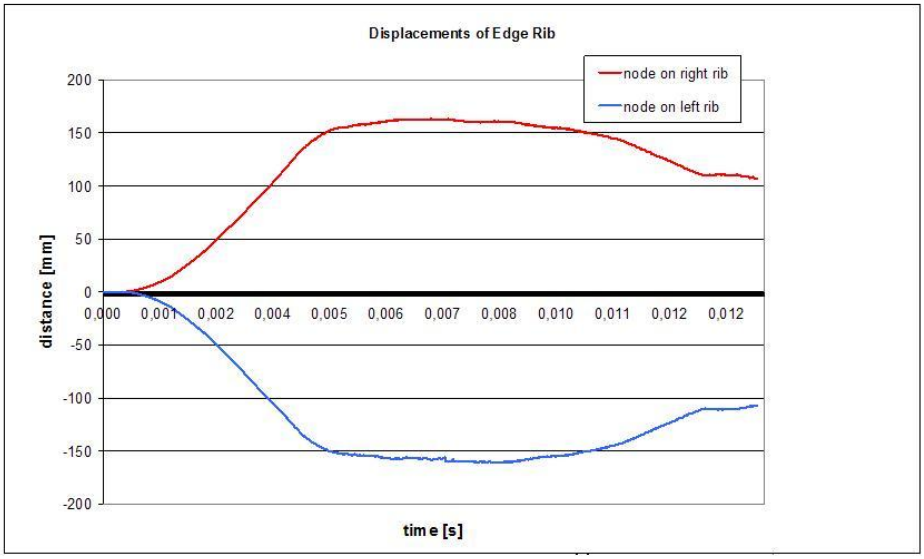

Figure 6.15: Edge rib's uz displacement during the impact

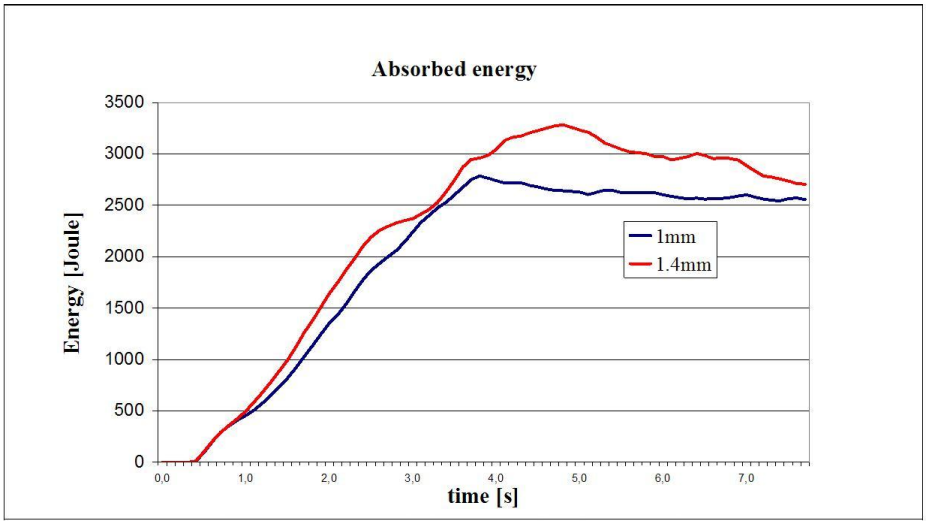

Figure 6.16: Estimated Impact energy absorbed by the honeycomb for the two configuration analysed

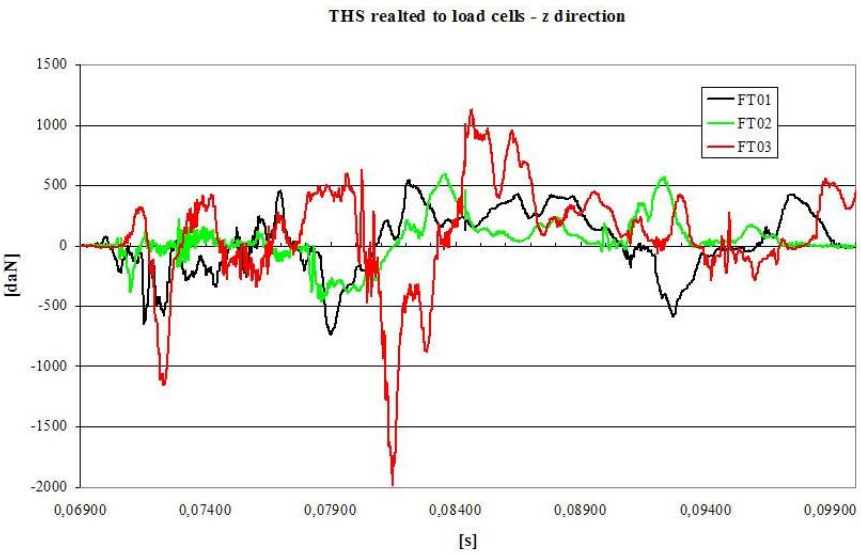

Figure 6.17: Time history recorded from load cells along impact direction

downward causing a force peak on the bottom load cell. This asymmetrical impact created a different shape of the time histories and it was therefore difficult to correlate it with the numerical time histories. Nevertheless, a correlation was attempted to correlate the peaks related to the three load cells. Table (6.2) shows the comparison between maximum peaks recorded

Load cells	**Exp value (daN)**	**Num value (daN)**	**error (%)**
FT01	-522	-544	3.9
FT02	-858	-893	4.2
FT03	-1,980	-2,053	3.6

Table 6.2: The configuration considered during the experimental test

from load cells and the FE results along impact direction. It is possible note that also in this case an error lower than 5% was obtained.

The configuration 2 (with outer ply of 1.4 mm) has showed a good performance at bird-strike but the deformation is strng, in particular, the model was accurate to predict the final deformed shape of the leading edge and the absence of foreign object penetration, showing that the designed leading edge made a composite material was able to protect the inner LE structure from damaging and to satisfy certification requirements. The numerical-experimental correlations show that the developed finite element models were able to well represent the different failure mechanisms characterizing the structural responses.

6.4.2 FML Configuration

In this work is reported the analysis related to the leading edge configurations with outer ply in fiber metal laminate material. Three different configurations were considered, the differences consist of the thickness of outer ply. The first configuration presented ply in FML 3/2-0.3 mm with an amount thickness of 1.4 mm, the second configuration has FML 2/1-0.4 mm with an amount thickness of 1.05 mm, and at least the third configuration presented ply in FML 3/2-0.3 mm with an amount thickness of 0.85 mm.

In this work the bird has been idealized as a cylindrical bullet of homogenous material. The numerical model of the bird-geometry (shape and dimensions) and material (constitutive law and equation of state) - is central in a bird-strike analysis when using explicit FE codes. The MSC/Dytran is the explicit code used during the crash simulation and the lagrangian approach was considered to model the bird impact phenomenon. In this report the bird was modelled as a projectile with the shape of a cylinder and the lagrangian approach has been adopted. The Lagrangian method consists of realizing a mesh associated to particles in the material under examination; therefore, each node of the mesh follows an individual particle in motion. This approach describes the motion because fixed the initial position it is

possible to restore a kinetic history about any point. The weight of bird used in the impact testing was 3.86kg, the density was $\rho = 950kg/m3$, and it was shaped as a cylinder of 268mm long and a diameter of recreated 134mm diameter, it has been solved with the MSC/Dytran explicit finite element code. The finite element model of the cylinder have been developed using eight-nodes underintegrated solid elements characterized by a progressive refinement towards the impacting end, figure (6.18). Moreover, to avoid

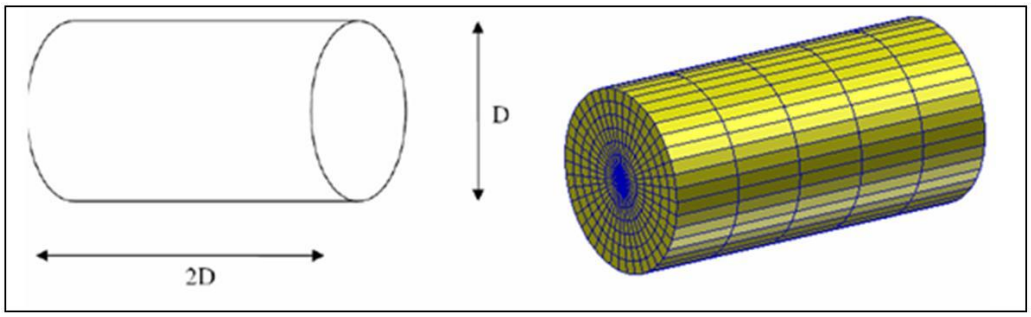

Figure 6.18: FEM for cylindrical body

penetrations, consequent to the distortions of the Lagrangian elements during the analysis, all the faces of the solid elements are involved during the impact with the targeting.

The figure (6.19), shows the finite element model of the leading edge structure, the truss and the lagrangian bird model. The model shown in figure contains the bird, one leading edge skin, two ribs, a rigid back plate and the load frame. The load frame was divided in the interface beam and a support beam. The interface beam was used to connect the leading edge structure to the load frame, and they were linked to the support frame using a tied node to surface contact interface. The one bay component was 640x310mm fixed along the edge on the truss, the interface structure was modelled by 1D elements and its dimension was 1164x630mm.

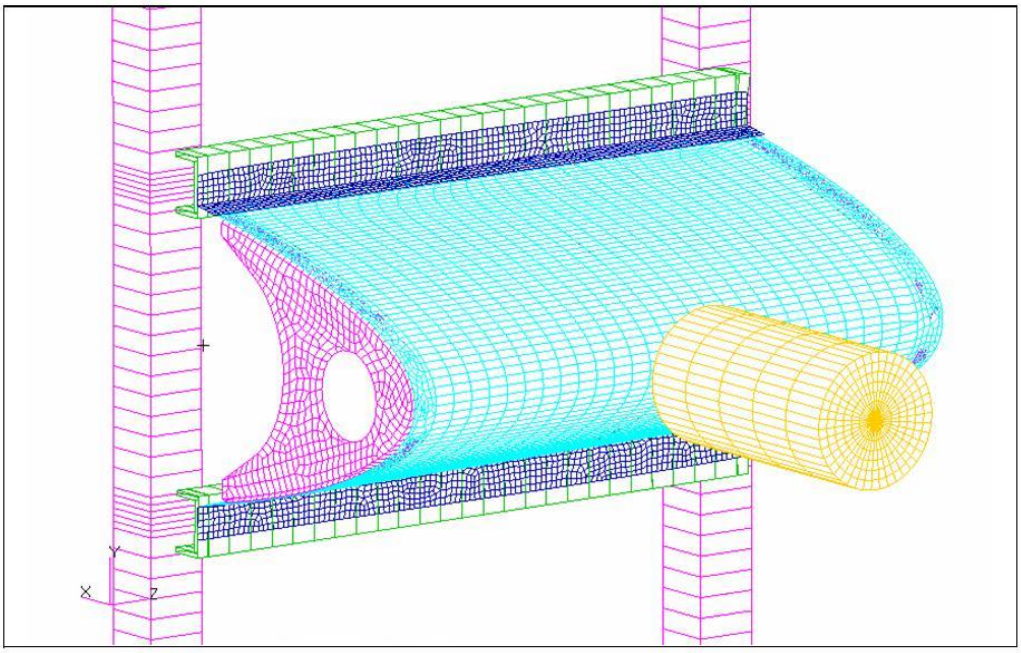

Figure 6.19: Leading edge bay FE model

The impact of the composite leading edge was simulated for velocity to 129m/s. All the configurations have satisfied the strike and no penetration was present but the different configuration have absorbed the kinetic energy due to the bird impact in different way. During the impact, the more critical zones were the one in according to a more variability of curvature, the zone failure are different for the different configurations. The configuration with FML 2/1-0.4 was characterized from a string deformation but this test article absorbed the total impact energy, the penetration was not present and the failure zone regarded the inboard skin. The figure (6.20) shows as the inboard aluminium skin presented a shear along the interface zone among the coupling honeycomb with the inboard ply.

Correlation between the experimental tests and the numerical simulation was attempted considering a normal impact 90 degree. Contact between

Figure 6.20: Failure zone related to the skin inboard

the bird and the structure and possible contact between the ribs and the rigid plate were modelled with lagrangian-lagrangian contact. Self-impacting contact was used to allow all elements of the structure to collide each other. The numerical and experimental correlation have shown good results both in terms of global behaviour of the test article and local evolution of some measurable parameters confirming the validity of the approach and possible guidelines for structural design including the bird impact requirements. The figure (6.21) shows that the developed finite element models were able to describe the zones with higher stress value, the numerical test underlined as the stress distributions exerted on the leading edge by the impacting bird have a peak on the inner skin due to a great curvature by the deformation, the stress value in this zone was higher (1200MPa) than the allowable stress of aluminium ply (380MPa).

The configurations with FML 3/2-0.3 presented a strong deformation but no penetrations were visible, the failure zones regarded a zone larger than the configuration with FML 2/1-0.4,

The figure (6.22) shows the deformation about the configuration with FML 2/1-0.3 and it is visible as the zone subjected to the failure resulted

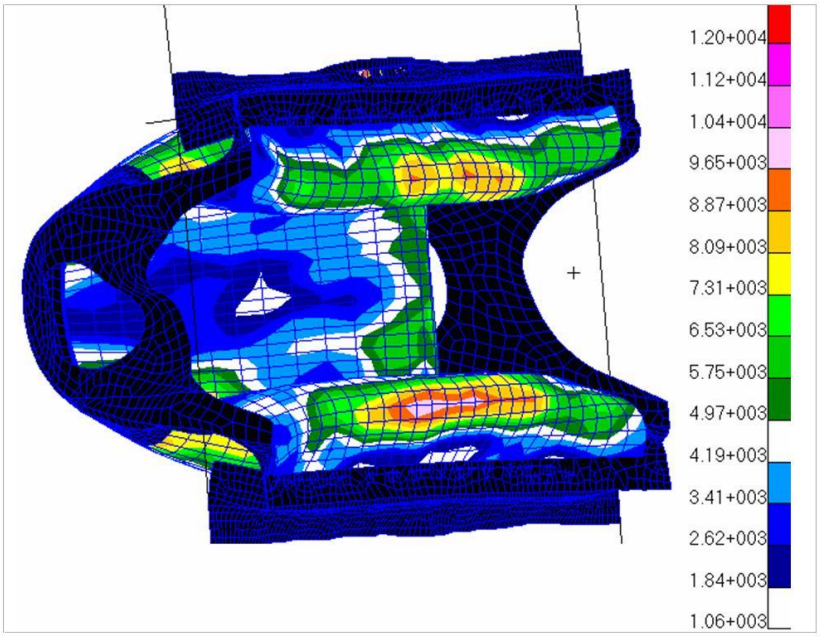

Figure 6.21: Stress on the FE model of the final state of FML 3/2

more extended on the leading edge, this configuration presented, on the outboard skin, the failure zones related to area with major curvature.

The numerical analysis has shown these critical zone on the inboard skin, the edges of FML skin were subjected to strong deformation. The figure (6.23) shows that the developed finite element models were able to describe the zones with higher stress value, the numerical test presented a stress peak on the inner skin, the stress value in this zone was higher (1280MPa) than the allowable stress of FML (631.4MPa).

The figure (6.24) shows the numerical result related to the displacement time history of the central node onto the outboard of the leading edge for all configurations. First information is about the plateau, the deformation was growing in according to the dynamic impact, successively the curve reached a stabilized line. It can be seen that the configuration FML 3/2-0.3

Figure 6.22: Deformation related to the skin inboard (left) and outboard (right)

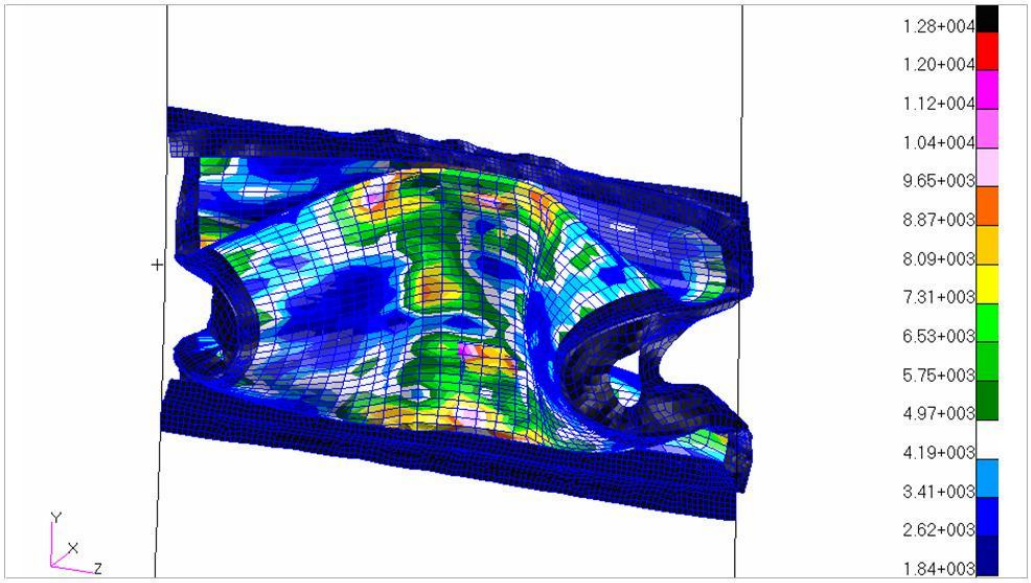

Figure 6.23: Stress on the FE model of the final state of FML 2/1

Figure 6.24: Time history of central node related to configurations

offers the minimum deformation of the central node of leading edge along impact direction, whereas the configuration FML 2/1-0.4 with the aluminium ply of 0.4mm presented a deformation higher the other configuration, the configuration FML 2/1-0.3 with the aluminium ply of 0.3mm presented a failure zone so there is a interrupt along the curve.

The numerical test underlines this critical behaviour about this configuration, the figure (6.25) shows a correlation between the three different configurations, it presents the absorbed energy from the honeycomb for all configurations. It is possible distinguish as the configuration with a thickness of the skin outboard highest absorbed more energy. During the first phase of the impact, the absorbed energy have the same shape, successively, the trend

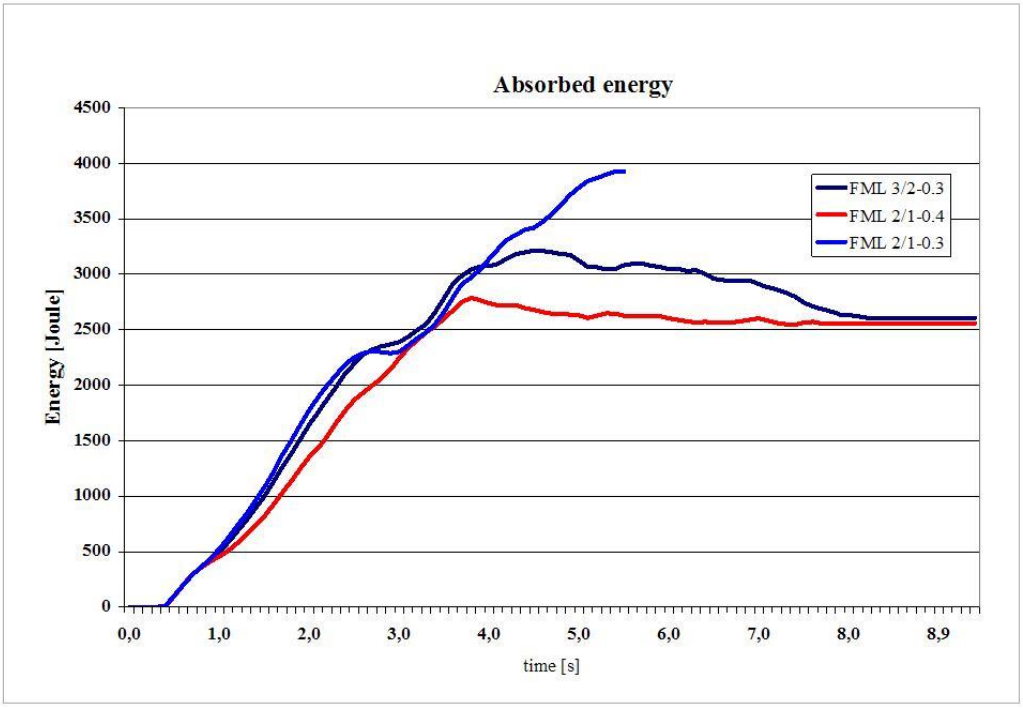

Figure 6.25: Time history of absorbed energy from honeycomb

resulted different due to major deformation of the external skin. It can be seen that the configuration FML 3/2-0.3 offers the maximum energy value absorbed from honeycomb, whereas the configuration FML 2/1-0.4 with the aluminium ply of 0.4mm presented a absorbed energy value lower during the impact dynamic, the configuration FML 2/1-0.3 with the aluminium ply of 0.3mm presented a failure zone so there is a interrupt along the curve.

In general the Fiber Metal laminate shows a higher resistance to cracking than non-clad 2024-T3 in a standard drop weight set-up or gas gun. This impact performance of FML is attributed to a favourable high strain rate strengthening phenomenon which occurs in the glass fibres, combined with their relatively high failure strain. In particular these results underline the

behaviour about the fiber metal laminate, the configuration FML 3/2 shows more advantages related to configuration FML 2/1 relatively to the bird impact. The laminate FML 3/2 presents a major number of aluminium plies related to the FML 2/1, this is favourable to absorb a major aliquot of the energy due to the impact, in this way produce a deformation lower than FML 2/1. Moreover the FML offers 15-30% weight savings over aluminium, due to the a low density. The table (6.3) presents a numerical comparison between the configurations.

Conf.	**Weight [kg]**	**Outboard (th) [mm]**	**Numerical deformation [mm]**
FML 3/2-0.3	1.97	1.4	410mm
FML 2/1-0.4	1.64	1.05	440mm
FML 2/1-0.3	1.53	0.85	460mm

Table 6.3: Comparison between three different configuration

In conclusion, the numerical and experimental correlation phase is the most critical aspects of such highly non-linear behaviour events due to several uncertainties which can affect the test and the model. In general, the model was accurate to predict the final deformed shape of the leading edge and the absence of foreign object penetration, showing that the designed leading edge made with FML material was able to protect the inner LE structure from damaging and to satisfy certification requirements. In particular the FML 3/2 presented a higher resistance to the impact related to the FML 2/1, this performance of FML 3/2 is attributed to a major number of aluminium plies related to the FML 2/1, this is favourable to absorb a major aliquot of the energy due to the impact, in this way produce a deformation lower than FML 2/1.

6.5 ALE Scenario

Now, we proceed to study the ALE Approach for bird-strike events, only the configuration FML 3/2-0.3 is studied applying ALE approach. For the simulation of bird-strike with the Arbitrary-Lagrangian-Eulerian (ALE) is necessary to introduce a surrounding air (control volume), which has to be fine enough to capture the material flow of the bird through the elements properly, see figure (6.26). Figure shows the model with the fluid (birds) inside the mesh.

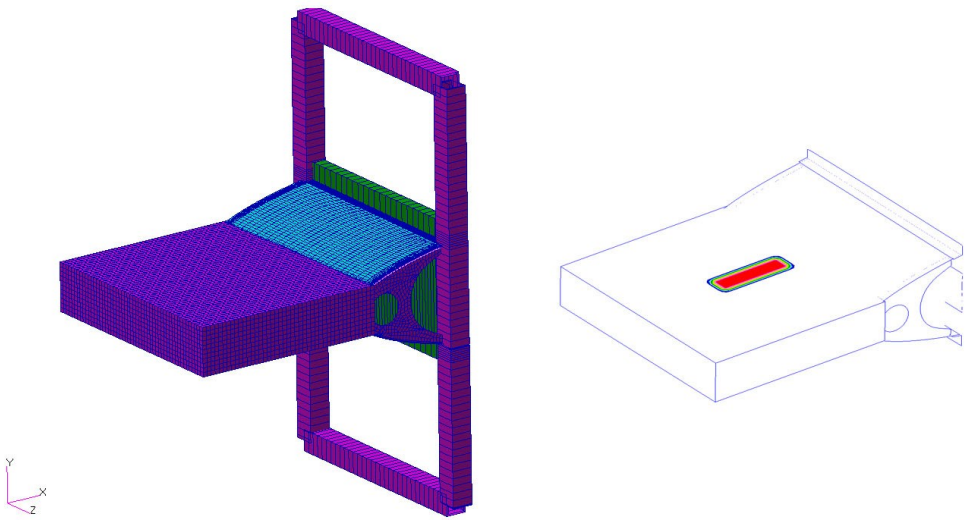

Figure 6.26: ALE finite model (left), control volume (right)

The Leading edge is modelled using shell element (CQUAD) for the outer skin, brick element (CHEXA) for the core and Belytschko-Tsay shell elements (CQUAD4) for the inner ply. The boundary conditions applied at the edges of the skin are defined within a cylindrical coordinate system, where the local X-axis is aligned with the impact speed direction. The cylindrical system is defined by a CORD2C entry.

The bird is modeled in an Eulerian frame of reference, which is built from 5430 CHEXA elements, and it is shown by plotting the material fraction (FMAT), (19), for elements. The birds are modeled as cylinders using the TICEUL entry where the remaining part of the mesh initially is void. The material is allowed to flow out of the Eulerian mesh by defining an outflow boundary condition to all free faces of the mesh by means of a FLOWDEF entry. The structure and the fluid (birds) are allowed to interact at the fluid-structure interface. For bird-strikes, the Arbitrary-Lagrange-Euler interaction is the most efficient FSI (Fluid Strucrture Interaction) to use. To define the FSI, an ALE interface is defined, consisting of a Lagrangian and an Eulerian surface. The structural plate serves as an interface by defining CFACEs on the elements of the plate. The CFACEs then are used to define a Lagrangian SURFACE. The Eulerian mesh coincides with the plate and in the plane of coincidence the faces of the Eulerian mesh are covered with CFACEs that define an Eulerian SURFACE. Both SURFACEs are defined to be used as the ALE interface. To propagate the interface motion into the Eulerian mesh, the Eulerian grid points are defined as ALEGRIDs. The type option on the ALEGRID entry is set to SPECIAL in which case MSC/Dytran will automatically use corrections on the Eulerian grid point motion depending on the boundary condition in which the point is included.

Figure (6.27) shows the bird impact on the leading edge bay. One can

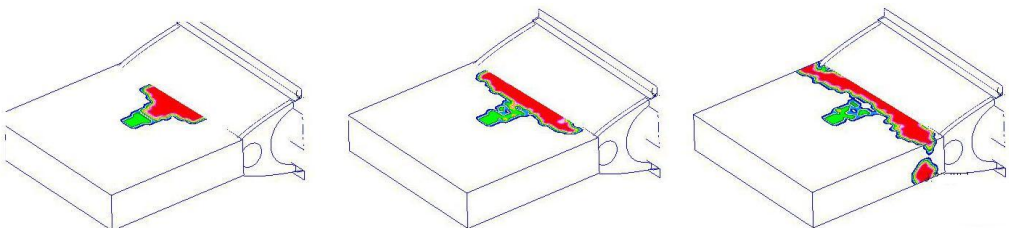

Figure 6.27: Bird-strike, ALE formulation

observe spalling and splitting of the bird leading to fragments of the bird

moving around. The last figure gives the idea of the ALE movement, but it have not offered a good correlation, because of instability of the analysis, infact the deformation is undervalued related to the lagrangian approach. A correlation can be made on the bird deformation after the impact with structure, compared to the Lagrangian bird-strike results the deformation of the leading edge is less localized but more especially in the lower part of the leading edge. It seems that the ALE-formulation is softer and therefore deformation less localized. Rupture of the leading edge is not observed and not failure occurred in the Leading edge spar.

Furthermore the behaviour of the ALE bird model observed during the simulation was close to that of a jelly body and hence somewhat unrealistic. The ALE mesh, at the end of the simulation, was so stretched that doubts on the accuracy of the solution seem reasonable and the simulations has not reached a normal termination. For this analysis, the numerical-experimental correlation was not exactly close. The correlation improved but remained less close than the one of the lagrangian. As a result, the ALE models were abandoned because of the lack of accuracy due to the stretching of the ALE mesh and the displacement is very different by the esperimental result.

6.6 SPH Impact Simulation

The SPH method, implemented in the explicit finite element code LS/Dyna, is ued to model the bird in an impact on the leading edge configuration ribless and with FML material. Detailed comparison with tests are made concerning the deformed shape of the bird and the structure. Above all it is necessary to say that the SPH method is well-suited to simulate problems that present mesh distortions and large displacements, this approach is a lagrangian technique but meshless, and it can be linked to standard fi-

nite element formulations, avoiding some of the material interface problems associated with eulerian code, (46).

In keeping with the current standard practice for bird-strike modelling, the bird model geometry was approximately here as a right circular cylinder with hemispherical end caps as shown in figure (6.28). The density of the

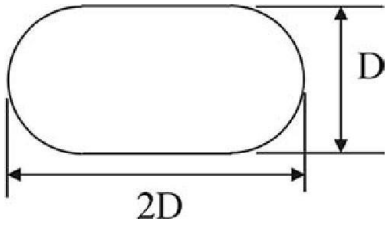

Figure 6.28: Geometry of Bird Model

bird is considered equal to $950kg/m^3$ obtaining an average value equal to about 95% that of water, as suggested by (8). The density model used for bird modelling, which is implemented in the LS/Dyna is the elastic-plastic hydrodynamics model, (47), where the pressure-volume relationship is governed by an equation of state (EOS) and it behaves as an elastic-plastic material at low pressure. The identification of the parameters for the bird model is done using results obtained in the studies reported in (48).

In this section it is possible to present the results obtained with the SPH approach and to do a comparison with results obtained from the Lagrangian approach. The SPH results are data suppied by dr Olivares of National Institute for Aviation Research at Wichita University. Figure (6.29) presents two FE models, considered during te analysis. The Lagrangian approach was studied using the MSC/Dytran code and SPH approach was performed by LS/Dyna code, it is possible to note as the shape of the bird is different, about the Lagrangian model the bird was modelled using a cilinder shape and for the SPH approach the bird was modelled with the hemispherical end caps.

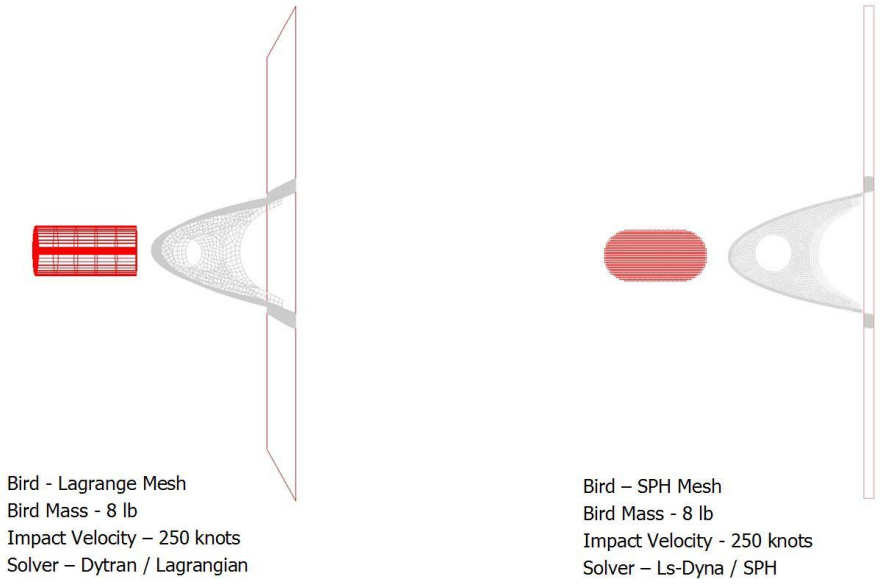

Figure 6.29: Bird Model, Lagrangian and SPH

About the bird shape of Lagrangian approach, the choice is characterized by obtaining a stability of the analysis, because of the large deformations the hemispherical shape did not allowed to terminate the analysis until last time step. This is not applicable to SPH approach and it was preferred to appeal at classic shape to bird modelling and it is possible to consider a cylinder shape.

A first correlation is about the times, the figures (6.30) and (6.31) show sequences of the impact captured during two different approaches, this procedure is considered necessary because to generate these images care was taken to ensure that both numerical studies started just as the bird impacted the leading edge structure.

The figures (6.32) and (6.33) represents the following steps of the simulation and allow to identify the evolution of the impact, the deformation behaviour of the structure according to Lagrangian approach appears to be

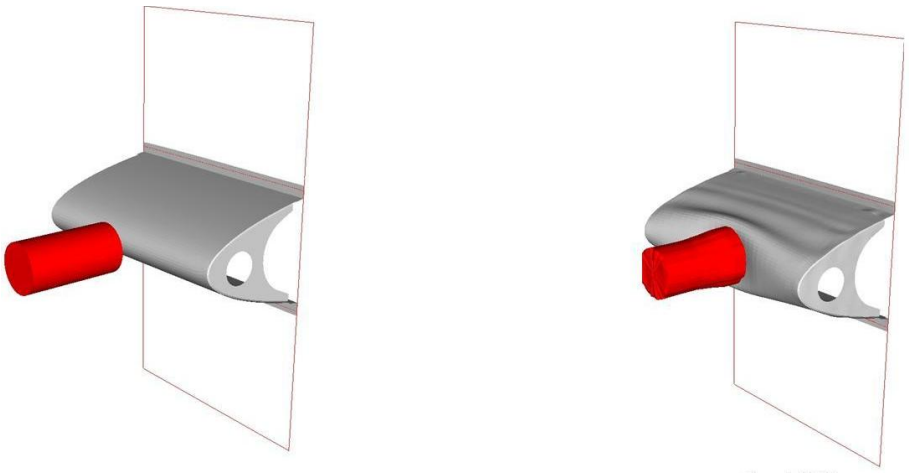

Figure 6.30: Two steps of the impact for Lagrangian modelling at 0 and 1ms

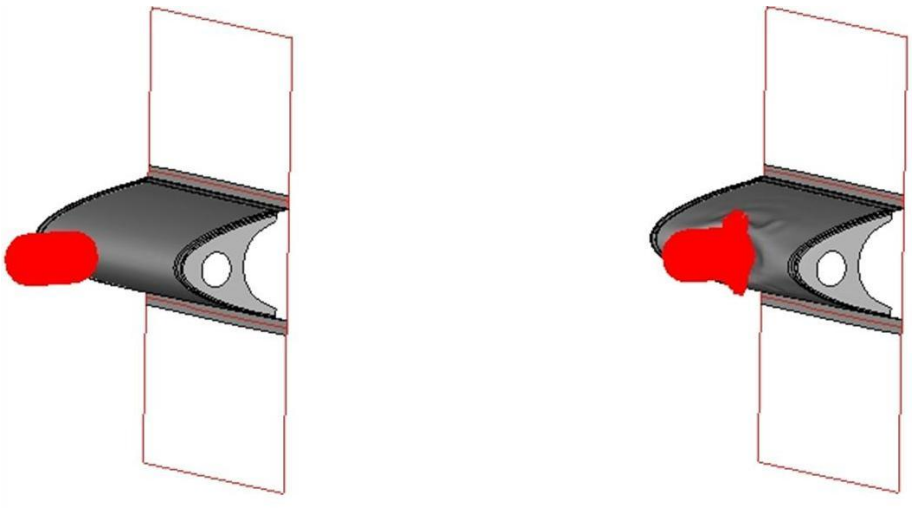

Figure 6.31: Two steps of the impact for SPH modelling at 0 and 1ms

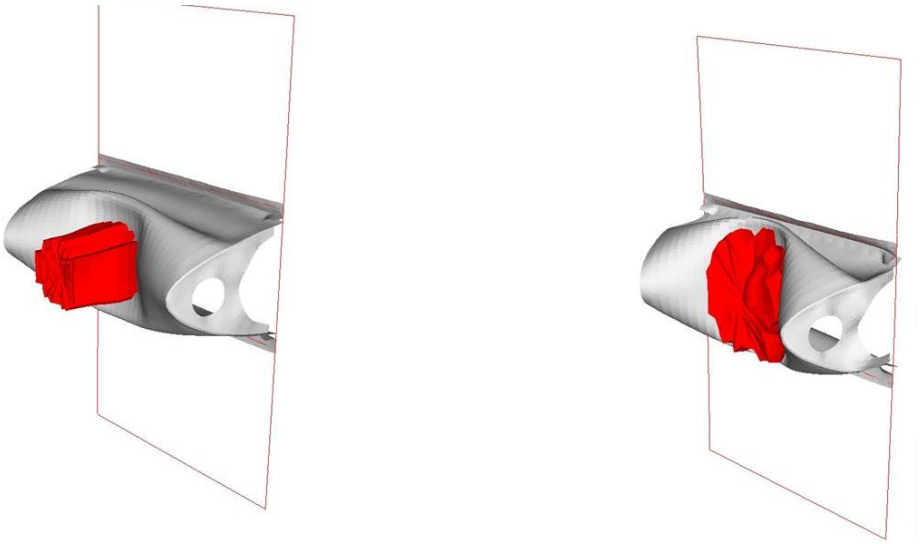

Figure 6.32: Impact for the Lagrangian modelling at 2 and 3.6ms

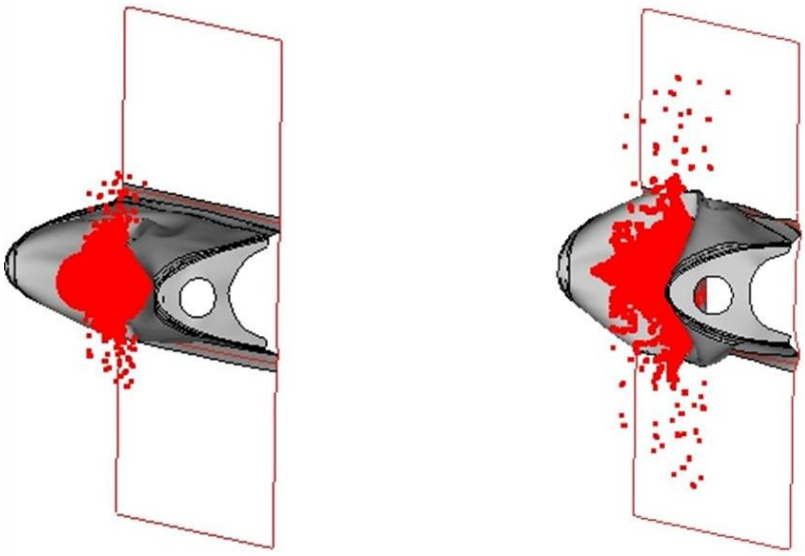

Figure 6.33: Two steps of the impact for the SPH modelling at 2 and 3.6 ms

in excellent agreement with the SPH model. The differences are evident on the deformation behaviour of the bird, infact the Lagrangian bird, (6.32), as soon as impacts the structure starts to deformate and it is evident that FE mesh undergoes large distortions and, therefore, it is straightforward to conclude that the use of the FE model seems feasible only in the early stages of the impact, when the bird is charcaterized by large distortions can cause a decreasing of the time step an unacceprable low value for the calculations to continue because in an explicit finite element analysis, the time step is determined by the smallest element dimension. On the contrary, the SPH model, figure (6.33), the SPH bird flows around the structure and break up into a debris particles and this approach reproduces the bird-strike behaviour, visually, in a way closer to common experience. Both simulations show that the leading ege configuration is able to to withstand the specified impacts without the birds penetrating the nose skin.

The figures (6.34) and (6.35) show the sequences from the same test but from the up view. It can be noted as the dynamic of impact is similar for both the approaches. It is evident that the results of the simulations demonstrate that the SPH and Lagrangian model are particularly reliable to reproduce in details the dynamic of the event during the normal evolution of the impact, figures (6.36) and (6.37). Those different views allows to follow the deformation of the structure and the behaviour of the bird when impacts the structure, the failure mechanism of the structure is close to the one observed in the experimental test. In general, the simulation results for the Lagrangian and SPH techniques are shown to be in close agreement with one other, and the bird's behaviour produced a different way to deform and to flow on the structure, which allows to understand the differences between two approaches.

The computer simulations have produced a large amount of information whose main features. Figure (6.38) shows the shape deformation of the

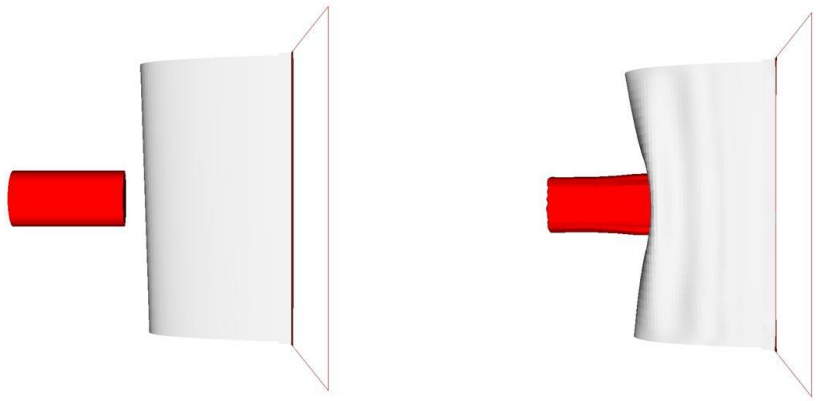

Figure 6.34: Up view of the Lagrangian modelling at 0 and 2 ms

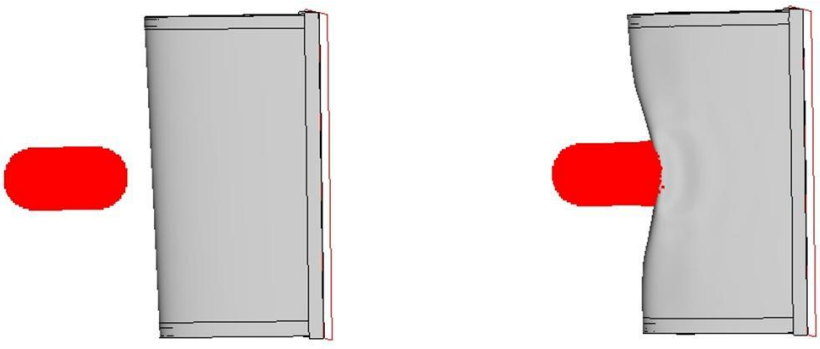

Figure 6.35: Up view of the SPH modelling at 0 and 2 ms

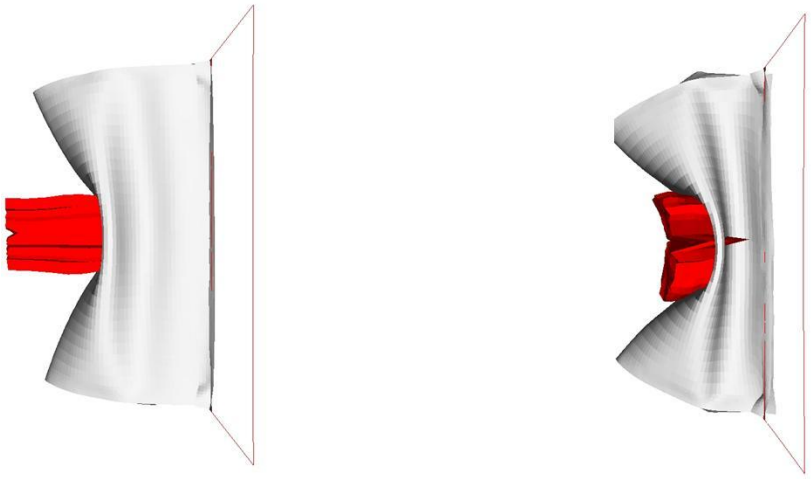

Figure 6.36: Up view of the Lagrangian modelling at 2 and 3.6 ms

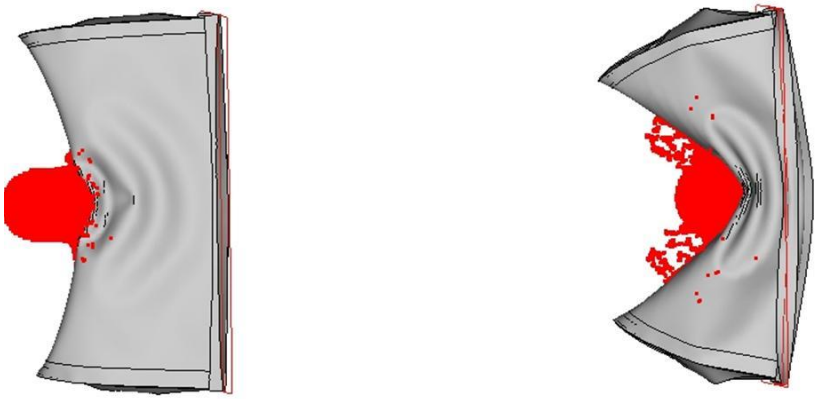

Figure 6.37: Up view of the SPH modelling at 2 and 3.6 ms

configuration in one of the scenarios analysed for the leading edge. Similar to the lagrangian approach, the first thing that should be said is that the damage produced to the skin call to collaborate the whole bay due to the reduced dimensions of the test article, but any perforation is present and the configuration is plastically deformed but the assy maintained the impact evolution absorbing the energy.

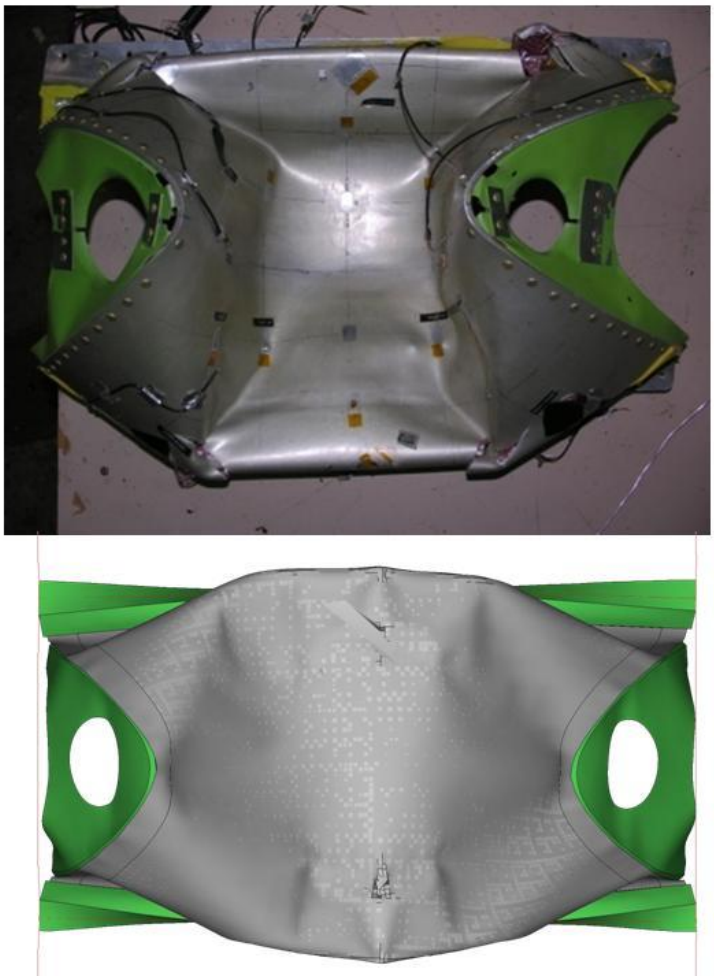

Figure 6.38: Numerical and Experiemental Shape after the impact

As shown in figure (6.39), the shape of the deformation in the skin is characterized by the stiffening role played by ribs, which prevents the overall downward movement from causing more severe damage and reducing the possibility to impact on the spar.

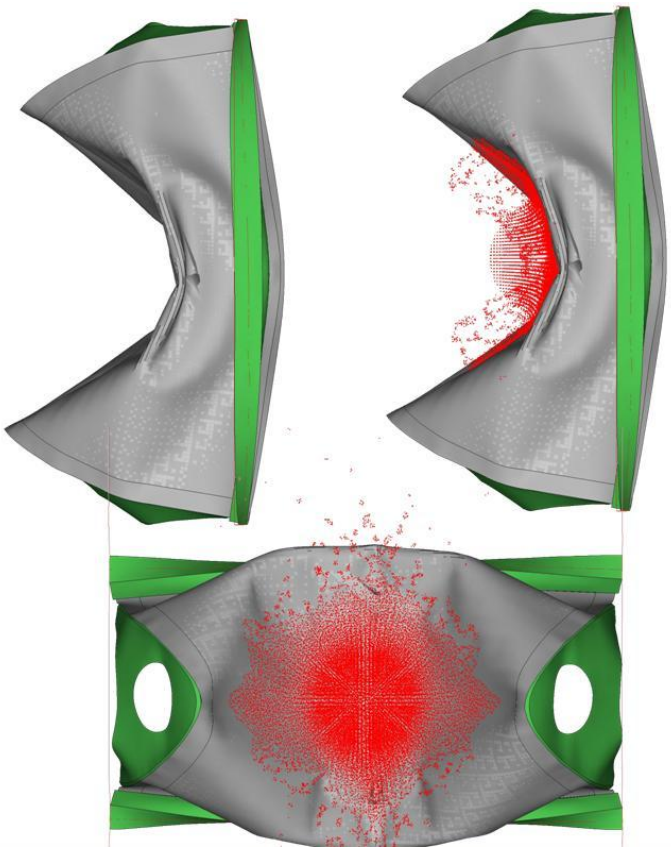

Figure 6.39: Views of the SPH modelling to estimate the damage

Figure (6.40) shows the maximum deformation on the leading edge analysed by SPH approach. From a numerical's point of view the value reported in the plot is 297 mm, which is lower than the real value recorded during the experiemntal test (350mm), while the lagrangian approach in the last section reported 340 mm. This difference about the deformation is a convincing

argument to insist on the lagrangian approach even if the SPH approach has remarked a more realistic level of damage and more realistic behaviour to simulate the bird-strike scenario.

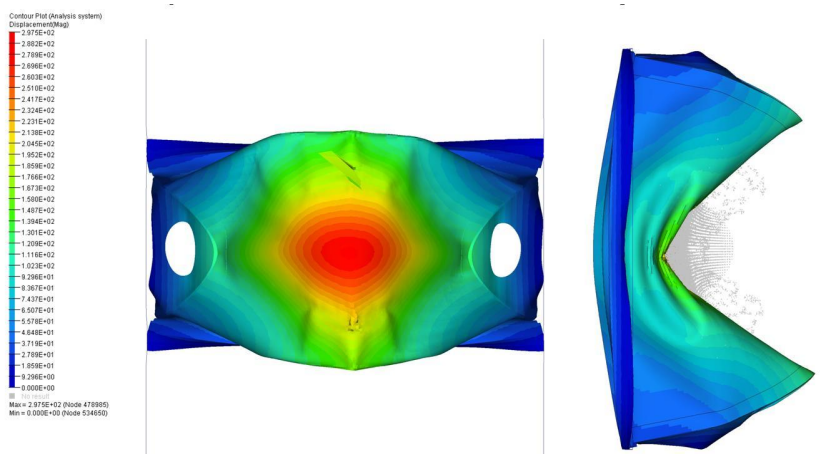

Figure 6.40: Maximum deformation of the SPH modelling at 3.6 ms

Chapter 7

Design of Tailcone

7.1 Impact on the Tailplane

This project took aim to describe how the simulation can be carried out in an industrial environment to obtain the certification of a leading edge of a cargo airplanes, C27J, to a bird-strike requirements. The leading edge of the vertical empennage has a total length of 2970 meters (117 in), with a chord that varies between 450 mm and 750 mm (18 in and 30 in), see figure (7.1).

The objective of this study was to verify the basic assumption of the analysis and to monitor the bird impact on fin structure in composite adopting the Lagrangian, Arbitrary Lagrange Euler (ALE) and Smooth Particle Hydrodynamics (SPH) approaches to investigate the validity of impact resistance models for analysis of a bird-strike. The numerical finite element simulations were performed using the commercial explicit integration code MSc/Dytran for Lagrangian and ALE approach, and LS/Dyna for the SPH approach. The experimental results are correlated for each method, considering advantages and disadvantages of the different techniques of modelling.

The projectile must be impacted onto leading edge at mid height, the position of the fin related to the water line of the airplane is shown in the

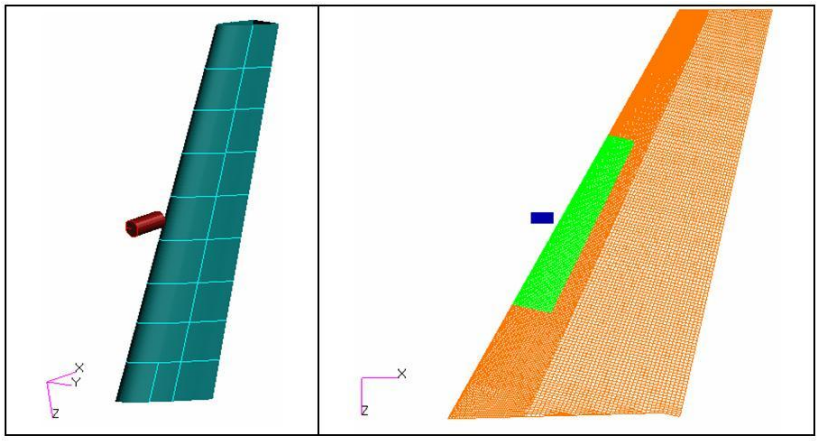

Figure 7.1: General view of the LE and its assembly on the fin of C27J

figure (7.2), the sweepback angle of 63 ° reduces the load peak on the surface during the strike because the bird tends to slide on the leading edge.

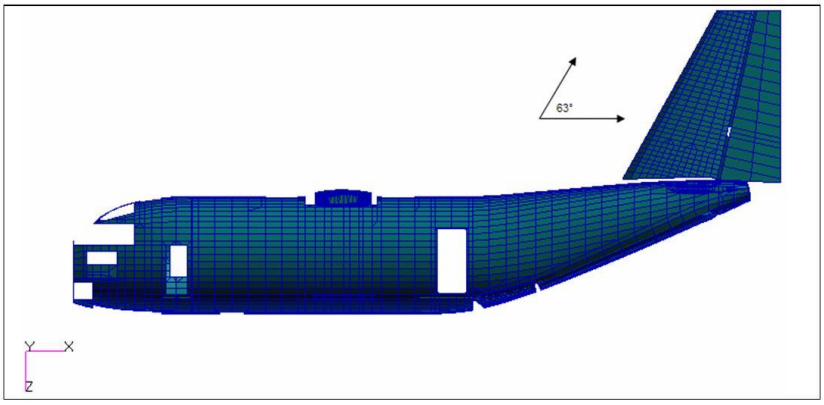

Figure 7.2: Fin position related to water line of the C27J aircraft

The point of impact is chosen on basis of structural requirements. The actual leading edge's configuration of the aircraft presents ten ribs distibuted on the leading edge, figure (7.3), the critical point about impacting is in correspondence of the minimum distance between the leading edge skin and

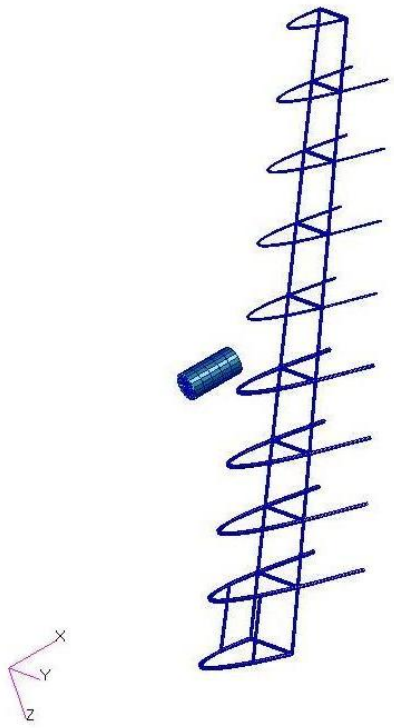

Figure 7.3: Rib Assembly along the tailcone

spar, and for this reason the target results the space between the fifth and sixth rib.

The finite element analysis is performed on the fin, the figure (7.4) shows the stress distribution on the structure adopting the Lagrangian approach, this figure shows the impact sequence in one of the scenarios analysed for the leading edge and shows that the damage produced to the structure is local, only small portion of the leading edge is damaged by the strike, whereas the rest of structure remains in the elastic range. The fringe plot shows the stress distribution in the KPa, that values underline the peak stress of 400MPa is located in the contact zone. The simulations show that the leading edge is

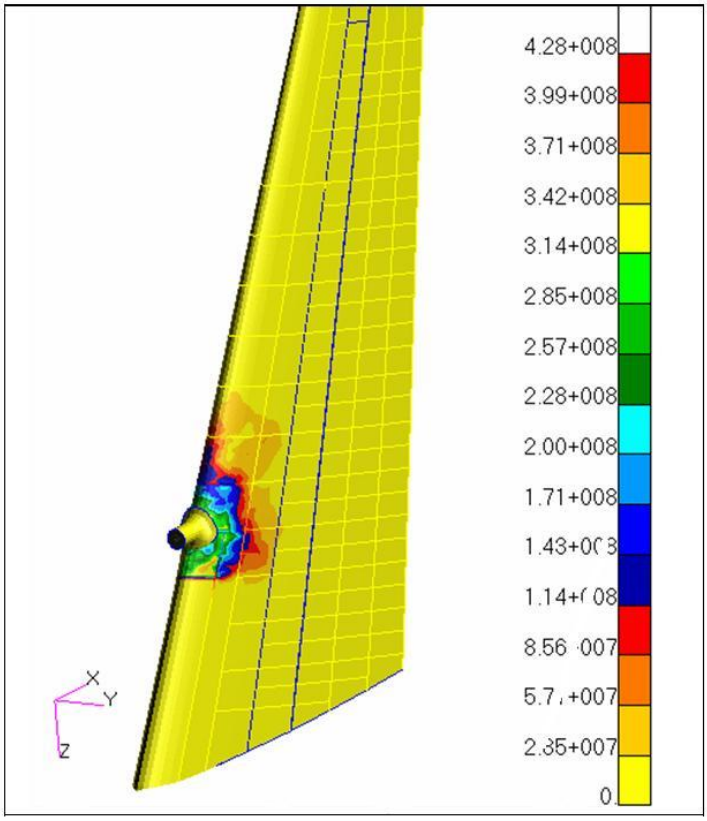

Figure 7.4: Max stress on the C27J fin finite model - Lagrangian Approach

able to withstand the specified impact without the bird penetrating in the structure.

Whereas the ALE approach underlines the fluid behaviour of the bird, as shown in figure (7.5) From images it is possible see the cylinder movement that were lapping on the structure deforming the fin during the transfer of the kinetic energy. This damage is far less severe than the damage caused adopting a Lagrangian approach. The possibility to consider the bird like a hydrodynamic phenomenon, ALE approach, costs disadvantages about the computational runtime related to Lagrangian approach, as it is shown

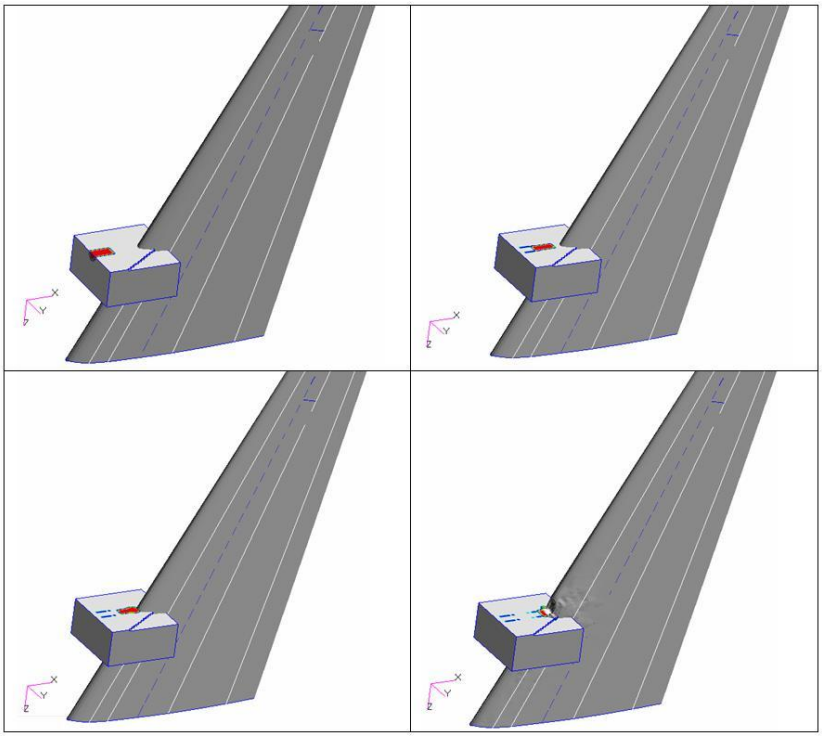

Figure 7.5: C27J fin finite model - ALE Approach

in table (7.1) The other disadvantage it is the peak of contact force, in the figure (7.6), ALE approach undervalues the real contact. The typical response of a composite leading edge is plotted in figure (7.7) The out of plane displacement is measured in the centre of the plate. In general the ALE approach defined a difficulty in the model and in the post processing phase, then this approach has been defined with a heavy runtime, moreover the peak of the impact force and the maximum deformation has been underestimate by the ALE approach, whereas the using the Lagrangian approach the model was accurate to predict the final deformed shape of the leading edge and the absence of foreign object penetration, showing that the designed leading edge made with honeycomb and aluminum material was able to protect

	Lagrangian Approach	**ALE) Approach**
elements	133,163	133,163
runtime	2h and 40m	22hours

Table 7.1: Comparison between runtime for Lagrangian and ALE Approach

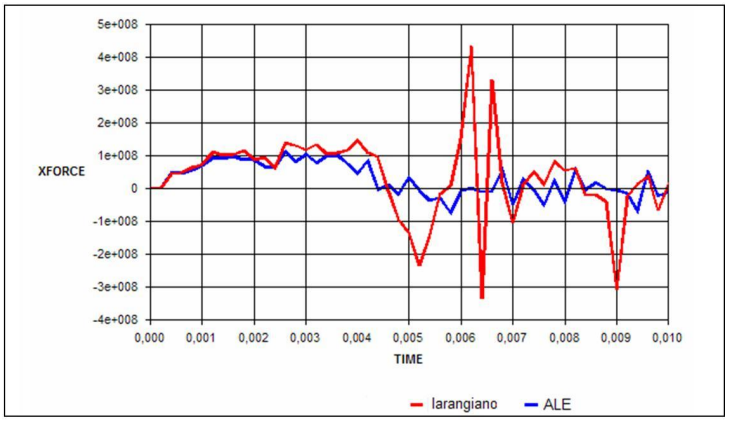

Figure 7.6: Contact force time history by Lagrangian and ALE approach

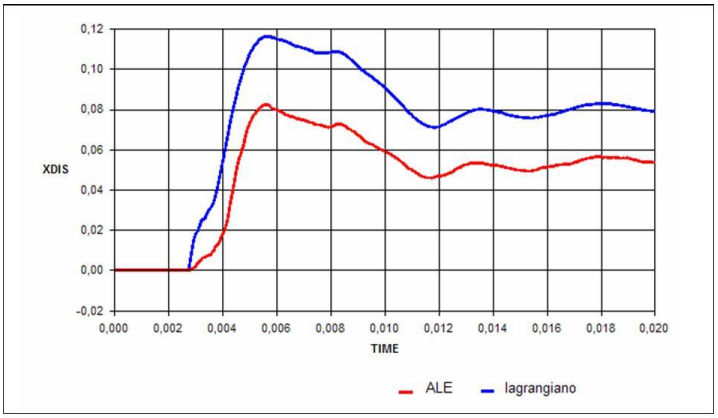

Figure 7.7: THS of the deformation with Lagrangian and Ale approach

the inner Leading edge structure from damaging and to satisfy certification requirements.

This analysis have obtained good results and for this reason a new concept of the leading edge was introduced, considering a ribless configuration, (7.8), infact according to numerical results the stress is concentrated in cor-

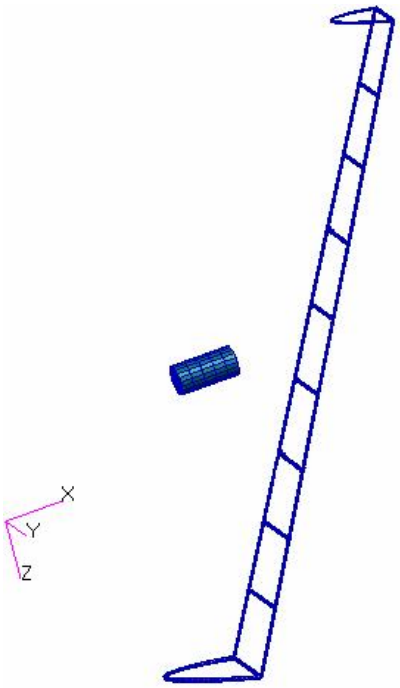

Figure 7.8: Ribless Configuration

respondence of ribs attachement, and this produced a failure of the leading edge in interface area between the ribs and the inner ply of the leading edge, (7.9). This consideration collects even more votes if you think to manufacturing process, because the installation of the ribs on the composite leading edge could produce a difficulty assembly because of the honeycomb presence. The rib must be installed on the outer ply and for this reason is necessary

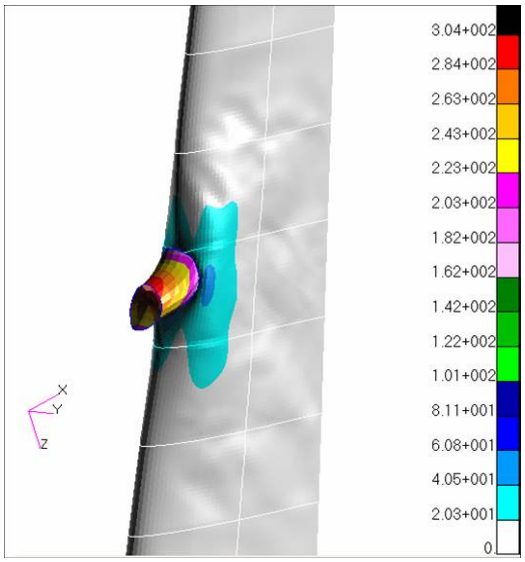

Figure 7.9: Stress is concentrated in interface

create a hole for each honeycomb panes to create the slot of the rib. Without the ribs the manufacturing would have its advantages.

7.2 Design of a Novel LE Structure

Having successfully developed and validated the material damage and delamination models for the skins, (49) and (50), which are the most crucial parts of a reliable numerical bird-strike simulation methodology, the FE models of the complex LE structure and the substitute bird are developed. Verification of the bird-strike test methodology was achieved through several simulations performed on the leading edge structure, which was ribless and in the FML material. This structure closely represents the geometry, material and manufacturing process that was employed on the C27J aircraft.

The numerical tests anticipated the experimental test. The configuration and the design of the leading edge structure was chosen on basis of the

experimental tests conducted on the bay of leading edge, and on basis of the numerical analysis conducted after having modelled the materials with the appropriate failure criteria obtained with the massive campaign of tests. This test article was connected to a test rig attachment, figure (7.10), and only two high-speed camera acquisition system was considered to erecord the phenomenon evolution, the reason is due to the possibility to check only if the bird perforated the LE and if the LE doformation compromises the integrity of the spar.

Figure 7.10: Test Rig attachment

7.2.1 Lagrangian Modelling

The resulting FE model consists of different components, the bird is modeled using Lagrangian brick finite elements with the properties of a fluid, giving an initial velocity and defining a master-slave contact interfaces so to apply the bird element loads to the structure. A lagrangian contact algorithm was

used between the bird and the leading edge. The bird model consists of 1440 brick elements.

The honeycomb core was considered like "Orthotropic Crushable Material Model", and it consist of 22.240 brick elements. About the fiber metal laminate, the "Orthotropic failure material model" was used, which defines the failure properties for an orthotropic material about shell elements. The experimental results, (50), showed that laminates exhibit an improvement in tensile strength over their monolithic aluminum alloys, and stress-strain behaviour is typically bilinear with a transition region associated with the yielding of aluminum layers. Glass fiber/epoxy composite layer of laminates is assumed to be linear elastic up to fracture, and the elasto-plastic behaviour of aluminum layers laminates was taken into account by introducing a plastic potential function. The laminate model consist of 11.120 shell elements.

Before the official test the configuration was studied with a FE analysis to estimate the damages and the numerical results showed a good behaviour at strike. Figure (7.11) shows the time history of the maximum deflection of the LE skin, considering that the spar distance from LE skin is 350mm, this results sounds good.

Besides the spar damage, the numerical model showed good results in the skin damages too, no damage was evident from the impact in either the test article or the model. The skin did not presented perforation and the wing box was able to absorb the total impact energy. Figures (7.12), (7.13) and (7.14) show different views of the the maximum deformation about the FE configuration, since the expected effects of the impacts are essentially of local nature, a finer finite element mesh has been designed to produce a good approximation of the deformation in the impact area, specially in the skin. Therefore, the simulations have been able to capture accurately the very localized deformation, (51).

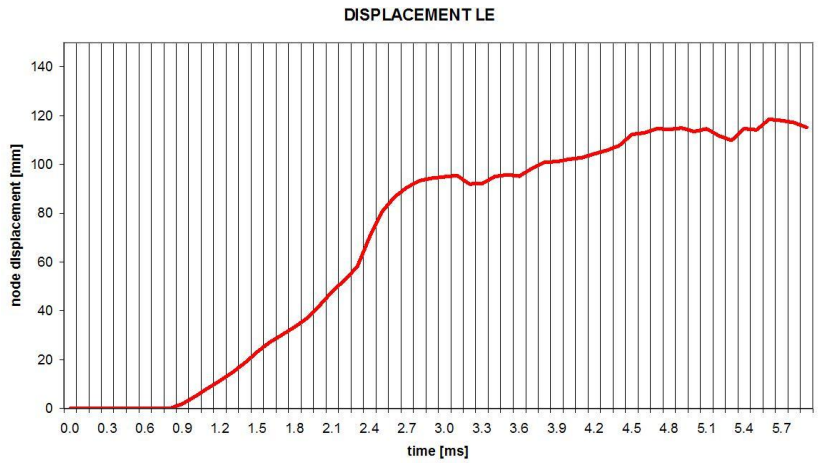

Figure 7.11: Numerical time history of LE skin displacement

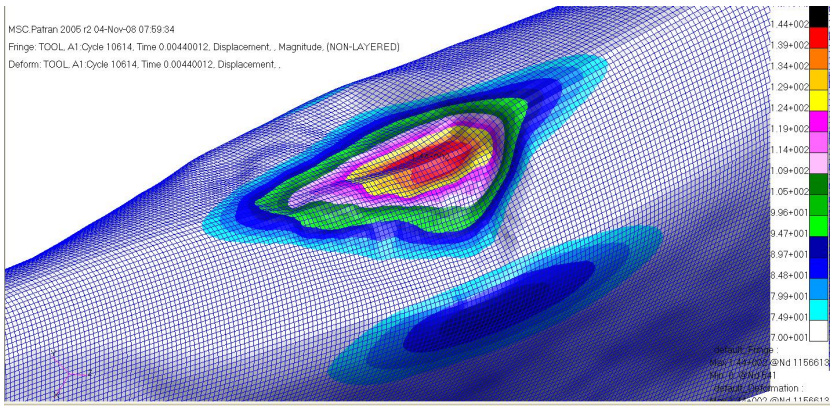

Figure 7.12: Numerical front view of deformation

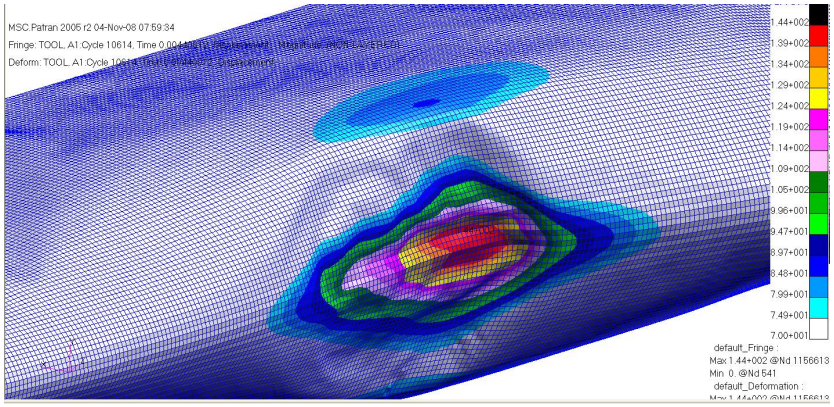

Figure 7.13: Numerical lateral view of deformation

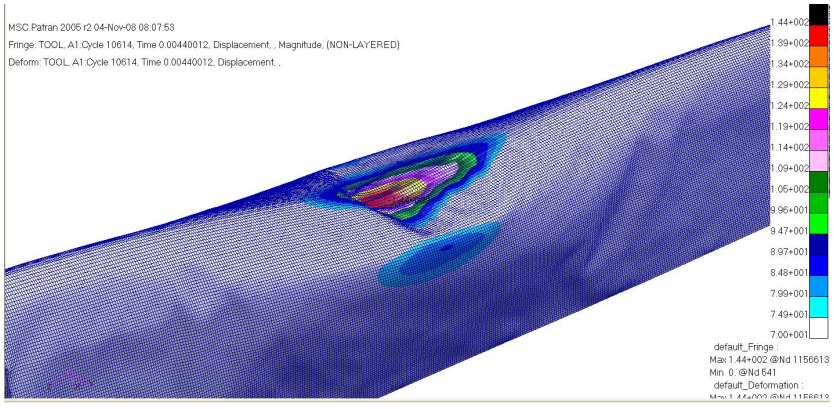

Figure 7.14: Shape wing after the impact

The simulations on LE predicted that the bird-strike at 250kts produced a large deformation but the test is considered passed, because the test article is survivable. A comparison of the bird-strike sequence captured in the test in comparison to the respective simulation is shown in figure (7.15). It may

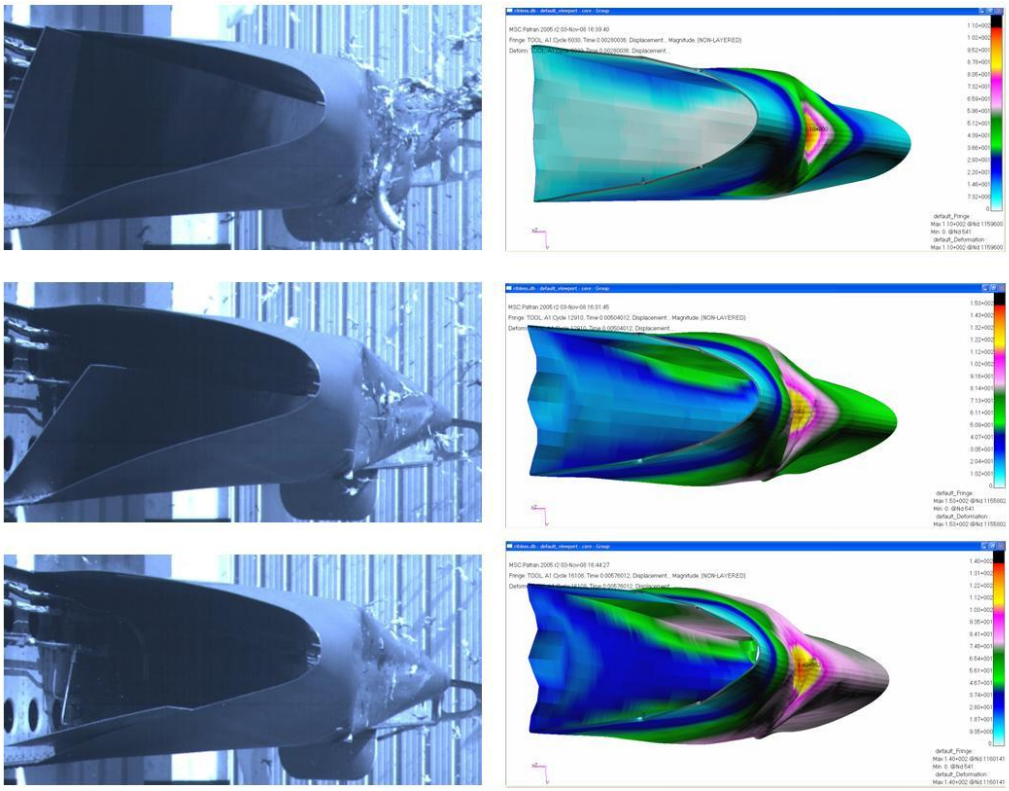

Figure 7.15: Numerical and experimental correlation at different steps

may be observed that in the test the impactor produced a large vibration and deformation but the skin of leading edge presented any perforation and spar is uninjured. The comparison shows a very good agreement between the experimental and the simulated bird-strike evolution. The developed numerical models comprise a useful tool for the analysis of the failure mechanisms and damage propagation of a bird-strike scenario.

Differently to the last numerical results on the leading edge in FML material with the presence of the ribs, the stresses are lower and are only concentrated in the impacted area, which is small related to the whole structure, but the deformations are higher than the same configuration with ribs, probably because there is a higher flexibility and elasticity of the structure and a greater portion of structure is called to collaborate to absorb the impact energy, as shown in the figure (7.16).

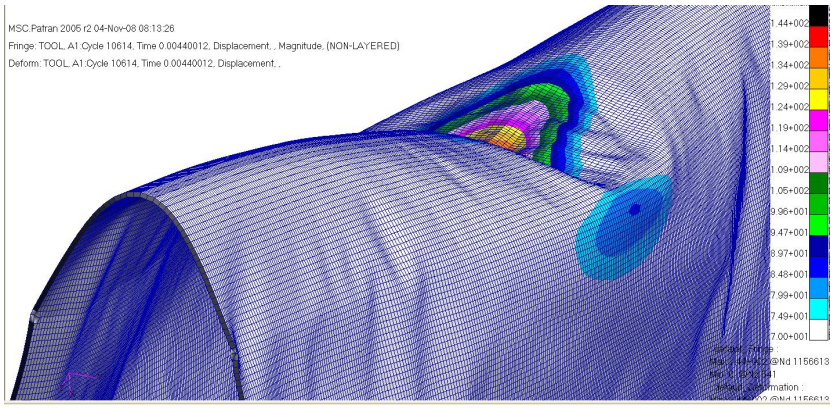

Figure 7.16: A large portion of structure partecipates to absorb the energy

In conclusion, the innovative composite configuration is the best solution capable to satisfy the performance and weight of the leading edge of a tailcone, the absence of ribs produced a lower peak of stress because of there are not interface zones between the skin and ribs but above all, the absence of ribs solved the manufacturing process because is not necessary that the honeycomb was emptied to fix the ribs to outboard skin of the leading edge. Excellent agreement was achieved between the simulation and test in terms of global structural behaviour of the test article, confirming the validity of the approach. In particular, the model was accurate to predict the final deformed shape of the leading edge and the absence of foreign object penetration, showing that the adopted FML material was able to protect the

inner LE structure from damaging. The designed wing leading edge made with FML material was able to protect the inner LE structure from damaging and to satisfy certification requirements. The fiber metal laminate presented a higher resistance to the impact. The model allowed to evaluate the damage on the LE in advance of the experimental test.

Chapter 8

Concluding Remarks

During the various phases of this project research experiences have accumulated on the study of the problem of bird impact both on finite element models and on the experimental phase and materials' characterization. The goal of the research was to develop new products or new processes in the field of industrial research, optimizing the structure of leading edge. Parallely the research has addressed the possibility to identify innovative materials and/or technologies potentially applicable to a classical leading edge configuration of a leading edge. All these topics devoted to the optimization of the structural efficiency and weight savings with regard to the bird-strike requirements.

This work paves the way for highlighting guidelines for modelling of leading edge. It was therefore necessary to perform an optimization process based on the parameters of geometric panel as the warp, the lay-up and thickness. The correct combination of such geometric characteristics may result in a configuration which is able to preserve from the catastrophic phenomenon as the requirement imposed by bird-strike on the leading edge.

The numerical models have allowed the knowledge of the correct trend of the parameters selected for the optimization process. They have been important for the reduction of the number of the experimental tests required for the assessment of the selected structural configuration. Obviously, the

need for at least one experimental test cannot be eliminated, considering also the number of parameters and variables driving such complex dynamic behaviors.

As result of the classical design procedure for a bird-strike resistant leading edge, the fin of the C27J aircraft shows a minimum thickness of the aluminum panel equal to 3.1 mm. The study of advanced optimization on different configurations of leading edge has highlighted, on the contrary, the possibility of considering different materials and of implementing a ribless configuration of the leading edge, thus guaranteeing the shape of the profile with the aluminum flexcore. The resulting structure is characterized by an higher global stiffness, and therefore it performs very well in absorbing impacts and resisting to the compression loads despite a lower density and weight compared to the classical design.

Another important aspect to highlight is that this configuration provides the ability to solve the problem related to the complexity of manufacturing. The presence of the ribs, indeed, requires that the flexcore vanishes to allow the application of the ribs on the outer skin edge, or alternatively to create a single component of honeycomb that covers the areas between two ribs. The numerical analysis, based on the finite element model, showed that the behaviour of the ribless configuration, impacted by an 8 pound simulated bird at a speed of 129 m/s. The result of such calculation indicates a deformation involving the entire surface of the leading edge so that the kinetic energy is distributed over a very large area of the panel.

Initially the experimental results were obtained on the simple component of the leading edge, and parallely the numerical models were referred to a single bay only. These studies have allowed the correlation between the numerical and the experimental results and the identification of the necessary parameters for the comparison and the failure criteria of the materials used during the tests.

Then, the results were extended on the full scale leading edge. Several numerical models have been implemented for the analysis of the potential leading edge different configuration. The selected structural arrangement has been finally tested in the real full scale configuration. The experimental results, confirming those obtained numerically, has validated the approach and it may be regarded as one successful case of a complex design supported by the numerical optimization.

During the entire research project, the FE analysis have been performed using different approaches: Lagrangian, ALE and SPH. Our latest conclusion is that, for the specific analyzed cases, the lagrangian approach may be preferred for its better approximation to the experimental results, even if the possibility of a numerical instability error, due to the large distortions of the mesh, is higher compared to the other approaches.

On the other hand the SPH approach needs to be more investigated, especially in a bird-strike scenario, since the behavior of the bird deformation impacting the structure appears to be more realistically modeled than the previous approaches.

References

[1] E.F.Lebow. *Cal Rodgers and the Vin Fiz: the First Transcontinental Flight*. Washinghton D.C.: Smithsonian Institution Press, 1989. 1

[2] E.C.Cleary, R.A.Dolbeer, and S.E.Wright. *Wildlife strike to civil aircraft in the united states 1990 - 2003*. Federal Aviation Administration National WildLife Strike Database Serial Report Number 10, 2004. 2

[3] W.Servoss, R.M.Engeman, S.Fairaizl, J.L.Cummings, and N.P.Groninger. *Wildlife hazard assessment for phoenix sky harbour international airport*. International Biodeterioration and Biodegradation, volume 45 pages 111-127, 2000. 3

[4] Certification Specifications CS 25.631. *Bird strike damage*. EASA Certification Specifications for Large Aeroplane, 2003. 3, 9, 33

[5] Certification Specifications CS 25.335. *Design Airspeede*. EASA Certification Specifications for Large Aeroplane, 2003. 4

[6] I.I.McNaughton. *The design of Leading Edge and Intake Wall Structures to resist Bird Impact*. RAE TR72056, 1972. 6

[7] E.Parkes. *The permanent deformation of a cantilever strucks transversely at its tip*. Proc. Roy. Soc. Lond., England, 1955. 6

[8] J.P.Barbers, H.R.Taylor, and J.S.Wilbeck. *Characterization of Bird Impacts on a Rigid Plate*. Technical Report AFFDL-TR-75-5, 1975. 6, 117

[9] B.N.Cassenti. *Hugoniot Pressure Loading in Soft Body Impacts*. United Technologies Research Center, Connecticut, 1979. 7

[10] W. Goldsmith. *Impact: The Theory and Physical Behaviour of Colliding Solids*. Dover Publications, Mineola, New York, 2001. 7

[11] C.Stoker. *Development of the Arbitrary Lagrangian-Eulerian method in nonlinear solid mechanics*. HC Stoker Enschedel, the Netherlands, 1999. 7

[12] N. Birnbaum, N. Francis, and B. Gerber. *Coupled Techniques for the Simulation of Fluid-Structure and Impact Problems*. Century Dynamics Inc, 1997. 7

[13] C.J.Read. Standard test method for bird impact testing of aerospace transparent enclosures. *ASTM F330-89*, 2004. 8

[14] Certification Specifications CS 25.775. *Windshield and windows*. EASA Certification Specifications for Large Aeroplane, 2003. 9

[15] Certification Specifications CS 25.571. *Damage tolerance and fatigue evaluatuion of structure*. EASA Certification Specifications for Large Aeroplane, 2003. 9

[16] Federal Aviation Regulation FAR 33.76. *Bird ingestion*. FAA, 2007. 9

[17] Wilbeck J.S. *Impact behaviour of low strength projectiles*. PhD dissertation, Texas AM University, 1997. 18, 21

[18] Wilbeck J.S. and Rand J.L. *The development of a substitute bird model.* ASME 81-GT-23 Gas turbibne conference and products show. Houston, TX, USA. American Society of Mechanical Engineers, 1981. 19

[19] *MSC Dytran theory manual.* MSC/Software, 2005. 26, 94, 115

[20] Carlo Alberto Huertas-Ortecho. *Robust Bird-strike Modeling Using Ls-Dyna.* PhD thesis, University of Puerto Rico, Department of Mechanical Engineering, 2006. 26

[21] Monaghan J.J. Smoothed particle hydrodynamics. *Annual Review of Astronomy and Astrophysics*, 30:543–574, 1992. 28

[22] Lakshmi S. Nizampatnam. *Models and Methods for Bird strike load predictions.* PhD thesis, Wichita State University, Department of Aerospace Engineering, 1999. 30

[23] A.Airoldi and Cacchione. Modelling of impact forces and pressures in lagrangian bird strike analyses. *International Journal Of Impact*, 32:1651–1677, 2006. 31

[24] L.B.Vogelesang and A. Vlot. Development of fiber metal laminates for advanced aerospace structures. *Journal of Materials Processing Technology*, 103:1–5, 2000. 36, 37, 38, 39, 66

[25] A.Vlot and J.W.Gunnink. *Fibre Metal Laminates an introduction.* 36

[26] M.O.W.Richardson and M.J.Wisheart. Review of low velocity impact properties of composite materials. *Composites Part A: Applied Sceince and Manufacturing*, 27:1123–1131, 1996. 37, 54

[27] A.Asundi and A.Y.N. Choi. Fiber metal laminates: An advanced material for future aircraft. *Jorunal of Materials Processing Technology*, 63:384–394, 1997. 37

[28] J. Sinke. Development of fiber metal laminates: concurrent multi-scale modeling and testing. *Journal of Materials Processing Technology*, 103:1–5, 2000. 37, 38, 39

[29] L.B. Vogelesang, J. Schijve, and R. Fredell. Fiber metal laminates: damage tolerant aerospace materials. *Case Studied in Manufacturing with Advanced Materials*, 2:250–260, 1995. 38

[30] H. Zhao and G.Gary. Crushing behaviour of aluminium honeycomb under impact loading. *Journal Impact Engineering*, pages 827–836. 41

[31] *Standard Test Method for Testing of Metallic Materials.* Philadelphia: Americam Society for Testing and Materials, 2005. 50

[32] A.Vlot. *High Starin Rate Tests on Fibre Metal Laminates.* 52

[33] M.A.McCarthy, J.R.Xiao, N.Petrinic, A.Kamoulakos, and V.Melito. Modelling of bird strike on an aircraft wing leading edge made from fiber metal laminates - part 1: Material modelling. *Applied Composite Materials*, pages 295–315. 52

[34] *Standard Test Method for Impact resistance of rigid plastic sheeting or parts by means of a tup (Falling Weight).* Philadelphia: Americam Society for Testing and Materials, 1982. 52

[35] T.Mitrevski, I.H.Marshall, and R.Thomson. The influence of impactor shape on the damage to composite laminates. *Journal of Composite Structures*, pages 116–122. 52

[36] M.T.Kortschot and C.J.Zhang. Characterization of composite mesostructures and damage by de-ply radiography. *Composite Science and Technology*, 53:175–181, 1995. 53

[37] D.J.Elder, R.S.Thompson, M.Q.Nguyen, and M.L.Scott. Review of delamination predictive methods for low speed impacts of composite laminates. *Composite Structures*, 66:677–683, 2004. 54

[38] Y.Aoura, D. Ollivier, A.Ambari, and P.Dal Santo. Determination of material parameters for 7475 al alloy from bulge forming tests at constant stress. *Journal of Materials Processing Technology*, 145:352–359, 2004. 54

[39] N.Tsartaris, F.Dolce, U.Polimeno, M.Meo, M.Guida, F.Marulo, and M.Riccio. Low velocity impact behaviour of fibre metal laminates. *Seventeen International Conference on Composite Science and Technology, (ICCST/7)*, Proceeding, CD-ROM, 2009. 59

[40] A.Rodis, A.Del Grande, M.Murarotto, E.V.Pizzinato, W.Shnabel, and C.Alberini. *Strain rate effects on the Mechanical Properties Thin Sheet Carbon Steels and Glass Fibre Composites*. Centro Ricerche Fiat, 1992. 66

[41] A. AiroldI and B. Cacchione. Numerical analysis of bird impact on aircraft structures undergoing large deformations and localised failure. *WIT Transactions on Engineering Sciences. In, Impact of Lightweight Structures*, 49, 2005. 79

[42] G.H.Shaue H.Lee. The thermomechanical behaviour for aluminium alloy under uniaxial tensile. *Materials Science and Engineering*, pages 154–164. 79

[43] A.Matzenmiller. On damage induced anisotropy for fiber composites. *International Journal of Damage Mechanics*, pages 71–86. 82

[44] Scott D.Papka and S.Kyriakidie. In-plane compressive response and crushing of honeycomb. *Journal of Mechanical Phys. Solids*, 42:1499–1532, 1994. 85

[45] R.S.Birch and M.Alves. Dynamic failure of structural joint systems. *Thin-Walled Structures*, pages 136–154. 86

[46] M.Guida, F.Marulo, M.Meo, and M.Riccio. Evaluation and validation of multi-physics fe methods to simulate bird strike on a wing leading edge. *13th European Conference On Composite Materials, (ECCM/13)*, Proceeding, CD-ROM, 2008. 117

[47] B.Langrand, A.S.Bayart, Y.Chauveau, and E.Deletombe. Assessment of multi-physics fe methods for bird strike modelling application to a metallic riveted airframe. *International Journal of Crashworthiness*, pages 415–428. 117

[48] M.A.McCarthy, J.R.Xiao, A.Kamoulakos C.T.McCarthy, J.Ramos, J.P.Gallard, and V.Melito. Modelling of bird strike on an aircraft wing leading edge made from fiber metal laminates - part 2: Modelling of impact with sph bird model. *Applied Composite Materials*, pages 317–340. 117

[49] M.Guida, F.Marulo, M.Meo, and M.Riccio. Analysis of bird impact on a composite tailplane leading edge. *Applied Composite Materials*, pages 241–257. 134

[50] M.Guida, F.Marulo, M.Meo, and M.Riccio. Analysis of bird strike on a wing leading edge made of fibre metal laminates. *Sixteen International Conference on Composite Science and Technology (ICCST/6)*, Proceeding, CD-ROM, 2006. 134, 136

[51] M.Guida, F.Marulo, M.Meo, and M.Riccio. Transient three dimensional finite element analysis of a bird striking a sandwich tailplane leading edge. *Seventeen International Conference on Composite Science and Technology, (ICCST/7)*, Proceeding, CD-ROM, 2009. 136